FABRICATION AND CHARACTERIZTION OF ALN THIN FILM BULK ACOUSTIC WAVE RESONATOR

by

Qingming Chen

BS, Tsinghua University, P. R. China, 1999

MS, Tsinghua University, P. R. China, 2001

Submitted to the Graduate Faculty of

the School of Engineering in partial fulfillment

of the requirements for the degree of

Doctor of Philosophy

University of Pittsburgh

2006

UNIVERSITY OF PITTSBURGH

SCHOOL OF ENGINEERING

This dissertation was presented

by

Qingming Chen

It was defended on

July 24, 2005

and approved by

Dr. John A. Barnard, Professor, Department of Materials Science and Engineering,

Dr. Scott X. Mao, Professor, Department of Mechanical Engineering

Dr. William S. Slaughter, Associate Professor, Department of Mechanical Engineering

Dr. Patrick Smolinski, Associate Professor, Department of Mechanical Engineering

Dissertation Director: Dr. Qing-Ming Wang, Associate Professor,
Department of Mechanical Engineering

FABRICATION AND CHARACTERIZTION OF ALN THIN FILM BULK ACOUSTIC WAVE RESONATOR

Qingming Chen, PhD

University of Pittsburgh, 2006

This dissertation presents the fabrication and characterization of the AlN thin film bulk acoustic wave resonator (FBAR). The bulk acoustic wave (BAW) resonators and filters have been considered the most promising devices used in the frequency control and wireless communication field when the performance frequency is up to GHz range. AlN is a piezoelectric material with hexagonal crystal structure. Some of its properties such as high longitudinal acoustic wave velocity (~11000m/s), high thermal conductivity, and high thermal and chemical stability make it a suitable material to fabricate the thin film bulk acoustic wave resonator.

In this study, first, the background that includes the concepts of the FBAR resonators and filters, the piezoelectricity, the material properties of some of the piezoelectric materials and the MEMS techniques is introduced. Following the introduction, the fabrication and characterization of the AlN thin film, the composite BAW resonator and membrane type FBAR are presented. AlN thin films deposited under various sputtering deposition conditions have been investigated and characterized. X-ray diffraction (XRD) and scanning electron microscopy (SEM) characterization results show that the highly c-axis oriented AlN thin films have been deposited on the Si and sapphire substrate at the appropriate conditions. The effective piezoelectric coefficient d_{33eff} and the mechanical properties such as the hardness and the reduced elastic constant of the AlN thin film in the four-layer composite resonator have been measured

by the single beam laser interferometer and nano-indentation methods, respectively. Then, the transfer matrix method is developed to characterize the impedances and electromechanical properties of the multilayer FBAR and composite BAW resonator. The effects of the type and thickness of the electrodes and support layers on the resonance frequency and effective electromechanical coupling coefficient k_{eff}^2 are discussed. The resonance frequency control and tuning methods including the connection to the external circuits and the incorporation of the support SiO_2 layer are also discussed. In addition, the vector network analyzer has been utilized to measure the resonance frequency response of the four-layer composite BAW resonator and the material properties have been characterized from the experimental data. Lastly, the accomplishments of this study are summarized and future perspectives are provided.

TABLE OF CONTENTS

LIST OF TABLES

LIST OF FIGURES

ACKNOWLEDGMENTS

First and foremost, I would like to thank my advisor, Dr. Qing-Ming Wang, for supporting me, encouraging me, for providing continuous motivation throughout my dissertation work and for all his optimism, patience and words of kindness. The guidance and support given by Dr. Wang has been of tremendous professional and personal benefit.

I am very thankful to the members of my thesis committee, Drs. John A. Barnard, Scott X. Mao, William S. Slaughter, and Patrick Smolinski. Thank you for your time, encouragements and valuable advices. I also want to thank the faculty and staff members in the Department of Mechanical Engineering, who have made my studies here valuable and enjoyable.

I also would like to thank Dr. Yongping Ding for the interesting discussions and his helpful suggestions.

I would like to thank all the friends I have made in Pittsburgh: Tao Zhang, Fang Li, Yue Ke, Peng Yuan, Chunhua Fu, Yixin Lu, Fei Yan, Lifeng Qin, Zhaochun Yang, Jianjun Yao, and Hongbin Cheng. Special thanks go to my dear friends Miao Jin and Binbin Chen.

Finally, I reserve my sincere thanks for my family members. I am deeply indebted to my father: Jian Chen, my mother Lunqiong Li, and my brother: Hongming Chen for their never ending love, dedication and support through my long journey of study. They have done so much for me in the past, and words cannot express the gratitude I have. I am also thankful for the encouragements provided by my sister-in-law.

1.0 INTRODUCTION

1.1 OVERVIEW

In many technical systems there is a strong trend for miniaturization of the components and systems. On one hand, the small components and systems perform differently so that the small systems can perform actions and functions that the large systems cannot do. In many cases the miniaturization makes the systems more convenient and efficient. On the other hand, technologies derived from IC-fabrication process allow the production of miniature components in large volumes for low prices. Micro Electromechanical Systems (MEMS) is one of the notions used to indicate the science of miniaturized mechanical components and systems. The term MEMS refers to a collection of micro sensors and actuators, which can sense its environment and have the ability to react to changes in that environment with the use of a microcircuit control. During the past decades, several new fabrication techniques have evolved which helped to popularize MEMS, and numerous novel devices have been reported in diverse areas of engineering and science. [1]

The core element in MEMS generally consists of two principal components: a sensing or actuating element and a signal transduction unit [2]. Micro sensors are made to sense the existence and the intensity of certain physical, chemical, or biological quantities, such as temperature, pressure, force, sound and chemical compositions [3-7]. Micro sensors have the advantages of being sensitive and accurate with a relative small amount of required sample substance. MEMS technology has found broad acceptance in the field of automotive sensors and

inkjet print heads in the past 10 years. Many suppliers today offer sensors for pressure, acceleration and mass-flow. However, compared to these relatively mature markets, the applications of MEMS technology in the RF communication and high frequency control and tuning fields are just emerging and developing.

Recently, with the great development in the cellular phone, navigation system, satellite communication and various other forms of wireless data communication, the frequency control becomes a key issue as the operation frequency is up to low or medium GHz range. Also, in order to minimize and improve the capacity of such systems, the development of high performance, miniature, on-chip filters and resonators operating in the low and medium GHz frequency range is needed. For example, there is a growing need for front-end filters that protect receivers from adjacent channel interference and output filters that limit the bandwidth of transmitter noise [8].

Traditionally, the RF filters refer to that work at the frequency range from 100MHz to 10GHz as filters working at higher frequencies are usually called microwave filters instead of RF filters. The frequency range from 100MHz to 6GHz is most suitable for medium and short-range terrestrial radio transmission in typical urban environmental as the damping is still acceptable low, antenna size is reasonable and sufficient bandwidth can be provided. Since all suitable frequency bands have been occupied by TV broadcasting, cellular phone system, cordless phones, Bluetooth, wireless local area networks (WLAN) and many other applications, the high selective RF filters become essential to avoid the interference between such applications.

Nowadays, most of the RF filters are used in the cellular phones. For example, in 2002, the RF filters for cellular phones accounts for 80% of the total market. All cellular phones need RF filters to protect the sensitive receive path from interference by transmit signals from other users

and noise from various RF sources. The minimum receive signal strength at which a phone must still operate can be 120 dB lower (a factor of 10^{12} in power) than the strength of interfering signals. Therefore, highly selective RF filters are needed between antenna and preamplifier to amplify the signals from the correct receive band. Selective RF filters are also needed in the transmit path of cellular phone as regulations forbid the emission of RF power outside the specified transmit band. A further application of RF filters in cellular phone is channel selection using intermediate frequency (IF) filters in the classical heterodyne receiver. RF filters can also be used in Global Position System (GPS) receivers and navigation system, short-range systems such as Bluetooth (2.45GHz) and many data communication systems.

In these wireless applications, power consumption is a critical factor. An absolute minimum current drain is a key design goal because battery weight and size influence consumers. Thus, low loss and high qulity factor (Q) for filter elements are absolute requirements in wireless application design. The insertion loss of the front-end bandpass filter and the noise figure of the low noise amplifier (LNA) dominate the noise figure of a receiver. Therefore, small size, low insertion loss, low power consumption and on-chip RF filters are very desirable.

1.2 TYPES OF RF FILTERS

Practically all the RF filters required for the applications mentioned above are bandpass filters. According to classical filter theory, a bandpass filter can be implemented by electrically or mechanically coupling two or more resonators. Each resonator in the filter structure can be any of different types, including LC resonator, transmission line resonator, ceramic resonator,

surface acoustic wave (SAW) resonator, or bulk acoustic wave (BAW) resonator. The performance of various front-end filter technologies at 1575MHz is shown in Fig. 1.1.

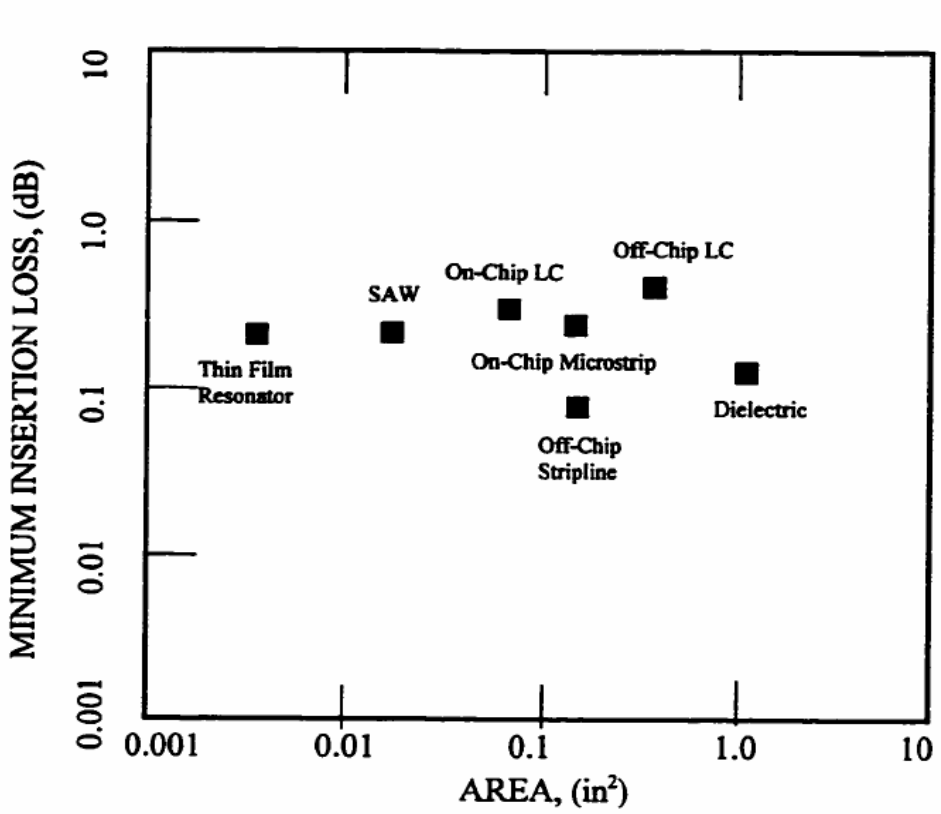

Figure 1.1: Comparison of various front-end filter technologies at 1575 MHz [9].

1.2.1 LC resonators

Inductors (L) and capacitors (C) can be connected in networks with a certain topology to form the filters. Lumped inductors and capacitors are used to design IF filters because at intermediate frequencies, their parasitics are negligible and resonator *Q*s are fairy high. However, at the frequency higher than 0.8 GHz, parasitics are not negligible, making it difficult to realize filter functions. For example, when the physical length of an inductor is not a proper fraction of a wavelength at the operating frequency, transmission line effects appear, with

accompanying frequency dependent parameters [9]. Also, on-chip LC resonator technology is unattractive for realizing a commercially miniature on-chip RF filter due to the excessive volume been taken up by using of on-chip inductors and capacitors. Fig. 1.2 shows the LC resonators fabricated by Reactel, Incorporated (Maryland, USA).

Figure 1.2: LC resonators.

1.2.2 Transmission line resonators

The resonance exhibited by open- and short-circuited lengths of transmission line can be adopted by the filter design. For example, an open-circuited transmission line will exhibit a parallel resonance when its electrical length is a multiple of $\lambda/2$; while a series resonance circuit will result when the electrical length is an odd multiple of $\lambda/4$. At the frequency of interest, microstrips are commonly used in filter design. The resulting device is generally too large and

therefore, unsuitable for use as a front-end bandpass filter for next generation wireless communication applications [9].

1.2.3 Ceramic resonators

The ceramic filters are extensively used for RF filters in cellular phones. The wavelength of an electromagnetic wave at 1GHz in air is 0.3 meters. In the materials with higher dielectric ε_r the wavelength can be reduced by a factor of constant $\sqrt{\varepsilon_r}$. Materials with dielectric constant $10 \leq \varepsilon_r \leq 100$ are suitable for building the filter. Materials with even higher dielectric constant tend to have too high intrinsic losses in the frequency range of interest. Low loss high dielectric materials are often used to significantly reduce filter volume and produce low loss bandpass filters. The high dielectric constant of the resonator ensures that most of the fields are contained within the dielectric. Ceramic bandpass filters are used in many cellular front-end designs because of the filter low loss and relatively low cost characteristics. The domain of ceramic filters is the antenna-duplexer application in CDMA phones at 1900 MHz because of their abilities to handle the power capabilities and selectivity in the frequency range. Ceramic filters can also be used in Bluetooth systems and other short range applications at higher frequencies. However, ceramic filters cannot be integrated on silicon because of the dimensional nature. Ceramic filters with high selectivity occupy a quite large board space and they are usually the components with the largest height on the printed circuit board of a cellular phone. Thus, they are unsuitable for the application in designing miniature on-chip RF filters.

Fig. 1.3 shows the ceramic filters fabricated by Argo Technology Co. Ltd. (Taiwan, China).

Figure 1.3: Ceramic filters.

1.2.4 Surface acoustic wave resonators

The electronics industry first used acoustic wave devices in 1965 when it was discovered that surface acoustic wave (SAW) transducers could be useful in the design of analog filters with selected frequencies in the range of 10MHz to 1GHz and above. Afterwards SAW devices have been developed for consumer, commercial, and military applications such as oscillators, resonators, sensors, actuators, accelerometers, and microscopes [10]. SAW filters dominate the RF filter market today since SAW resonators are much smaller than transmission line and ceramic resonators due to the fact that the velocity of acoustic wave is about 10000 lower than the velocity of an electromagnetic wave. Accordingly the acoustic wavelength is only a few microns at 1 GHz. Therefore the resonator based on acoustic standing wave can have much smaller size. Piezoelectric materials are widely used in the acoustic wave resonators to couple energy between electrical and mechanical domain. The mostly used piezoelectric substrates for SAW filters are quartz, lithium niobate and lithium tantalite.

In SAW filters, the acoustic waves travel along the surface of the piezoelectric layer in one lateral direction. Such acoustic waves are generated and picked up by interdigital combfinger transducers, which are made of metal lines. In the vertical direction the acoustic wave energy will not dissipate because of the quickly decays of the acoustic wave. The filter function is defined by the structure of the metal lines and the gratings structures between the interdigital transducers.

For the application of the SAW filters, we have to consider several problems. The periods of combfingers of the SAW filters have to be very small for the application at frequency above 2 GHz. Actually, SAW filters for frequencies above 2.5 are not available now. The second issue we should consider is the power handling capabilities of the SAW filters at high performance frequency. In some cases, the narrow combfingers have to carry very large current density that causes problems such as electromigration and overheating. SAW filters also have the disadvantage of being temperature dependent. The temperature dependence requires the choice of a specific material that may not yield a device with the lowest loss. The combfingers cannot be passivated and are therefore sensitive to corrosion. Thus, the high-performance filters have to be mounted in hermetically sealed packages. Several techniques employed to overcome these disadvantages usually add to the overall cost of productions and make it difficult to integrate SAW filters with silicon IC. Fig. 1.4 shows the SAW filters fabricated by RF Monolithics, Inc. (Texas, USA).

The main reason RF filter integration remains a challenge is the difficulty of realization a high Q inductor on chip. The typical inductor Q in the conventional CMOS process is less than 10. With copper metallization and a thick top metal layer far above the silicon substrate, an inductor Q of 20 has been demonstrated. However, the insertion loss of a filter implemented with

an inductor Q of 20 still remains quite large. To achieve insertion loss of only a few dBs requires a Q in the hundreds. Presently, only discrete filters can achieve such a high Q.

Thin film BAW filters, like SAW filters, are composed of resonators whose dimensions are much smaller than transmission line and dielectric filters. Acoustic waves are confined to the thin film piezoelectric material layer, resulting in a low loss device. BAW filter fabrication processes are highly compatible with existing silicon IC processing. Hence, they are suitable for direct integration with other active circuits. Another advantage of BAW resonator is that device design and the piezoelectric film material properties determine their Qs.

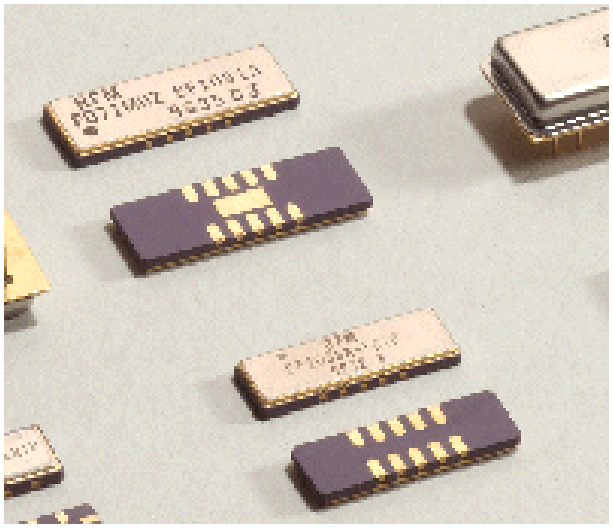

Figure 1.4: Surface acoustic wave filters.

1.3 BULK ACOUSTIC WAVE (BAW) RESONATOR

The filters can be realized using the traditional resonator technologies such as LC, ceramic resonators and transmission line resonators connected in networks of a certain topology. However, they become too large or are difficult to meet the performance requirements when the

operation frequency increases to GHz range. The advantage of acoustic wave filters over electromagnetic filters is generally recognized as their small size resulting from the approximately five orders of magnitude reduction in the acoustic wave velocity. Bulk acoustic wave resonators have such unique advantages since they are at least an order of magnitude smaller than dielectric resonators or lumped elements, and possess much lower insertion loss than surface acoustic wave devices [11].

For traditional electroacoustic resonator technologies in the microwave region, only the bulk single crystalline piezoelectric materials can be used. However the choice of these materials is rather limited and they are not compatible with the existing IC technology. Furthermore, in order to increase the operating frequency, the only way is to decrease the dimension of the bulk materials while its acoustic wave velocity is determined uniquely by the material properties, which will result in the enormous increase of the fabrication cost. In recent years, the MEMS and film deposition technologies have been introduced to the BAW resonator area, which extend the application fields of electromechanical BAW devices to GHz frequency range. Instead of attenuating the crystal plates to micrometer thicknesses, the piezoelectric thin films can be grown onto the specific substrate to meet the thickness requirement in resonator fabrication. Since various piezoelectric films can be deposited on a lot of substrates and the highly developed thin film technologies can grow piezoelectric films with high uniformity and controlled properties on the substrates, the new film BAW devices have more advantages than the traditional devices. It should be pointed out that by far the greatest potential of fabrication and performance of the BAW resonator is that it opens the very promising possibility of integrating the traditionally incompatible IC and electroacoustic technologies. This in turn will bring about a number of substantial benefits such as significant decrease in the fabrication cost of the final device, easier

and simpler device design as well as increased sensitivity, reduced insertion loss, low power consumption, small device size, reduced material use, less electromagnetic contamination, etc. Another very significant benefit of this integration would be the mass fabrication of highly sensitive, low cost integrated chemical and biological sensors and electronic tags that can be use as environmental controller and monitor. Agilent Technologies is the first company to start mass production of discrete FBAR device [12].

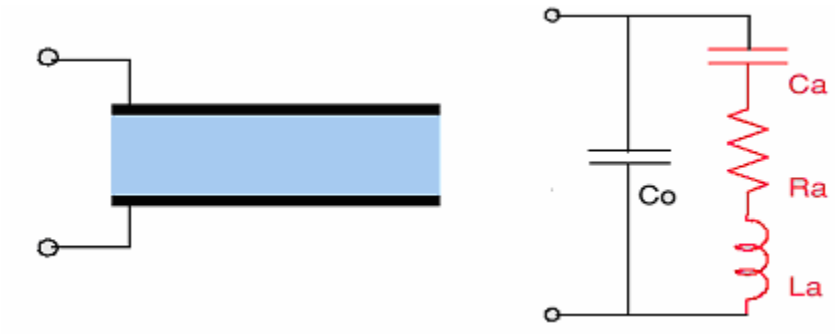

(a) (b)

Figure 1.5: Crystal resonator (a) Resonator structure, (b) Equivalent circuit around any primary resonance.

A traditional configuration of the crystal resonator is shown in Fig. 1.5(a) while the Butterworth Van Dyke (BVD) equivalent circuit is shown in Fig. 1.5(b). The resonator is in the form of a simple capacitor which has a piezoelectric material for the dielectric layer and suitable top and bottom metal electrodes. The simplified equivalent circuit of the piezoelectric resonator has two arms. C_0 is the geometric capacitance of the structure and the R_a, L_a, C_a portion of the circuit is called the "motional arm," which arises from the mechanical vibrations of the crystal. The series elements R_a, L_a, C_a which are controlled by the acoustic properties of the device, account for the motional loss, the inertia and the elasticity respectively.

For the thin film bulk acoustic wave resonator, the optimal resonator design requires the acoustic wave to be confined into the piezoelectric material layer in order to produce a very high Q device. Most piezoelectric FBAR are of the thickness mode type, meaning that the bulk acoustic wave is reflected within the piezoelectric thin film and spread in the thickness direction. The boundary conditions require the waves to be reflected at the surfaces, which are perpendicular to the thickness direction, with great efficiency in order to maintain high quality factor Q [13]. In fact, acoustic wave can travel in the hard solid materials with a typical velocity of 5000m/s. As a result, the acoustic impedance of the air is 10^5 times lower than that of the hard solid material and the 99.995% of the acoustic wave energy will be reflected at the solid/air interface. For example, traditional quartz crystal resonator can trap the energy inside the vibration plate using this method and its resonance frequency can up to 100MHz. For higher frequency requirement, the FBAR is one kind of solution. Some of the principles of quartz resonator have been extended to the FBAR using in the higher frequency region. Since the thickness of the piezoelectric film is only a few microns or thinner, the effect of the electrodes and support layers are considerable increased in the performance of the resonator. Several papers have been published on different practical structures and topologies of thin film resonators including membrane type acoustic resonator, air gap resonator, and the solidly mounted acoustic resonator (SMR) [14-17].

Backside etching of the substrate is used to form the membrane type acoustic wave resonator shown in Fig. 1.6(a). The membrane structure has two air interface reflecting surfaces that are similar to the ideal, free air structure shown in Fig. 1.5. Typical fabrication process for the membrane structure includes deposition of an etch-stop layer followed by the deposition of bottom electrode, piezoelectric layer and top electrode for the resonator. A backside etching is

then used to remove portion of the substrate to free the membrane. A disadvantage of the membrane type acoustic wave resonator structure is the possibility that backside etching process might not be compatible with previously fabricated circuits on the same substrate. The membrane needs to be strong to withstand any post processing. Since the membrane structure is lack of the ability to dissipate heat, it is not suitable for use in high power circuits.

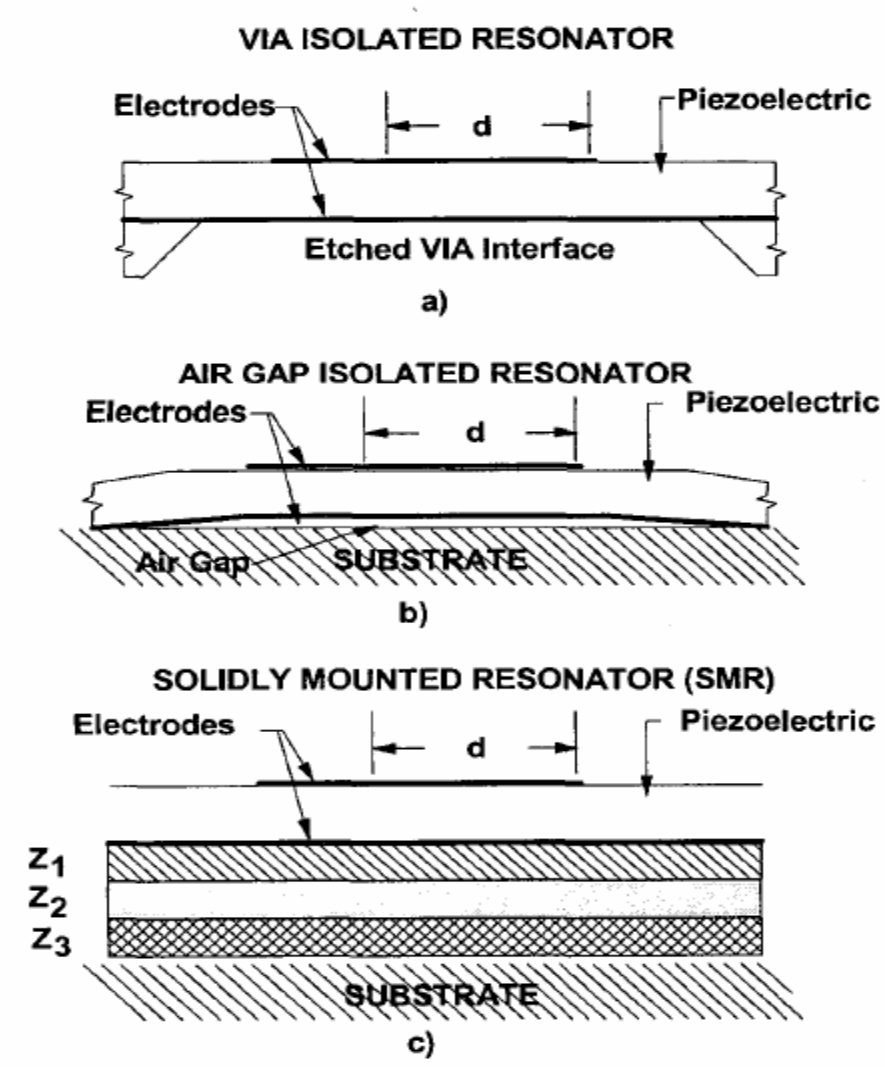

Figure 1.6: Typical BAW resonator configurations [8].
(a) Membrane type, FBAR (b) Air gap type, FBAR (c) SMR type

The air gap resonator structure can be achieved by using an undercut etching to form a bridge structure. In the processing, a sacrificial support layer is deposited before sputtering the resonator layer, i.e., the piezoelectric layer. After the fabrication process for the top resonator material, the sacrificial layer is etched away to form a structure which is supported at the edges but is free from the substrate in the resonator active region. The internal strain can affect this structure to make it somewhat fragile. Like the acoustic membrane structure, it's difficult to dissipate heat in high-power circuit when using the air gap resonator structure. Since backside etching process is not required, the air-bridge structure can be used with a larger number of substrates. Fig. 1.6 (b) shows the air gap resonator structure.

To achieve mechanical resonance in a resonator structure, an acoustic isolation to the surrounding media is required so that a large standing wave can be obtained. Since the achievable mechanical acoustic impedance ratio of the common piezoelectric materials to the corresponding substrates is small, the piezoelectric material layer cannot be directly deposited on the substrate in order to obtain a high Q resonator which requires the acoustic impedance on both sides of the resonator be approximately zero. The solidly mounted resonator structure provides zero acoustic impedance for the top interface and an acoustic impedance of almost zero for the bottom interface where the acoustic reflector layer reflect the acoustic wave back to the piezoelectric layer. The reflector can be composed of several layers with alternating values of high and low acoustic impedance and a thickness equivalent to a quarter wavelengths at the main resonance frequency. During resonator operation, at any of the interfaces between high and low impedance layers a large percentage of the wave will be reflected and sum up with correct wave phase since the thickness of each layer is $\lambda/4$. It presents an apparent zero impedance at the interface as the case in the ideal free air resonator structure. Since the bridge structures are not

required, SMR device can be fabricated after all other active devices are achieved and passivated. The schematic structure of SMR is shown is Fig. 1.6 (c).

1.4 TYPES OF BULK ACOUSTIC WAVE FILTER

BAW filter can be achieved by electrically connecting several BAW resonators in a certain topology or by stacking the acoustically coupled resonators on top of each other. Typically, two groups of resonators with different resonance frequency are sufficient to make a filter.

RF signals related to ground are single-ended and unbalanced while other balanced RF signals are differential and symmetrical. Balanced components require two connections at each port, which carry identical signals with opposite sign. Balanced signals are less vulnerable to interference and crosstalk because interfering signals will only generate common mode amplitudes and be cancelled out in a differential evaluation. Bandwidth and insertion loss are two critical parameters for the application of the RF filter. The relative width of the frequency bands for cellular phones is typically between 2% and 4.3%. A maximum insertion loss of 3-4 dB throughout the whole passband and the application temperature range from -30 to 85°C should be guaranteed. BAW filters can fulfill all the requirements for cellular phone systems. The most straightforward BAW filters to be made are single-ended input and single-ended output filters and also filters using balanced signals at both input and output ports. The different BAW filters types include ladder filters, lattice filters, stacked crystal filters (SCF), and coupled resonator filters (CRF). The ladder filters and lattice filters will be reviewed below.

Ladder-type filters can be used both for single-ended and balanced signals. Only the single-ended type as shown in Fig. 1.7 is reviewed here. The two groups resonators used in the ladder

filters are series resonators and shunt resonators. The base structure that is composed of one series resonator and one shunt resonator is called a “stage”. The ladder filters consist of multiple stages. The working principle of the ladder filter is shown in Fig. 1.8. f_{detune} is the parallel resonance frequency difference between series resonator and shunt resonator. In the center of the pass band, the impedance of the series resonator is small which allow the RF signal pass by. On the other hand, the shunt resonator has large impedance which will prevent the signal passing by. Typical values for f_{detune} are 60-80% of the passband width, which means the series resonance frequency of the series resonator is close to the parallel resonance frequency of the shunt resonator. For ladder filters, the transitions to the upper and lower stopbands are steep. The greatest challenge in ladder BAW filters for the relative high bandwidth applications is to get the sufficient effective coupling coefficient.

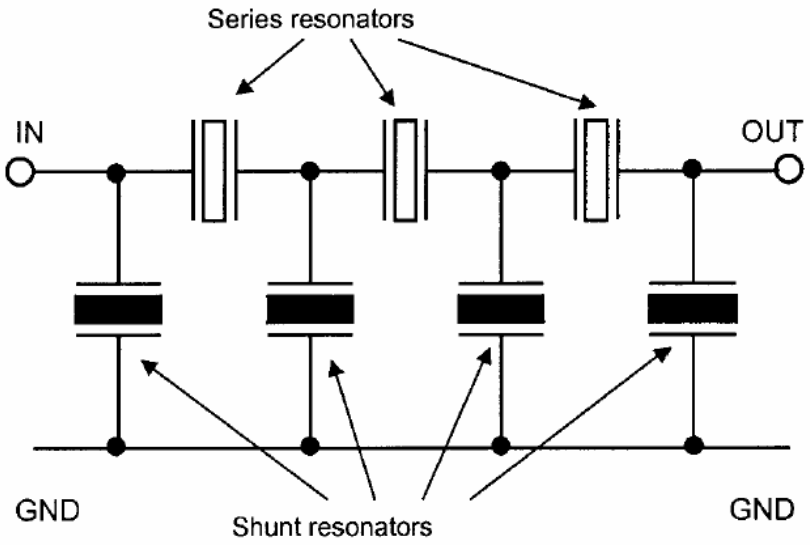

Figure 1.7: Topology of a ladder filter.

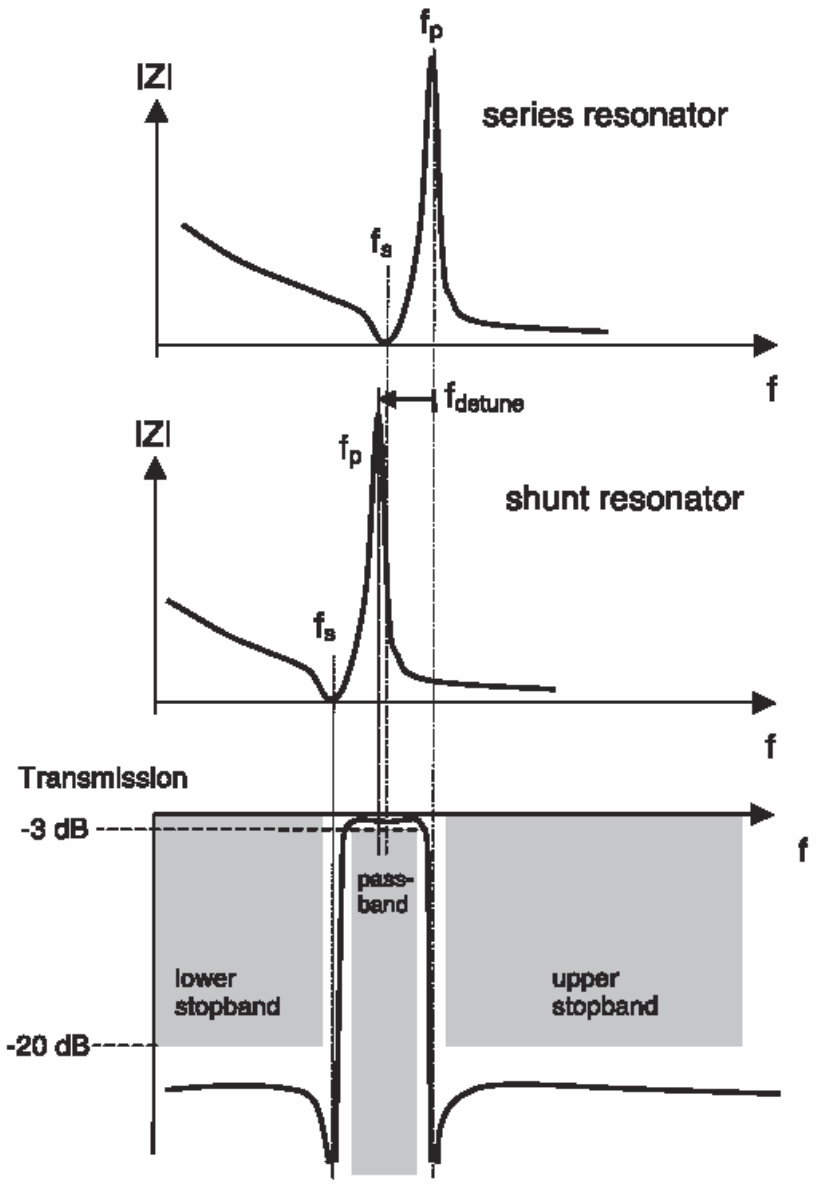

Figure 1.8: Working principle of a ladder filter.

Lattice-type is a suitable filter topology for BAW filters as shown in Fig. 1.9. However, this kind of filters works properly only when both the ports are balanced. In a lattice BAW filter, each stage consists of a bridge-type structure with four resonators which are two series resonators and two shunt resonators. As in the ladder filters, the difference of the resonance frequency is detuned by f_{detune}. The working principle of the lattice is that either the serious

resonators or the shunt resonators pass the signal to the output at $f_{s,shunt}$ or at $f_{s,series}$, respectively. If serious and shunt resonator have the same size, the far stopband will have almost infinite attenuation because the bridge is in perfect balance. The width of passband can be 30% larger than that of the ladder filters which use the resonators with the same effective coupling coefficient and Q factor. The insertion loss of such a lattice filter is also far less than that of the ladder filters. One disadvantage of the lattice filters is that the transitions to the stopbands are not steep.

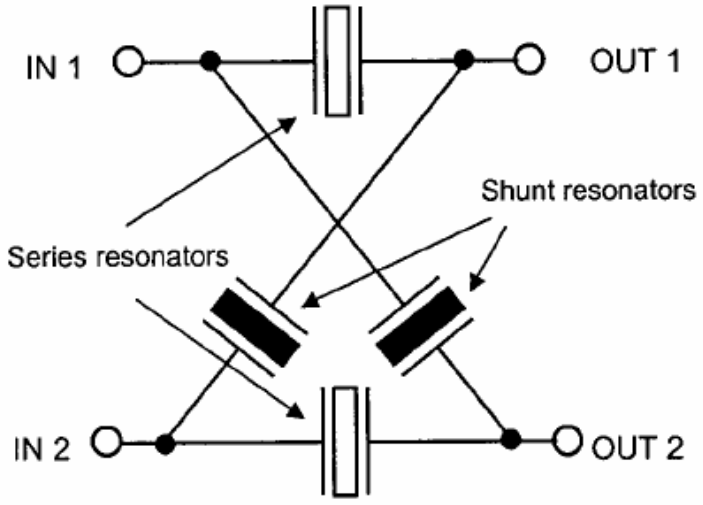

Figure 1.9: Topology of a lattice filter.

1.5 BASIC THEORY AND PARAMETERS OF BAW RESONATORS

Acoustic wave travels in the solid with different types: bulk longitudinal (compressional) wave, whose principal polarization is along the direction of propagation, and transverse (shear) wave, whose principal polarization is perpendicular to the propagation direction. These waves

are shown in Fig. 1.10(a) and (b). By imposing different boundary conditions to the equation of motion, different types of wave can be obtained such as the surface acoustic wave. A surface acoustic wave (SAW) can propagate along the surface of a semi-infinite solid as shown in Fig. 1.10(c). In the SAW mode, the particle near the surface has the largest displacement, while the particle motion decreased to nearly zero at a depth of about one wavelength. In both cases, the velocity of SAW and BAW in the homogeneous substrate is independent of frequency. This property is very important to the acoustic wave devices based on these two modes [18].

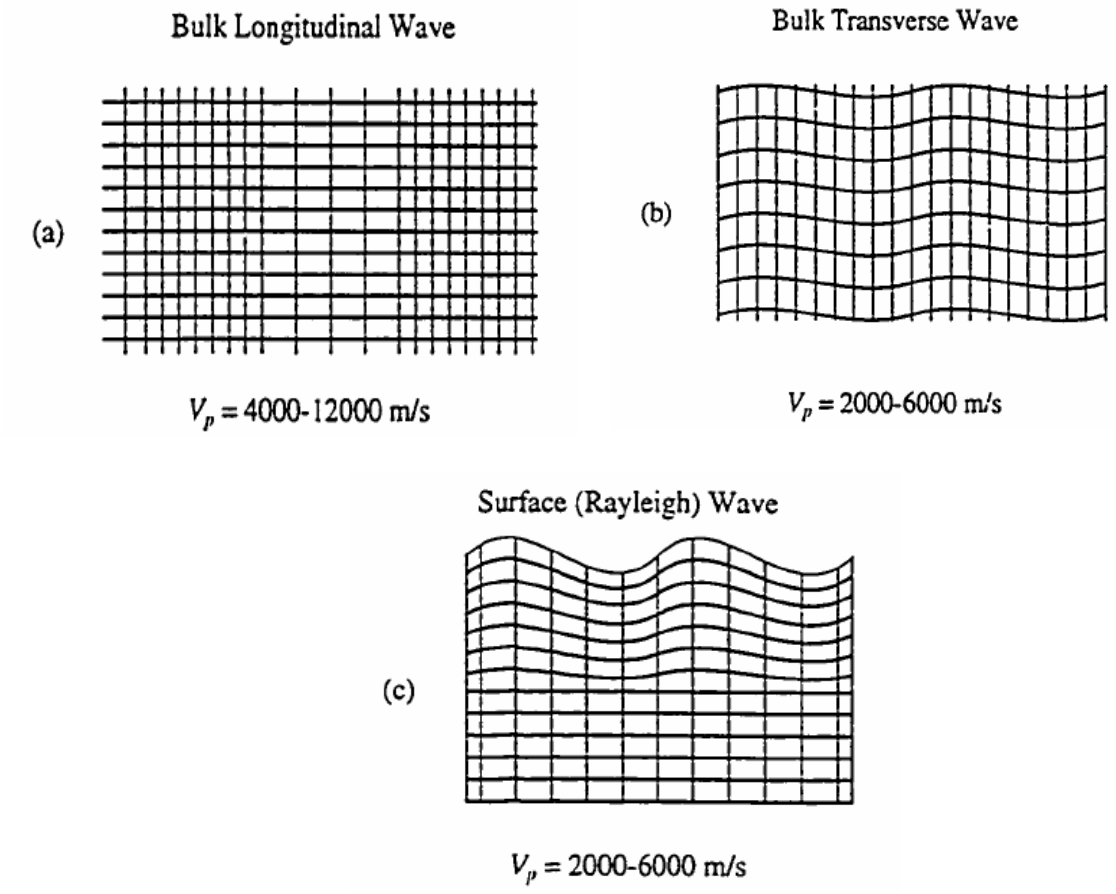

Figure 1.10: Schematic representations of elastic waves in solids with typical wave speeds, $V_{p,}$ for each case [18]

Traditionally, resonators have been excited with the external electric field parallel to the resonator plate normal (thickness excitation, TE) direction or perpendicular to the plate normal (lateral field excitation, LTE) direction. Due to the piezoelectric effect, the velocity of propagation of acoustic waves in piezoelectric media is higher than in the non-piezoelectric case. It is a common practice to modify the stiffness tensor by considering adding the piezoelectric and permittivity tensor elements, in order to calculate the impact of piezoelectricity in the velocity of propagation of the wave. The stiffness constants in that case are referred to as "stiffened" constant. It should be known that the piezoelectric corrections to the stiffness matrix depend not only on the piezoelectric coefficient matrix, but also on the direction of propagation. A crystal may be strongly piezoelectric for a given direction while the effect is completely absent in a different direction. The stiffened phase velocity is:

$$v' = \sqrt{\frac{c'^{E}}{\rho}} = \sqrt{\frac{c^{E} + e^{2}/\varepsilon^{S}}{\rho}} \tag{1.1}$$

where c is the elastic stiffness constant, e is the piezoelectric constant, ε is the permittivity, and ρ is the mass density. The superscript E and S represent that electric field and strain are held constant.

For comparison, the unstiffened phase velocity is:

$$v = \sqrt{\frac{c^{E}}{\rho}} \tag{1.2}$$

Rewriting equation (1.1) to

$$v' = v(1 + K^{2})^{1/2} \tag{1.3}$$

where

$$K^{2} = \frac{e^{2}}{\varepsilon^{S} c^{E}} \tag{1.4}$$

is called the piezoelectric coupling constant. The electromechanical coupling coefficient is also defined:

$$k_t^2 = \frac{e^2}{\varepsilon^S c^D} = \frac{K^2}{K^2 + 1} \tag{1.5}$$

Consider the structure shown in Fig. 1.5(a), where the acoustic wave propagating in the direction parallel to the external electric field. In this case, the longitudinal displacement vector is precisely zero in the piezoelectric medium. Therefore, the acoustic wave propagation in this configuration requires that we use c^D in place of c^E, where

$$c^D = \frac{e^2}{\varepsilon^S} + c^E \tag{1.6}$$

In the TE mode, the propagating acoustic wave generates an electric field in the piezoelectric crystal and vice versa. Hence the wave propagation is regarded as stiffened and the coefficient, given by k_t, is used to express the coupling in BAW devices in this mode.

Quality factor Q is a measure of the energy dissipation within the system, indicating how well mechanical energy input to the resonator remains confined there during the oscillatory motion. The loss mechanisms that effect Q can take many forms including friction, fluid damping, and material dependant thermoelastic damping. With a force applied at its resonance frequency, a resonator with an infinite Q would vibrate with ever-increasing amplitude, never losing energy to its surroundings, and continue to vibrate indefinitely once the applied force was removed. Conversely, with a Q approaching zero, the resonant frequency of a device would be virtually undetectable. The vibrations at the resonant frequency would have the same magnitude as those away from it and vibrations would die out immediately if the excitation force was removed.

The Q of a resonator is important, as it affects many of the performance characteristics of the system in which the device is used. For example, in an oscillator, the Q directly affects the accuracy of the frequency produced. The frequency of a signal source will vary with the change in time for a resonator with a low Q, while a resonator with a very high Q will show far less variation.

In general, Q can be determined by

$$Q = \frac{f_0}{BW_{3dB}} \tag{1.7}$$

where BW_{3dB} is the 3dB bandwidth of the resonator; that is, the bandwidth at which the mechanical energy stored in the oscillations has been reduced to half that of the peak. The Q is also directly related to other common measures of loss, the damping ratio ξ, by

$$Q = \frac{1}{2\xi} \tag{1.8}$$

The amplitude of the vibration increases with the increase of Q as does the sharpness of the resonance peak. It is this sharp peak in mechanical response which gives mechanical resonators their excellent selectivity in communication systems.

The design and manufacture of the on-chip thin film bulk acoustic wave filter depends on several factors, including thin film material quality, physical structure of resonator elements, and filter topology. The commonly used figure of merit (M) in resonator design is defined as [19]

$$M = \frac{Q}{2C_r} \tag{1.9}$$

where Q is the quality factor of the resonator and C_r is the ratio of the clamped capacitance C_0 to the motional capacitance C_a of the resonator. For Nth harmonic, C_r is given by

$$C_r \cong \frac{N^2\pi^2}{8k_t^2} \tag{1.10}$$

and

$$C_r \cong \frac{f_s}{2\Delta f} \tag{1.11}$$

where k_t is the coupling coefficient, f_s is the series resonant frequency, and Δf the bandwidth. Since C_r is inversely proportional to the coupling coefficient, equation (1.10) implies that the maximum achievable fractional bandwidth of the resonator is limited by properties of the piezoelectric material. Also, as can be seen form the equations, for wideband filter application, the parameter M will increase with the decrease of C_r and therefore high coupling coefficient k_t is required in the system. Thus, candidate piezoelectric materials should have high electromechanical coupling coefficient. It can also been seen, however, that for frequency control applications the figure of merit is weighted toward high Q.

1.6 PIEZOELECTRICITY

Since the piezoelectric materials have been widely used in the BAW resonators and filters, it is essential to understand the piezoelectricity effect of the materials. Piezoelectricity is a widely used physical effect that has its name derived from the Greek word piezein, meaning to apply pressure. Certain classes of crystals exhibit the particular property of producing an electric field when subjected to an external force of pressure. They also expand or contract in response to an externally applied voltage. Brothers Pierre and Jacques Curie first discovered this effect in α-quartz crystal in 1880 [20]. The piezoelectric effect reflects the coupling between the mechanical energy and the electric energy domain of the material. Its first practical application was in the

1920s when a Frenchman, Langevin, developed a quartz transmitter and receiver for underwater sound—the first sonar. Piezoelectric crystals are common in many modern applications, for example, as clock oscillators in computers and as ringers in cellular telephones. They are attractive for MEMS because they can be used as sensors as well as actuators.

The piezoelectric crystals can produce an electric polarization or electric charge when a proportional mechanical force (or strain) is applied between some faces. This phenomenon is called “direct” piezoelectric effect. Complementary to this is the “converse” piezoelectric effect: the application of the voltage to the crystal can also change its shape. There are 32 typical crystalline classes of which 21 are non-symmetric and 20 of those exhibit the piezoelectric effect. Because the piezoelectric effect is by definition linear, there are only 18 possible coupling coefficients of which not all are necessarily non-zero. Of course, all piezoelectric materials do not necessarily fall into these categories; for example, there is the polymer material PVDF that is also a piezoelectric material.

The physical origin of piezoelectricity is explained by charge asymmetry within the primitive unit resulting in the formation of a net electric dipole. Adding up these individual dipoles over the entire crystal gives a net polarization and an effective electric field within the material. Crystal symmetry plays an important role: only a crystal that lacks a center of symmetry can have the piezoelectric properties. A crystal with a center of symmetry, such as a cubic crystal, is not piezoelectric because the net electric dipole within the primitive unit is always zero, no matter if there is an externally applied stress.

For linear piezoelectric material, the general constitutive equations are used to describe the relations between mechanical and electrical variables. The key components that make up the constitutive equations illustrate the relationships between the terms such as Stress (T), Strain (S),

Electric Field (E), and Dielectric Displacement (D). Stress and strain are defined by second rank tensors while vectors define the electric field and dielectric displacement. Thus, Mechanical stress T_{ij}, mechanical stain S_{ij}, electrical field E_i and electrical displacement D_i are the variables used in the equations. Depending on the variable choice, the following four sets of constitutive relations are defined:

$$\begin{cases} S_{ij} = s^{E}_{ijkl} T_{kl} + d_{kij} E_k \\ D_i = d_{ijk} S_{jk} + \varepsilon^{T}_{ij} E_j \end{cases} \quad \text{i, j, k, l=1 to 3} \tag{1.12}$$

$$\begin{cases} T_{ij} = c^{E}_{ijkl} S_{kl} - e_{kij} E_k \\ D_i = e_{ijk} S_{jk} + \varepsilon^{S}_{ij} E_j \end{cases} \tag{1.13}$$

$$\begin{cases} S_{ij} = s^{D}_{ijkl} T_{kl} + g_{kij} D_k \\ E_i = -g_{ijk} T_{jk} + \beta^{T}_{ij} E_j \end{cases} \tag{1.14}$$

$$\begin{cases} T_{ij} = c^{D}_{ijkl} S_{kl} - h_{kij} D_k \\ E_i = -h_{ijk} S_{jk} + \beta^{S}_{ij} D_j \end{cases} \tag{1.15}$$

where s_{ijkl}, c_{ijkl}, ε_{ijkl} and β_{ijkl} are elastic compliance constant, elastic stiffness constant, dielectric permittivity constant, and dielectric impermittivity constant. d_{ijk}, e_{ijk}, g_{ijk} and h_{ijk} *a*re piezoelectric coefficients which can be converted into each other. The superscript *T, S, D,* and *E* mean that the stress, strain, dielectric displacement and electric field are held constant.

The particular pair of equations utilized will depend upon the consideration of which constants are known or measurable, and the application for which they are required.

A set of equations relating the constants is given by

$$d_{ijk} = e_{ilm} s^{E}_{lmjk} = g_{ljk} \varepsilon^{T}_{il} \tag{1.16}$$

$$e_{ijk} = d_{ilm} c^{E}_{lmjk} = h_{ljk} \varepsilon^{S}_{il} \tag{1.17}$$

$$g_{ijk} = h_{ilm} s^{D}_{lmjk} = d_{ljk} \beta^{T}_{il} \tag{1.18}$$

$$h_{ijk} = g_{ilm} c^{D}_{lmjk} = e_{ljk} \beta^{S}_{il} \tag{1.19}$$

The constitutive constants are dependent upon the boundary conditions. For example, if a material is short circuited, then the electric field potential existing across the material is to be zero; however, if subjected to an open circuit, then a capacitor is formed. [21]

When evaluating both the direct and converse piezoelectric effect, the constant most typically used (and easily measured) is the piezoelectric strain coefficient *d*. the electromechanical coupling associated with this constant can be best illustrated conceptually by the relation

$$d = (D / T)^{E} = (S / E)^{T} \tag{1.20}$$

The group of constants which relates strain in a given direction to the applied voltage of any other direction (under constant stress) is called the piezoelectric strain coefficient. These constants are identified through the following relationship:

$$S_{kl} = d^{T}_{ilk} E_{i} \tag{1.21}$$

Alternatively, *d* may also be called the piezoelectric charge coefficient. In this case, it would then express the surface charge density as a function of a stress field while the electric potential is held constant. This is express by

$$D_{i} = T_{kl} d^{E}_{ilk} \tag{1.22}$$

If the material is subjected to a hydrostatic condition, the constant *d* may be turns out to have a higher overall value. A large value of *d* is generally considered preferable when actuation is required.

Similarly, the constant *g* is known as the voltage coefficient. This constant relates the field produced as the result of an imposed stress under open circuit condition.

$$E_j = -g^D_{jkl} T_{kl} \tag{1.23}$$

To attain a large voltage for a given stress state, as for a sensor application, this constant will need to be as large as possible. The constant *g* may also be used to indicate the strain produce due to an applied charge per unit area, given a stress free state, and can then be termed as a strain coefficient.

Two more piezoelectric constants can also be identified. These relate the stress proportionally to the voltage and the voltage proportionally to the strain, as following

$$T_{ij} = -e^S_{kij} E_k \tag{1.24}$$

$$E_j = -h^D_{jkl} S_{kl} \tag{1.25}$$

These equations are analogous to those for the constants *d* and *g*.

As discussed above, the physical properties of the crystal are described by tensors. Since tensors are inherent symmetric, they are often expressed in matrix notation for brevity. The compressed matrix notation consists of replacing *ij* and/or *kl* by *p* and/or *q* with: 11→1, 22→2, 33→3, 23=32→4, 13=31→5, 12=21→6. The following relationships exist between the tensors expressed by two different notations.

$s^E_{pq} = s^E_{ijkl}$ when i=j, k=l and p, q=1, 2, 3

$2s^E_{pq} = s^E_{ijkl}$ when i=j, k≠l and p=1, 2, 3 and q=4, 5, 6

$4s^E_{pq} = s^E_{ijkl}$ when i≠j, k≠l and p, q=4, 5, 6

$d_{iq} = d_{ikl}$ when k=l and q=1, 2, 3

$2d_{iq} = d_{ikl}$ when k≠l and q=4, 5, 6

For the piezoelectric material aluminum nitride (AlN) discussed in this study, its symmetry can be expressed by point group 6mm. There are 10 non-zero independent coefficient exist, i.e. d_{31}, d_{33}, d_{15}; ε_{11}, ε_{33}; s_{11}, s_{12}, s_{13}, s_{33}, s_{44}. If expressed in matrix form, they are:

$$[d]=\begin{bmatrix} 0 & 0 & 0 & 0 & d_{15} & 0 \\ 0 & 0 & 0 & d_{15} & 0 & 0 \\ d_{31} & d_{31} & d_{33} & 0 & 0 & 0 \end{bmatrix} \tag{1.26}$$

$$[\varepsilon]=\begin{bmatrix} \varepsilon_{11} & 0 & 0 \\ 0 & \varepsilon_{11} & 0 \\ 0 & 0 & \varepsilon_{33} \end{bmatrix} \tag{1.27}$$

$$[s]=\begin{bmatrix} s_{11} & s_{12} & s_{13} & 0 & 0 & 0 \\ s_{12} & s_{11} & s_{13} & 0 & 0 & 0 \\ s_{13} & s_{13} & s_{33} & 0 & 0 & 0 \\ 0 & 0 & 0 & s_{44} & 0 & 0 \\ 0 & 0 & 0 & 0 & s_{44} & 0 \\ 0 & 0 & 0 & 0 & 0 & s_{44} \end{bmatrix} \tag{1.28}$$

For the piezoelectricity, the piezoelectric coupling factor, or energy ratio, is considered to be a good indicator of the efficiency of the material's piezoelectric capability. This constant is defined by its square such that

$$\begin{aligned} k_{ijk}^2 &= \frac{\textit{mechanical energy converted to electric energy}}{\textit{input mechanical energy}} \\ &= \frac{\textit{electric energy converted to mechanical energy}}{\textit{input electric energy}} \end{aligned} \tag{1.29}$$

The subscripts may be neglected on the whole, or may be considered for a particular cause and effect relationship where i and jk reflect the electric and mechanical components respectively. For example, considering the particular mode that only T_1 is the only non-zero item

for the stress tensor. This mode is induced by the electric field E_2 through d_{12}. Then the piezoelectric coupling coefficient is $k_{ijk}^2 = \frac{d_{21}^2}{s_{11}^E \varepsilon_{22}^T}$.

This constant is somewhat like an efficiency rating parameter which indicates what percent of the energy put in is transferred to the desired effect. The energy conversion are dependent upon the boundary conditions and are sensitive to certain variables, such as frequency, and therefore is somewhat application specific.

1.7 PIEZOELECTRIC MATERIALS

After the piezoelectric effect was discovered in quartz crystal, many materials with piezoelectric property are discovered and synthesized. Nowadays, quartz is still a widely used piezoelectric material for overall stability with respect to time and temperature and is noted for its frequency control capabilities. Quartz is naturally piezoelectric (non-ferroelectric) with an essentially linear response, even when very high electric or stress fields are imposed. However, there are no available methods to deposit crystalline quartz as a thin film over silicon substrates. Piezoelectric ceramics are also common. Lithium niobate ($LiNbO_3$) and barium titanate ($BaTiO_3$) are two well-known matereials, but they are also difficult to deposit as thin films. Polyvinylidenefluoride (PVDF) is the piezoelectric polymer material that was first discovered in 1969. PVDF has fairly strong piezoelectric property and is chemical stable.

A large part of the research of BAW resonator are focus on the development of novel functional material (piezoelectric, ferroelectric, etc) with superior electromechanical properties allowing the fabrication of high frequency devices with improved performance and at low fabrication cost at the same time. High electromechanical coupling coefficient, low

electromechanical losses, high thermal stability, and the compliance with the IC technology become the main concern for these new materials. Nowadays, the most popular piezoelectric materials for BAW applications are lead zirconate titanate (PZT), zinc oxide (ZnO) and aluminum nitride (AlN).

1.7.1 Lead Zirconate Titanate (PZT)

PZT has been the widely used piezoelectric ceramic since the late 1950s, due in part to its ability under increased temperature. PZT material can be manufactured by many techniques such as sintering and sol-gel methods. For example, the PZT can be synthesized from powders which are first pressed and then sintered in the oven at 1350°C to produce the ceramic. After the process of sintering, the material needs to be poled. A high DC electric field is exerted cross the ceramic by using the electrodes (e.g., silver) which are adhered to the ceramic plate surface. However, if the poled ceramic is subjected to a high AC field, excessive stress, or if the Curie point exceeded, the material may be de-poled. [21]

By varying the amounts of the components and/or by using dopants, PZT ceramics can provide a wide range of piezoelectric attributes. These attributes are typically classified as “soft” and “hard” properties. Soft PZT compositions have the advantage of providing relatively large stain due to their high *d* constant (as high as 0.07 percent), but on the downside, soft materials often exhibit large nonlinearities which include hysteresis, aging, and heating effects. Hard PZT is typically used in sensor application due to its high *g* constant and generally exhibits very linear behavior, but due to their higher stiffness, hard PZTs typically cannot provide strains higher than 0.03 percent which limits their application as an actuator. Both types of PZT, however, do have common attributes. Their fast response time (on the order of microseconds) is one of the most

valued properties of the material. Thus, a piezoelectric actuator's resolution made by PZT is only limited by its controlling electronics. Because piezoelectric ceramics are capacitive devices, their power consumptions are minimal. In addition to these attributes, PZT has the ability to operate in a wide temperature range.

Sputtering PZT is difficult because it requires the control of the stoichiometry of lead, zirconium and titanium accurately. Nowadays PZT has been successfully applied to MEMS by using sol-gel process.

1.7.2 Zinc Oxide (ZnO)

ZnO has many excellent physical properties which make it can be used in many areas. ZnO has a wide and direct band gap of 3.37eV at room temperature. ZnO is known to have wurtzite structure with lattice constant a=3.249 Å, c=5.207Å. Its large exciton binding energy (60meV), which is much greater than the thermal energy at room temperature, makes it a promising candidate for applications in blue-UV light emission and room-temperature UV lasing. ZnO is attracting attention as a semiconductor with piezoelectric property which can be used for gas sensor, biosensor, surface acoustic wave devices, transducers, and transparent thin film transistors. It is also attractive for forming various types of nanorods, nanowires, and nanotubes for observation of quantum effects. Nowadays, Many ZnO nanocrystals are fabricated by various methods [22-24].

1.7.3 Aluminum Nitride (AlN)

Aluminum nitride, AlN, does not occur in nature. F. Briegleb and A. Geuther first prepared it in 1862 by heating aluminum in a nitrogen atmosphere at 700°C. In more recent work, AlN was

prepared at high temperature. However, there was disagreement on many of its properties such color and oxidation resistance.

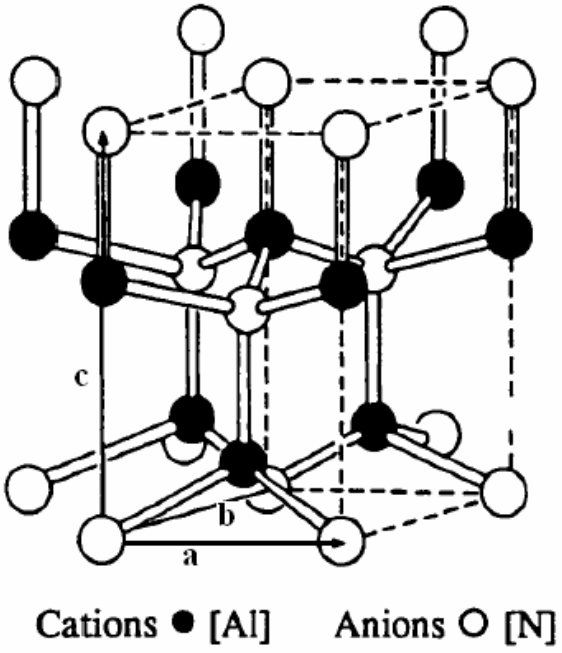

Figure 1.11: The crystal structure of AlN [25].

Aluminum nitride is a wide band gap material, and can crystallize in both wurtzite and zinc-blende structures. Hexagonal wurtzite structured AlN has a direct room temperature bandgap of 6.2eV. Cubic zinc-blende structured AlN has an indirect bandgap. The wurtzitic AlN is the stable crystal structure at ambient temperature with the lattice constants: a= 3.111Å and c=4.978 Å. While the theoretical estimate of the lattice parameter of zinc-blende structured AlN is a= 4.38Å. The AlN wurtzite crystal structure is shown in Fig. 1.11.

Hexagonal wurtzite structured AlN attracted much interest because of its material properties stability. Aluminum nitride is one of the few nonmetallic solids with a high thermal conductivity with a high theoretical value of 320W/m·K [25]. The high thermal conductivity of AlN makes it

a successful packaging material to remove the heat generated in the wafers in silicon microelectronics technology. Thermal conductivity will be decreased by adding oxygen to the AlN lattice which causes a vacancy on the aluminum atom site. For application in micro electronic devices, thermal expansion coefficient is an important parameter. A mismatch of the thermal expansion coefficients between the thin film and the substrate may induce the distortion of the substrate and film. The thermal expansion coefficients of AlN over the temperature range from 20-800°C are $5.3 \times \times 10^{-6}$/ °C and $4.2 \times \times 10^{-6}$/ °C along a axis and c axis respectively [26]. Under the definition of lattice misfit: f=2(b-a)/(a+b), where a and b are the lattice parameters of the substrate and the film respectively, the hexagonal AlN (002) has 22.3% lattice misfit with cubic silicon (111). But the thermal expansion coefficient of AlN is well matched to that of silicon from room temperature to 200 °C. Its thermal expansion coefficient is also closer to that of GaAs than either SiO_2 or Si_3N_4. Thus AlN has potential application in silicon based IC area.

AlN has high thermal stability (up to 2200°C), high resistivity, and a high breakdown voltage (14kV/mm). The melting temperature of AlN is as high as 3073K under 100 atmospheres of nitrogen. In addition, it has very high hardness, high optical transmission (0.2-12.5μm) and good chemical stability.

Wurtzite AlN alloyed with GaN may span a continuous range of direct band gap energies throughout the visible spectrum into the ultraviolet (UV) wavelengths. Such a nitride system is promising for optoelectronic device applications, such as light emitting diodes (LEDs), laser diodes (LDs), and detectors, which are active in the green, blue or UV wavelengths [27]. The wide bandgap group III nitride (GaN, AlN and InN) semiconductors and their alloys have the potential applications for high power electronic devices. Their unique material properties, i.e., high electric breakdown field, high electron saturation drift velocity and negative electron

affinity demonstrate their tremendous potential in high power device application. As they are exceptionally chemically stable, they are also suitable in harsh chemical environments. [27, 28]

AlN thin film is a common buffer layer in the growth of GaN film to improve the material quality due to their close lattice and thermal match. It is very difficult to grow GaN film on Si substrate because of the large mismatches in lattice constant and thermal expansion coefficient, and because of the chemistry between GaN and Si. In addition, the GaN growth on sapphire substrate also takes the advantage of highly c-axis oriented AlN buffer layer. Smooth and low defect density buffers, such as AlN thin films, are required to grow high quality GaN.

Due to the high static dielectric constant ε_r of 8.5, the growth of high quality AlN layers as insulators has benefits for devices with insulated gates such as metal-insulator-semiconductor field effect transistor (MISFET) and insulated gate-field effect transistor (IGFET). More recently, AlN has been used as a barrier layer in multi-layers Co/AlN/Co and NiFe/AlN/NiFe. It was demonstrated that AlN could be a useful alternate barrier material. AlN is also promising for ferromagnetic/dielectric magneto-optical due to its high refractive index [27].

The crystal structure, such as the preferred orientation, determines the performance of the AlN film. For the (002) oriented AlN films, the c-axis is normal to the substrate surface and the plane parallel to the substrate surface is the closest packed basal plane, with either all Al atoms or N atoms. The (002) oriented AlN films are useful in the BAW resonators since they have the highest piezoelectric stress constant is this direction. On the contrary, for (100) and (110) oriented AlN films, the c-axis is parallel to the substrate surface and the non-close packed planes consisting of an equal number of aluminum and nitrogen atoms parallel to the substrate surface. The (100) oriented AlN thin films are promising materials for surface acoustic wave devices.

AlN is promising for SAW and BAW device application due to its high sound velocity, and piezoelectricity. AlN has nearly twice the SAW velocity as that of quartz and $LiNbO_3$. Table 1.1 lists some important material properties of the aluminum nitride.

Table 1.1: Materials properties of AlN [28, 29]

PROPERTY	VALUE
Band gap	6.3eV
Density	3.3g/cm^3
Hardness	2.0 kg/mm
Theoretical thermal conductivity	320W/m·K
Thermal expansion coefficient	$5.3 \times \times 10^{-6}$/^{o}C (a axis);
Critical field strength Ec	6-20 MV/cm
Reflective index n	2.15
Surface acoustic wave velocity	5500-5650 m/s

From 1960's, much effort was done to grow and characterize the piezoelectric AlN materials. Over the years, several synthesis methods have been developed to grow AlN thin film on various substrates. The common thin film deposition techniques include purely physical methods, such as evaporation and purely chemical methods, such as gas and liquid phase chemical process. Furthermore, many overlapping processes that are based on glow discharges and reactive sputtering combine both physical and chemical methods.

The most popular techniques for epitaxial growth of III nitrides are based on metal-organic chemical vapor deposition (MOCVD), molecular beam epitaxy (MBE) and pulsed laser

deposition (PLD). It should be pointed out that MOCVD is also referred to as metal-organic vapor phase epitaxy (MOVPE) and organometallic chemical vapor deposition (OMCVD). MOCVD is one of the most important techniques for producing AlN thin films with high deposition rate, but the high working temperature (>700°C) requirement limits its applications in many areas such as the fabrication of electronic devices. Instead, low temperature techniques such as plasma assisted CVD, magnetron reactive sputtering, and ion beam deposition are also widely adopted.

As to sputtered film growth, conditions are more critical for AlN than for ZnO because of the possible presence of strong internal stresses. Results have shown that the growth of the thick AlN films is rather critical because of its tendency to present microcracking. This tendency is more evident with increasing the thickness of the film when using silicon substrate, particularly in the (100) orientation.

Some polycrystalline AlN films exhibit high quality piezoelectric properties and can be used for the transduction of both bulk and surface acoustic waves. If compared to other piezoelectric films, such as the well-known ZnO, AlN shows a slightly lower piezoelectric coupling.

In summary, PZT, ZnO and AlN possess their own advantages. Considering the piezoelectric coupling coefficient which determines the degree of energy transition between electrical and mechanical domain, PZT is definitely larger than the other two materials. A piezoelectric layer with too low coupling is difficult to be made to the RF filter with the required bandwidth. For dielectric constant, AlN and ZnO are similar with ε_r around 10. This value is much smaller than that of the PZT which have ε_r up to 400. From acoustic performance considerations a dielectric constant of 100 would be ideal at 1GHz. From the point of the acoustic wave velocity, the higher is the velocity, the higher is the BAW device resonance frequency. Therefore, AlN are better

than PZT and ZnO with respect to the high frequency range applications. As the piezoelectric layer determines the resonance frequency, its temperature coefficient is also affect the thermal drift of the resonator. AlN has a considerable lower temperature coefficient than ZnO. Several other material parameters have indirect effects on the performance of BAW resonators. A high thermal conductivity of the piezoelectric layer can enhance the power handling capability of a filter, and high chemical stability is also important to the reliability of the device in a humid environment. In these aspects, AlN shows excellent performance and it is the material employed to fabricate the BAW resonators in this study. Table 1.2 shows some material properties of the PZT, ZnO and AlN.

Table 1.2: Comparison of piezoelectric materials for BAW

	Aluminum Nitride (AlN)	Zinc Oxide (ZnO)	Lead Zirconate Titanate (PZT)
Coupling coefficient k_t^2 (%)	6.5	7.5	8-15
Dielectric constant ε_r	8.5-9.5	9.2	80-400
Longitudinal Acoustic velocity (m/s)	10500-11000	6350	4000-6000
Intrinsic loss	Very low	Low	High
CMOS compatible	Yes	No	No

1.8 MEMS FABRICATION BACKGROUND

Micromachining techniques have been used in the fabrication of the RF devices such as SAW and BAW resonators for a long time. The general process for fabricating a micro-scaled

mechanical structure out of silicon or other thin film materials involves three primary steps: deposition, patterning and etching.

1.8.1 Deposition

The first step, deposition, is that thin film materials are deposited or grown on the substrates which usually are the silicon wafers. Deposition processes range from simple spin-on methods, where a material in liquid form is deposited on wafer and the wafer is spun at high speeds to evenly spread a thin film of material across the substrate, to more complex physical and chemical methods that utilize complex chemical reactions and physical phenomena to deposit films. Two general methods exist for deposition of thin films: physical vapor deposition (PVD) and chemical vapor deposition (CVD). Each deposition method has intrinsic advantages and limitations in terms of the quality, type and range of material that can be deposited, as well as concerns related to equipment, cost and complexity.

Thin film deposition methods are classified by how the source material is introduced and by the activation of the source material. The processes that use heat (such as thermal evaporation), an energetic beam of electrons (such as electron beam evaporation), photons (such as pulsed laser deposition), or energetic ions (such as sputtering), are PVD methods. In contrast, CVD techniques use gases, evaporating liquids, or chemically gasified liquids as the source materials. One essential difference between PVD and CVD techniques is that the former deposit material which already exists in solid form, while the latter deposit material which does not exist previously and is synthesized in the vapor deposition process.

PVD uses physical ways to vaporize the target material. The produced vapor is later deposited as a thin film layer on the substrate. For different techniques, the employed vacuums

are different. For example, the thermal evaporation needs normally high (10^{-6} torr) to ultrahigh (10^{-9} torr) vacuum and sputtering needs moderate (10^{-4} torr) to low (10^{-1} torr) vacuum.

In this study, sputtering is the method we used to deposit the AlN thin film and the electrodes. Sputtering is also the PVD method most preferred in industrial fields. The objective of this deposition process is to controllably transfer atoms from a source (solid target) to a substrate where film formation and growth proceed atomistically. The target material can be almost any solid (alloys or compounds, both insulating and conducting) thus making the sputtering technique widely used. In this process, the gaseous plasma discharges are used to bombard the surface materials off of a target which is made of the material to be deposited. Atoms are then displaced (sputtered) and carried to the substrate by a potential difference between the target and the substrate (the target serves as the cathode, while the substrate wafer acts as the anode) [30]. The plasma is a partially ionized gas containing a great deal of energy. Heavy inert gases (usually argon ions) are used to provide the energetic ions which are discharged onto the target. This discharge results from a current flowing through the low-pressure gas (medium or high vacuum), and some of the discharges can glow due to light emission from excited atoms. The discharge particles can be either neutral or ionic. However, ions are preferred since thy can be controlled by an electric field. In the deposition process, more than one target can be used and deposition can be made at the same time on all targets, or in a predetermined order.

In the sputtering process, any material can be deposited stoichiometrically, and a uniform film deposition rate can be obtained over large areas. As well, the kinetic energy distribution of sputtered atoms is close to the energy needed for the displacement of surface atoms, therefore

there is no extra leftover energy, which could damage the deposited surface. Due to these properties, the sputtering is the most widespread using method of PVD techniques.

Sputtering can be divided into four categories: (1) direct current (DC), (2) radio frequency (RF), (3) magnetron, (4) reactive. There are important variants within each category (e.g., DC bias) and even hybrids between categories.

In DC sputtering a high voltage DC source (in the range of kilovolts) is used to create and sustain the plasma, with the sputtering target being the cathode of the discharge, and with the substrate (and vacuum chamber walls) acting as the anode. Argon is the most commonly used sputtering gas. DC sputtering requires the use of only conductive targets. This is due to the nature of the target cathode which accumulates charge, and would not allow for the flow of charge if it were non-conducting. In order to overcome this, Radio frequency voltage can be used to create a capacitive environment around a non-conducting target in order to create a discharge.

Radio frequency sputtering was invented as a means of depositing insulating thin films. Below about 50 kHz, ions are sufficiently mobile to establish a complete discharge at each electrode on each half-cycle. Direct current sputtering conditions essentially prevail at both electrodes, which alternately behave as cathodes and anodes. Above 50 kHz two important effects occur. Electrons oscillating in the glow region acquire enough energy to cause ionizing collisions, reducing the need for secondary electrons to sustain the discharge. Secondly, RF voltages can be coupled through any kind of impedance so that the electrodes need not be conductors. This makes it possible to sputter any material irrespective of its resistivity. Typical RF frequencies employed can range from 5 to 30 MHz. However, 13.56 MHz has been reserved for plasma processing by the Federal Communications Commission and is widely used. RF sputtering essentially works because the target self-biases to a negative potential. Once this

happens, it behaves like a DC target where positive ions bombardment sputters away atoms for subsequent deposition. Negative target bias is a consequence of the fact that electrons are considerably more mobile than ions and have little difficulty in following the periodic change in the electric field. [30]

Besides its ability to use non-conducting or electrically insulating targets, RF sputtering has many advantages over the DC sputtering such as the lower voltages and higher deposition rates. The magnetron RF discharges are the most widely used even though they can turn out to be more costly and may be noisy.

Though DC/RF sputtering is the most popular technique due to its simplicity, it is not efficient. And thin film might be damaged due to the increase in temperature which can be caused by the energetic electrons bombarding the surface of the substrate. Another technique magnetron sputtering will enhance the sputtering performance.

Electrons within the magnetic and electric field environment experience two forces which are well-known Lorentz force and electric field force,

$$F = \frac{m \cdot dv}{dt} = -q(\overline{E} + v \times \overline{B}) \tag{1.30}$$

where q, m, v, $\overline{E}$ and $\overline{B}$ are the electron charge, mass, velocity, electric field and magnetic field respectively.

First considering the case that the electric field is parallel to the magnetic field, an electron launched from the cathode with velocity v and angle θ with respect to $\overline{B}$ experiences a Lorentz force $qvB\sin\theta$ in a direction perpendicular to $\overline{B}$. The electron's orbit becomes a helical curve. Clearly, electron residence distance in the plasma will be prolonged by the magnetic fields and thus the probability of ion collisions will be enhanced. Therefore, applied magnetic fields have

the desirable effect of reducing electron bombardment of substrates, increasing the sputter deposition rates and extending the operating vacuum range.

If the electrons can be trapped near the target instead of reaching to the anode, the ionizing efficiency will be remarkably enhanced. This can be obtained by design the magnetron distribution in the sputtering process. Practically, it can be achieved by placing bar or horseshoe magnets behind the target. Therefore, the magnetic field lines first emanate normal to the target, then bend with a component parallel to the target surface and finally return, completing the magnetic circuit. Electrons emitted from the cathode are initially accelerated toward the anode, executing a helical motion in the process. When they encounter the region of the parallel magnetic field, they are bent in an orbit back to the target. Electrons stay in the negative glow region with a circular motion before collisions may drive them back toward anode. By suitable design of target magnets, a “race track” will be produced where the electrons hop around at high speed. Because of the intense ionized gas above the “race rack”, target erosion by sputtering occurs within it.

Magnetron DC/RF sputtering is presently the most widely commercially practiced sputtering method because of its advantages. When operating the planar magnetrons, the voltage is considerably lower than that without a magnet being used to trap electrons since a high voltage is not needed to maintain the plasma due to increased electron usage efficiency. It has very high deposition rates that are typically an order of magnitude higher than rates obtained by conventional sputtering techniques. Another advantage is that some substrate damage is prevented since electrons are safely trapped and cannot easily bombard the substrate surface.

Another form of sputtering is called reactive sputtering due to the fact that the sputtering ions (from the target) react chemically with the introduced gas and form the resulting deposited film.

The most common compounds reactive sputtered include oxides (e.g., Al_2O_3, SiO_2, In_2O_3), nitrides (e.g., AlN, TaN, Si_3N_4), carbides (e.g., TiC, WC, SiC), sulfides (e.g., CdS, CuS, ZnS) and oxycarbides and oxynitrides of Ti, Ta, Al and Si. Irrespective of which of the materials is considered, during reactive sputtering the resulting film is either a solid solution alloy of the target metal doped with the reactive element, a compound, or some mixture of the two. In this thesis, AlN thin films can be deposited on the substrates by sputtering the aluminum target in the plasma containing nitrogen and/or argon.

1.8.2 Patterning

After deposition, a pattern must be transfer to the films to serve as a template for the selective material removal. The most common method for transferring a pattern to a wafer is the photolithographic process. Photolithography involves three primary steps; deposition of a photosensitive emulsion layer (termed photoresist, or simply resist), ultraviolet exposure of the wafer and resist to some pattern, and subsequent develop of the wafer to remove unwanted photoresist and then get the exposed pattern. Photoresist is typically deposited on the wafer using the spin-on method. The pattern that used to expose the photoresist is termed the mask. During exposure process, the mask blocks the UV light from exposing that portion of the resist. The UV light then catalyzes a reaction in the unexposed portions of the resist. The photoresists is then developed in a developing solution. During the subsequent step, the developing solution removes those portions of the resist that were not protected by the mask. A resist of this nature is termed positive photoresist. A negative resist does the exact opposite: the exposed areas become less soluble in the developing solution and the protected areas are removed. Additional steps exist for annealing the photoresist, and preparation of the wafer (i.e. cleaning, drying, baking, etc.). The

defined photoresist then serves as a material mask for the removal of thin film materials. Fig. 1.12 shows the basic steps of the photolithographic process.

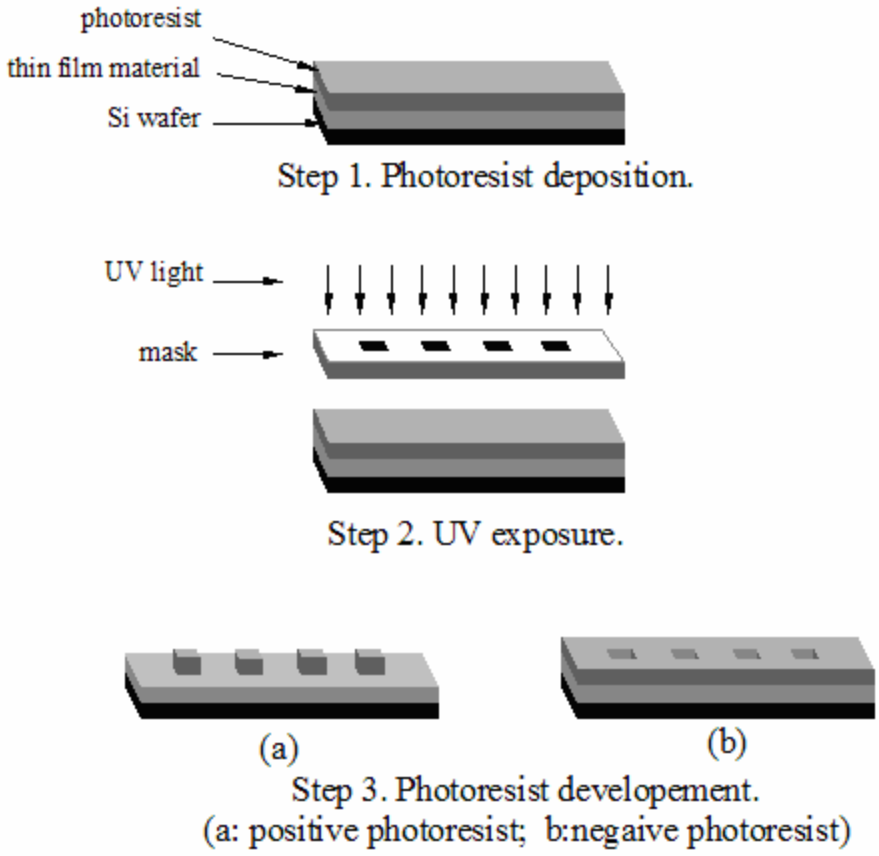

Figure 1.12: Basic photolithography process.

1.8.3 Etching

The final step involves the removal, or etching, of materials in desired areas by physical or chemical means to create the microstructure. The patterned photoresist serves as a material template for the definition of microstructures. Patterns can be etched directly into the silicon substrate, or into a thin film which in turn can be used as a mask for subsequent etches. Many

etching forms including wet-chemical, dry-chemical, and physical etching techniques are all used in MEMS processing.

Wet etching involves using solutions with diluted chemicals to dissolve the unprotected areas of a thin film or substrate. There are numerous wet etchants used, depending on the material to be removed. Wet etching can either be isotropic etching or anisotropic etching depending on the structure of the materials or the etchants used. For bulk micromachining, both isotropic and anisotropic etchants exist. If the material is amorphous or polycrystalline, wet etching is always isotropic etching. Each etchant removes material at a specific rate at a certain temperature, and thus the etch time varies as a function of material and thickness. The chemical reaction that occurs varies from etchant to etchant as well. Wet etching is easy to apply, and it needs inexpensive equipment and facility.

Dry chemical, or plasma, etching involves material removal by thin film reacting with a gaseous reactive species. A reactive species is generated by collisions of molecules in a reactive gas. These species are diffused to the solid target and absorbed at the surface, causing a reaction there. The reacted clusters are then desorbed and diffused away from the target. If the etching mechanism is purely chemical, powered by the spontaneous reaction, the process is referred to as "plasma etching". However, if the ion bombardment catalyzes an etch reaction, the process is referred to as reactive ion etching (RIE), which is really a combination of physical and dry chemical etching. RIE offers the advantages compared with wet etching, such as fast etch rates and good material selectivity to the films and resist temples, as well as the advantages inherent in physical etching, such as a high degree of anisotropy. Selectivity to the resist template is necessary because it can also be etched during these processes. RIE is very common in both IC and MEMS fabrication [31].

2.0 RESEARCH OBJECTIVES

The projective of this research is to develop the on-chip thin film bulk acoustic wave resonator (FBAR) that operates at GHz frequency range and the corresponding characterization methods and techniques.

Thin film bulk acoustic wave filters have been considered being the most promising RF filters for the RF and microwave signal processing and control applications. The FBARs are also considered being the most promising approach to fabricate the on-chip resonators. However, the fabrication of the high quality piezoelectric on-chip devices and their integration with other circuit elements remain a lot of challenge in the real industry processing. Processing challenges exist in direct deposition of AlM thin film and the integration of the thin film devices on the substrate. In addition, the fabrication and application the FBARs including multiple layer composite BAW resonators are lack of direct theoretical modeling, which makes the BAW filters remain a lot of technological challenges. Furthermore, since the resonance frequencies of the resonators may shift due to the processing uncertainty or the change of the application environments, the efficient resonance frequency control and tuning methods should be developed.

The growth of highly c-axis oriented AlN film on a suitable substrate becomes a key point to get a high quality BAW resonator with highly electromechanical performance. In this study, first, we will deposit the c-axis oriented AlN films on the Si substrate and sapphire substrate respectively by using the DC reactive magnetron sputtering method. The effect of the deposition

parameters including the discharge power, substrate temperature, deposition pressure, gas flow ratio, and the distance between target and substrate on the orientation of the thin film will be investigated. After the deposition of the AlN thin film, micro-fabrication techniques will be used to fabricate the four-layer membrane type FBAR and the composite resonators.

In order to obtain a device with the best performance quality, the theoretical modeling of the resonator need to be developed. Based on the Mason model and by using the transfer matrix method, the theoretical analysis for a multiplayer FBAR will be developed. The influence of the substrate and electrode on the resonance frequency and effective electromechanical coefficient will be studied. Also the resonance frequency control and tuning methods will be discussed according to the theoretical model.

Characterization of the piezoelectric films and the resonators is important for the design, fabrication and application of these acoustic devices. Thus, the elastic, piezoelectric and electromechanical properties of the AlN thin films and devices will be characterized. In addition, the resonance frequency characteristics of the device will also be characterized.

3.0 FABRICATION OF ALN THIN FILM BULK ACOUSTIC WAVE RESONATOR

3.1 FABRICATION OF ALN PIEZOELECTRIC THIN FILM

The properties of aluminum nitride (AlN) make it an interesting material for several applications in the microelectronics industry. Its wide band gap has led to investigations of its potential as an insulating material for GaAs and InP based electronic device structures. Its high hardness, high thermal conductivity, resistance to high temperature and caustic chemicals combined with a reasonable thermal match to Si and GaAs, also makes AlN an attractive material for electronic packaging applications. Its piezoelectric properties in the c-axis orientation and the high longitudinal acoustic wave velocity make it a suitable material to fabricate the bulk acoustic wave resonators.

AlN thin film resonator can be grown on various substrates such as silicon wafer, graphite substrate [32] and alumina wafer [33, 34]. Since AlN crystal material has the largest piezoelectric property at (002) crystal direction or c-axis direction, it becomes a key issue to deposited or grow AlN films with c-axis orientation which are strongly affected by the various types of substrates.

The c-axis oriented AlN thin film can be deposited on (111) silicon wafer [35] and the (100) silicon wafer [36, 37] directly. Using Si (111) as the substrate, The AlN thin films can be integrated with silicon based microelectronics. And we also can get the improved film quality over electrode-based deposition. This is because (002) growth of the AlN film is favored by 3-

fold symmetry. However, there is large lattice mismatch and large difference in coefficient of thermal expansion between the AlN film and the Si (111) substrate. The Si (100) direction is the more common wafer orientation for microelectronics. But unfortunately, the c-axis oriented growth on this direction is very difficult. Thus, we may require a seed or buffer layer such as aluminum wetting layer. There is also large lattice mismatch and large difference in coefficient of thermal expansion between the AlN film and the Si (100) substrate. The Pt (111) is an ideal buffer layer for the c-axis oriented AlN film growth. [38, 39] This is because the hexagonal AlN structure matches well with the Pt (111) plane. The AlN crystal grains grow quasi epitaxial on Pt (111) substrate.

Till now, the AlN film has been grown on the Si (100) by several method such as chemical vapor deposition [40, 41], and physical vapor deposition method [42, 43]. In my research, DC reactive magnetron sputtering method is used to grow the c-axis oriented AlN film on the Si (100) substrate while using the Pt (111) thin film as the buffer layer.

The AlN (002) are also been used as the buffer layer when depositing the GaN on the sapphire (002) substrate since AlN is lattice match with the sapphire substrate [44, 45]. In my research, the c-axis oriented AlN films are also deposited on the sapphire substrate (MTI Corporation, CA, USA) by using the DC magnetron reactive sputtering method. Pt/Ti has been used as the electrode between AlN and the substrate.

3.1.1 Process paramters in reactive sputtering

Reactive sputtering is a widely used PVD process where a metallic target is bombarded in a reactive atmosphere. For AlN thin film depostion, the high purity Al target is sputtered by the high energy particles in an Ar/N_2 ambient atmosphere. The sputterd Al atoms are deposited onto

the desired substrate where they react with N_2 gas molecules to form the AlN. Compared to sputtering from a compound target, the reactie sputtering have some important advantages: metal targets are cheaper and ealiy be machined; metal targets have the capability to bear (sustain) higher discharge power due to their high thermal conductivities which enable efficiently cooling the targets; one metal target can utilized to fabricate several different films within different reactive gas atmasphere. However, the reactive sputtering process is relatively complex and many process parameters will influence the film quaility including the purity, smoothness, inner thermal stress and prefered crystal orientation.

A) Depostion pressure

Pressure is an important parameter used in vacuum technology. A large number of units have been generated to describe it under various circumstances. In general, there are two types of units which including the scientific units system (or coherent unit system) and practical units system (or incoherent units system). For scientific units, the pressure is usually defined as a force per unit area, and examples of these units are newtons/meters^2 (or pascal) and dynes/cm^2. Practical units, however, are defined by the height of a column liquid such as Hg or H_2O, and examples of these units are Hg, torr, atmosphere, etc. Some important and frequently used units' conversions are:

1 atm=1.013×10^5 pascal (Pa)

1 torr=1 mmHg=133.3 Pa

1 bar=750 torr

The gas molecules's mean free path is associtate with the deposition pressure at constant process temperature. At low sputtering pressure, the mean free paths of the species increase owing to the decrease of the particle scattering which makes the particles in the plasma have

higher kinetic energy and thus they can easily transfer the energe to the adatoms at the the growing film surface. However, at low pressure, the bombardment of the growing film with fast neutrals which have sufficiently high energy will cause the re-sputtering [46, 47] and damage the growing film.

Normally, the magnitude of compressive stress increses with the decrease of the sputtering pressure. Since the internal stress accumlates within the AlN thin film by high momentum transfer at the surface at low pressure.

B) Ar/N_2 gas flow ratio

The addition of the inert gas Ar in the mixture gas atmaspher can offer several advantages. It can increase the sputtering yield and hence improve the deposition rate. It also provides an easy way to control the type and amount of both molecules and ions arriveing at the film surface. Thus, it can control the film stoichiometry and structure by varying the gas compositon.

While the gas pressure is kept constant, the mean free paths of the molucules don't change too much. Therefore, the effects of the flow ratio change are determined by the chemical natures of the gases. In addtion, The residul stress of the AlN film is also affected by Ar/N_2 flow ratio.

C) Discharge power

The discharge power is an important parameter for the reactive sputtering process. It can affect depostion of AlN film in a number of ways. The higher the dischge power is utlized, the higher the depostion rate can be obtained. For high deposition rate, the impurtity incorporated in the film from background gases can be dramatically reduced. On the other hand, low depositon rate results in poor film quality mainly due to background gas incorporation. However, extremely high depositon rate may result in nonstoichiometric films and the structural defects

due to the reaction and diffusion limitations. Discharge power can also affect the crystal orientaion of the AlN film by affecting the kinetic energies of the sputtering particals.

D) Substrate temperature

The deposition temperatuer may be the most effective process parameter for controling the crystal structrue of the sputtered film. High deposition temperature can improve the mobility of the sputtered atoms and ions. However, it also increases the cost of the process, introduces thermal stresses, increases imputity incorportion, etc. In practice, in order to integrate the film and resonator fabricaiton process with the Si based IC technologies, it is desirable to reduce the temperature as much as possible. Several methods such as utlizing the substrate bias need to be employed to reduce the depositon temperature.

3.1.2 Deposition of the AlN thin film and the electrodes

Since the c-axis oriented AlN thin film is difficult to be grown on the Si (100) substrate directly, the first step of the deposition of the c-axis oriented AlN thin film is to deposit the Pt/Ti thin film on the Si (100) wafer. Here, Ti thin film is used as the adhesive layer between Pt thin film and Si substrate. The thickness of the Ti should not exceed 20 nm that not only can bond the Pt and Si together but also doesn't affect the electromechancal properties of the resonator. The sputtering systems we used to deposit the Pt, Ti and AlN thin film are the ISE-OE-PVD-3000 (Innovative Systems Engineering Inc., PA, USA) and AJA ST20 (AJA international Inc., MA, USA) sputtering systems. The schematic drawing of the deposition chamber of sputtering machine is shown in Fig. 3.1. In the AlN film deposition process, the process atmosphere was the mixture of the Ar and N_2 where N_2 was used as the reactive gas which reacted with Al atoms or ions to form the AlN thin film on the substrate.

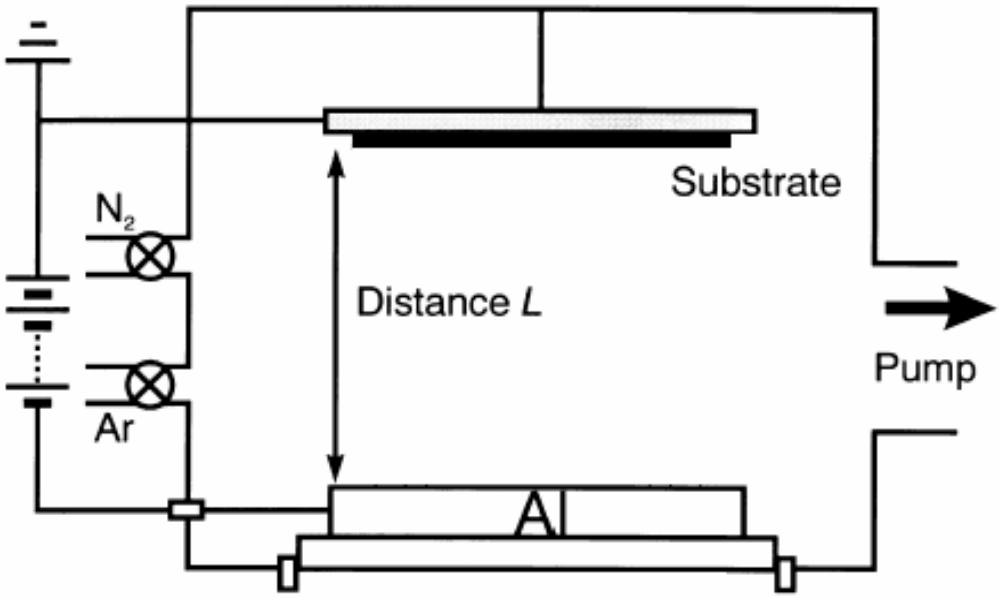

Figure 3.1: The schematic drawing of the DC reactive sputtering system.

Table 3.1: Sputtering conditions for preparation of the Pt and Ti thin films

	Pt	Ti
Target (99.999% purity)	ϕ50mm Pt target	ϕ50mm Ti target
DC Power (W)	100	100
Substrate temperature(^{o}C)	100-120	100-120
Target-Substrate distance(mm)	50-80	50-80
Base pressure (torr)	$<5\times10^{-6}$	$<5\times10^{-6}$
Sputtering pressure (mtorr)	5	5
Ar gas flow rate (SCCM)	10	10
N_2 gas flow rate (SCCM)	0	0

Table 3.2: Sputtering conditions for preparation of the AlN and Al thin films

	Al	AlN
Target (99.999% purity)	ϕ50mm Al target	ϕ50mm Al target
DC Power (W)	100	200-275
Substrate temperature (^{o}C)	20	450-550
Target-Substrate distance(mm)	40-80	40-90
Base pressure (torr)	$<5\times10^{-6}$	$<10^{-6}$
Sputtering pressure (mtorr)	5	2-5
Ar gas flow rate (SCCM)	10	5-10
N_2 gas flow rate (SCCM)	0	12-20

Different deposition conditions will lead to different material properties including the piezoelectric coefficient, mechanical properties and electric properties of the material. The deposition conditions for the electrodes and AlN thin film are shown in Table 3.1. and Table 3.2. The buffer layer Pt/Ti can be used as the bottom electrode of the bulk acoustic wave resonator. The Al thin film can be deposited on the top of the AlN thin film as the top electrode.

3.1.3 Structural analysis of the Pt and AlN film

X-ray Deffraction (XRD) is a powerful, non-destructive analytical method for examine the chemical composition and crystallographic structure properties of materials, such as crystal structure and orientation, lattice parameters, film texture, etc. This is achieved by using the method in various of modes. In this research, the θ-2θ mode was used to determine the film crystal orientation.

A crystal lattice is a regular three-dimensional distribution (cubic, rhombic, etc.) of atoms in space. These are arranged so that they form a series of parallel planes separated from one to another by a distance d, which varies according to the nature of the material. For any crystal, planes exist in a number of different orientations that each with its own specific d spacing. When a monochromatic X-ray beam with wavelength λ is projected onto a crystalline material at an angle θ, diffraction occurs only when the distance traveled by the rays reflected from successive planes differs by a complete number n of wavelengths. By varying the angle theta, the Bragg's Law conditions are satisfied by different d-spacings in polycrystalline materials. Plotting the angular positions and intensities of the resultant diffracted peaks of radiation produces a pattern, which is characteristic of the sample.

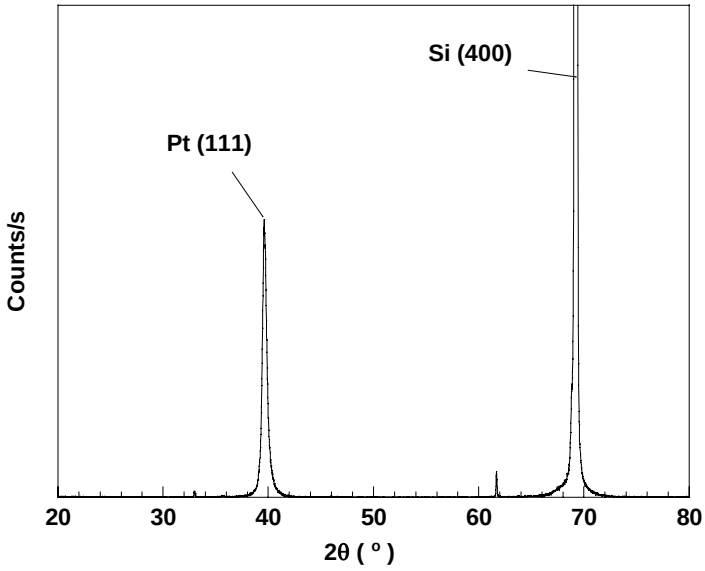

Figure 3.2: The XRD result of the Pt/Ti thin film deposited on the Si (100).

The orientations of the deposited Pt thin film were characterized by using the XRD analysis method. Fig. 3.2 shows the XRD result of the Pt/Ti thin film deposited on the Si substrate. It can

be seen that, the Pt film deposited at 100-120^{o}C shows good (111) orientation, which will advantage the growth of the c-axis oriented AlN thin film.

The detailed XRD analysis results of the AlN thin film deposited under various conditions will be discussed in the next chapter.

Scanning electron microscopy (SEM) is used to examine physical features with dimentions form several microns down to a few nanometers. A focused beam of electrons passsing through a vacuum is scanned and bombarded across the surface of the specimen and electrons emitted from the sample surface are used to form an image on a monitor screen. A range of emissions from the specimen occurs, including backscattered (or primary reflected) electrons, secondary electrons and X-rays, and all can be utilized to obtain topographical and elemental information. Because the amount of energy given to the secondary electrons of the sample as a result of the bombarded is small, only those secondary electrons that are produced within a very short distance to the surface are able to escape from the sample. Thus the secondary electrons topographical images have very high resolution down to several nanometers. Routinely, a detector close to the specimen surface collects secondary electrons. Each captured electron causes a flash of light in a scintillator, which passes down a light guide to a photomultiplier, and this converts it to an electrical signal. The final signal is proportional to the number of secondary electrons emitted from the specimen and is used to modulate the brightness of a display spot on the monitor screen. The orientation or morphogy of surface features influences the number of secondary electrons reach the detector, which creates variations in image contrast that represent the sample's surface topography. Thus, SEM is suitable for topographical and morphological analysis of AlN thin film.

The SEM can be used to identify the thickness of the electrode and the AlN thin film. It also can be used to observe the crystal orientation of the film. Fig. 3.3 shows the thickness of the Pt/Ti buffer layer is about 116nm. Since it is much thinner than the piezoelectric layer for the thin film bulk acoustic wave resonator, its effect on the resonance frequency and eletromechanical property of the resonator can be ignored when using it as the bottom electrode.

Fig. 3.4 shows the SEM images of the AlN thin film deposited on the center and edge position of the Pt/Ti/SiO_2/Si substrate respectively. The DC discharge power of the sputtering system was 250W and the deposition temperature was 450^{o}C. SEM images show that the AlN thin film has good thickness uniformity on the whole substrate. It can be seen that the thickness of the AlN thin film is about 2.6μm that leads to the resonance frequency of the thin film bulk acoustic wave resonator is about 2 GHz. By knowing the thickness of the films, we can identify the deposition rates for Pt and AlN film under the conditions described in the Tables 2.1 and 2.2 which are about 20nm/min and 4nm/min respectively.

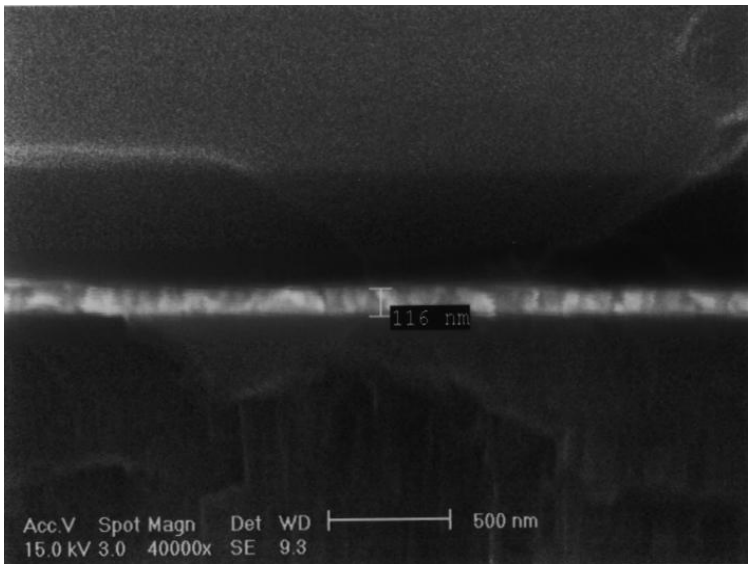

Figure 3.3: The SEM picture of the DC sputtering deposited Pt/Ti buffer layer.

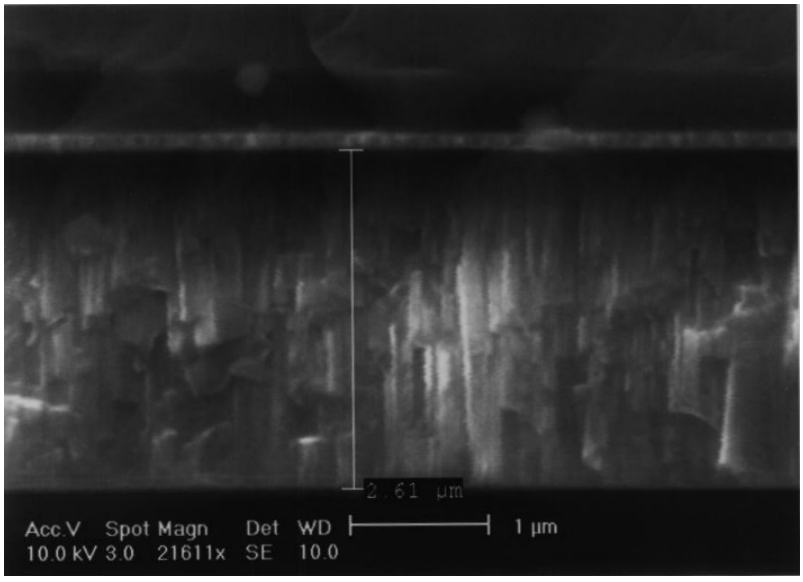

(a)

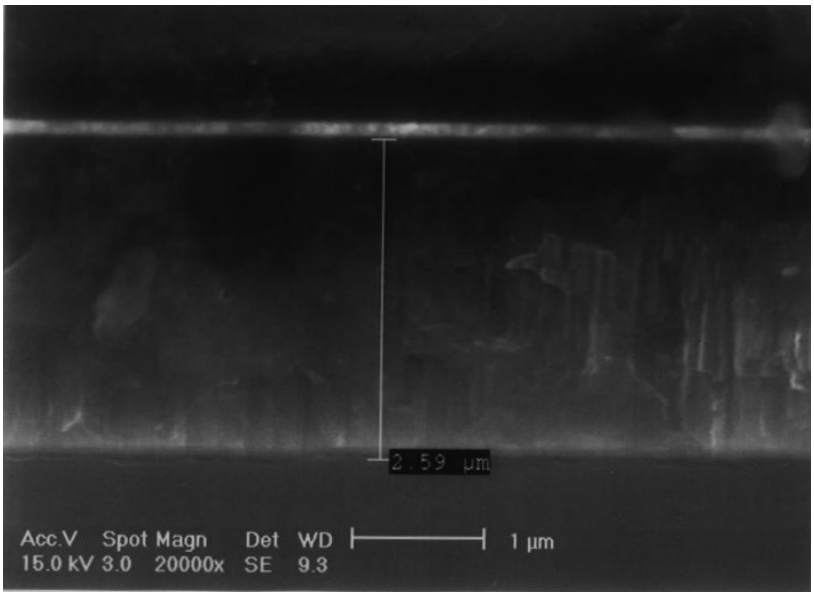

(b)

Figure 3.4: The SEM picture of the DC sputtering deposited AlN thin film at different position of the Si (100) wafer (a) center of the wafer, (b) edge of the wafer.

3.2 FABRICATION OF THE BULK ACOUSTIC WAVE RESONATOR

After the deposition of the AlN piezoelectric thin film and the top electrode Al, some material should be patterned and etched to fabricate the thin film bulk acoustic wave resonator and the thin film composite resonator. The schematic drawing of the thin film resonators is shown in Fig. 3.5.

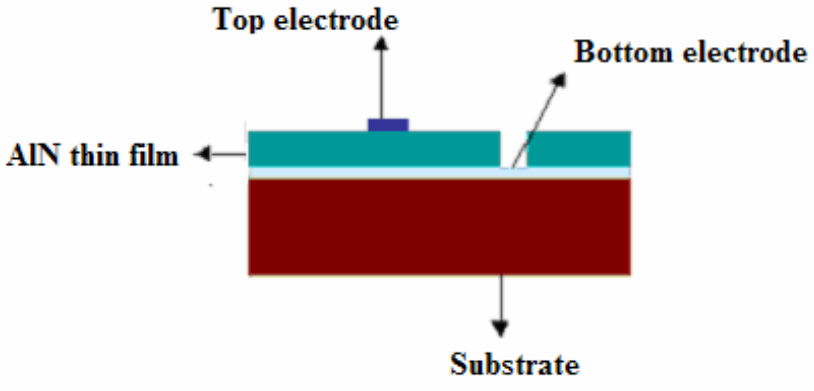

(a)

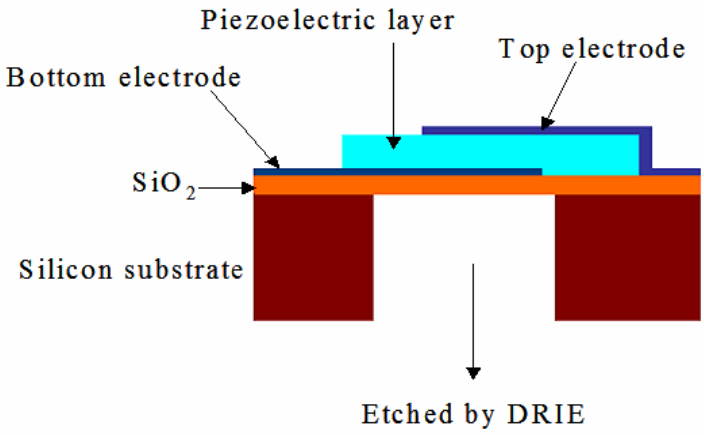

(b)

Figure 3.5: Schematic structures of the (a) four-layer composite resonator and (b) the thin film bulk acoustic wave resonator.

Fig. 3.5 (a) shows the four-layer thin film composite resonator. The substrate can be double side polished silicon or sapphire. The piezoelectric AlN thin film is sandwiched by two electrodes. In the fabrication process for this resonator, pattern and etching process were utilized for the AlN layer and top electrode layer. Fig. 3.5 (b) shows the structure of membrane type thin film bulk acoustic wave resonator in which SiO_2 layer was deposited on the Si substrate to act as a support layer. It can be seen that besides the pattern and etching of the AlN film and the electrodes, a backside etching was used to remove portion of the Si substrate to free the membrane. Thus the active zone of the FBAR includes four thin film layers which are etch-stop SiO_2 layer, bottom electrode, AlN, and top electrode.

Table 3.3: Typical etchants and etching rates for the AlN bulk acoustic wave resonator

Etched material	Etchant	Etching Rate	Temperature
Al	$HPO_4/HNO_3/CH_3COOH$/ DI water	30-50nm/min	Room temperature
AlN	H_3PO_4	40-50nm/min	~130 ^oC
SiO_2	Commercial BOE solution	100nm/min	Room temperature
Silicon substrate	KOH solution	80μm/hour	80-85^oC
	Deep RIE	80-100 μm/hour	Room temperature

The SU-8 and AZ series photoresists were used in the patterning for the thin film and as the mask of the etching processing. They were coated on the wafers or substrates by the Karl Suss RC8 spinner (SUSS MicroTec Inc., USA) in the clean room. After the photoresist being exposed by UV light and developed, the AlN film, electrodes and the silicon substrate were etched by

using the wet etching method and RIE dry etching method. There are a number of different types of etchants that can be used to etch different materials. Popular anisotropic etchants for silicon include potassium hygroxide (KOH) and ethylene-diamine and pyrocatecol (EDP). Experimental etching rates for the different materials with corresponding etchants and the working temperatures are given in Table 3.3.

In the process that the Si substrate is etched by KOH solution, the SiO_2 thin film commercially coated on the silicon wafer can be used as the mask material. However, even though wet etching is a slow process, SiO_2 mask itself can be attacked by the KOH if the system is left in the solution for a long time. In such case, using the silicon nitride or other particular thin film coated on the SiO_2 layer as the mask instead is effective way.

For substrates made of homogeneous and isotropic materials, the etchants will attack the material uniformly in all directions. This orientation-independent etching is referred to as isotropic etching. However, for the silicon wafer which has a diamond cubic crystal structure, different crystal planes have different abilities of resisting the etching of the etchant. Thus, it is possible to control the finished geometry of the etched silicon material when using some particular etchant. In silicon crystal, Due to the different alignment of the atoms, (100) and (111) planes have different mechanical strength which then reflects the degree of readiness for etching. It has demonstrated that the material on the (111) plane is hardest to etch. When the (100) silicon wafer is exposed to the etchant, the etching begins at the opening in the photoresist or the buffer layer over the silicon substrate. Considering the crystal structure of the silicon crystals, the angle between the (100) plane and (111) plane is 54.74°. Thus, the V-shape trench or inverted pyramid with the sidewall slope at 54.74° occurs as shown in Fig. 3.6.

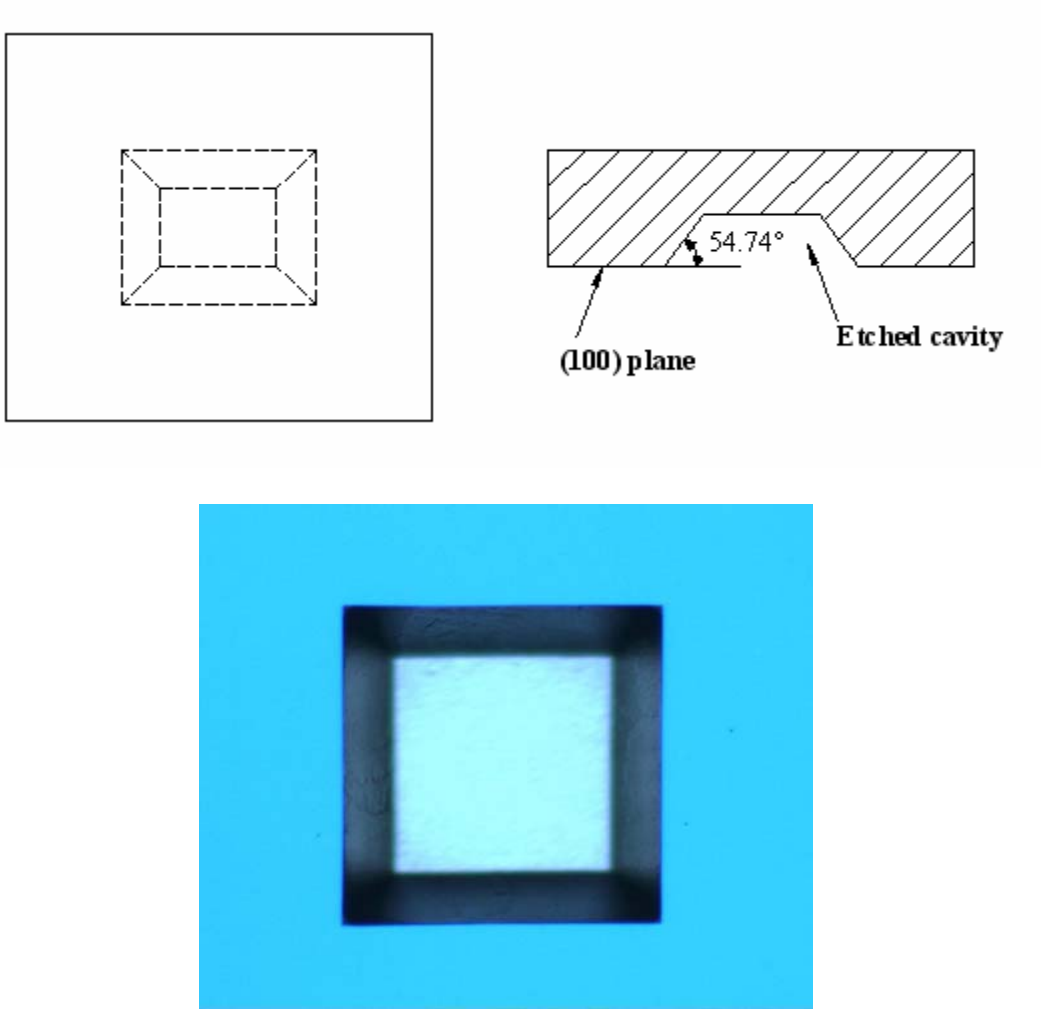

Figure 3.6: Anisotropic etching of silicon substrate.

For the membrane type FBAR fabrication, both sides of the wafer need to be etched. Thus, the protection of the top surface is important for the fabrication of the device when etch the back side of the silicon substrate. Photoresist cannot be utilized to protection layer since almost no photoresist can resist the etching of KOH solution for a long time. There are two ways to solve this problem. One way is to coat extra thin film such as Si_3N_4 or Pt which can resist the etching of the KOH for a much longer time. This method can introduce more fabrication cost and increase the complexity of the resonators structure. Another way is to use the mechanical fixture

to protect the other side. In the fixture, o-ring can be utilized to prevent the etchants from contacting the structures of the top surface. However, since the existence of mechanical stress exerted by the mechanical fixture and the inner stress of the thin film such as thermal stress, the wafer is easily damaged caused by the cracking during the etching process. Thus, Deep RIE dry etching becomes an ideal method to remove the silicon material without damaging the top pattern of the resonator.

During the AlN thin film dry etching process, etching process and passivation process are carried out alternatively. SF_6 and O_2 are the active gases which are used to etch the AlN away while the C_4F_8 is used to passivate the etching wall.

Figure 3.7 shows the images of the top surface and cross section of the fabricated membrane type thin film bulk acoustic wave resonator.

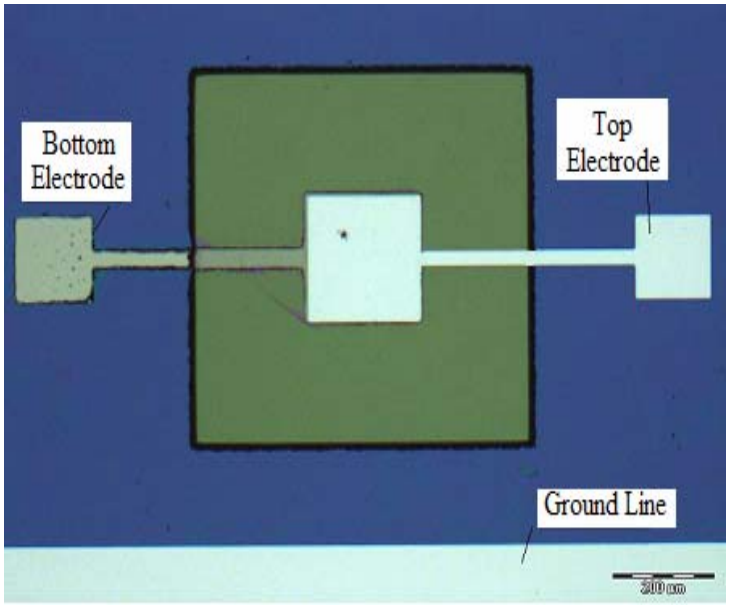

(a)

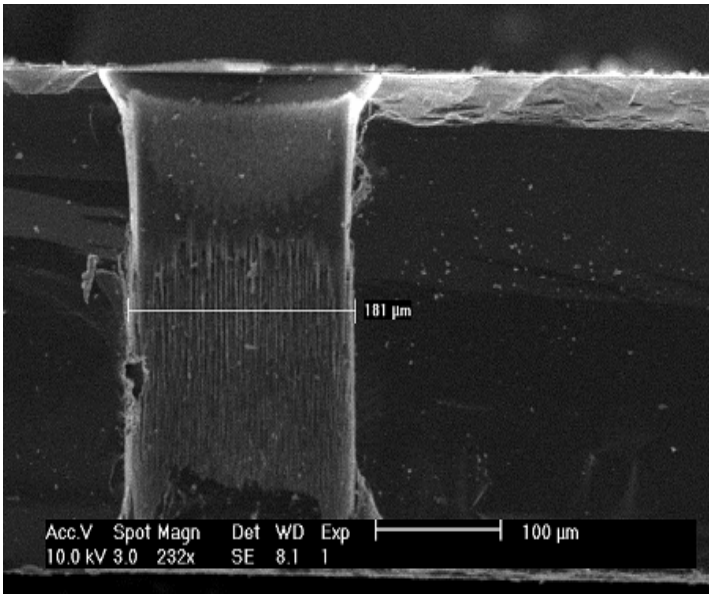

(b)

Figure 3.7: Images for the FBAR. (a) Top view image (b) SEM image of the cross section.

4.0 CHARACTERIZATIONS OF THE ALN THIN FILM

The material properties of the piezoelectric films are very important for the performance quality of the electromechanical devices made by these films. Thus, the characterization of the AlN thin film is critical for the fabrication of the thin film bulk acoustic wave resonator. In this chapter, the crystal structures, material morphologies, mechanical properties, and piezoelectric coefficient are measured or characterized by various scientific techniques.

4.1 CRYSTAL STRUCTURE OF ALN THIN FILM

In order to get the best performance properties of the BAW resonator, we need deposit the highly c-axis oriented AlN thin film. The crystal structure properties were characterized by the XRD and SEM methods.

AlN film has a hexagonal wurtzite structure with the lattice constant a=0.3110nm and c=0.4980nm. In this structure, each aluminum atom is surrounded by four nitrogen atoms, forming a tetrahedron with three equivalent Al-N bonds named B1 and a special Al-N bond named B2, which is parallel to the c-axis of the film. The bond length of B1 and B2 are 0.1885nm and 0.1917nm. In addition, the angle between two B1 is 110.5^{o}, and the angle between B1 and B2 is 107.7^{o}. Similarly, a nitrogen atom is surrounded by four aluminum atoms which also forms a tetrahedron in the crystal structure of the AlN thin film. In the AlN crystalline cell, the atoms of Al and N form sp^3 hybridized orbits. Bond B2 is formed by the coupling of the Al

empty orbit and the N full orbit. However, the B1 is formed by the coupling of the Al and N semi-full orbits. Therefore, the bond energy of B2 is smaller than that of B1 which makes B2 break relative more easily than B1, which means it needs more energy for the sputtered particles grown in the c-axis orientation. [35]

At the first stage of the deposition, nucleation grow randomly on a substrate, but only some nucleation survive whose fastest growth direction is closest to the normal direction of the substrate. The nucleation growth and therefore the final orientation of the thin film are affected by several sputtering parameters such as sputtering pressure, substrate temperature, discharge power, substrate-target distance and the gas flow ratio. First, we look at the effect of the sputtering pressure on the crystal orientation of the AlN thin film.

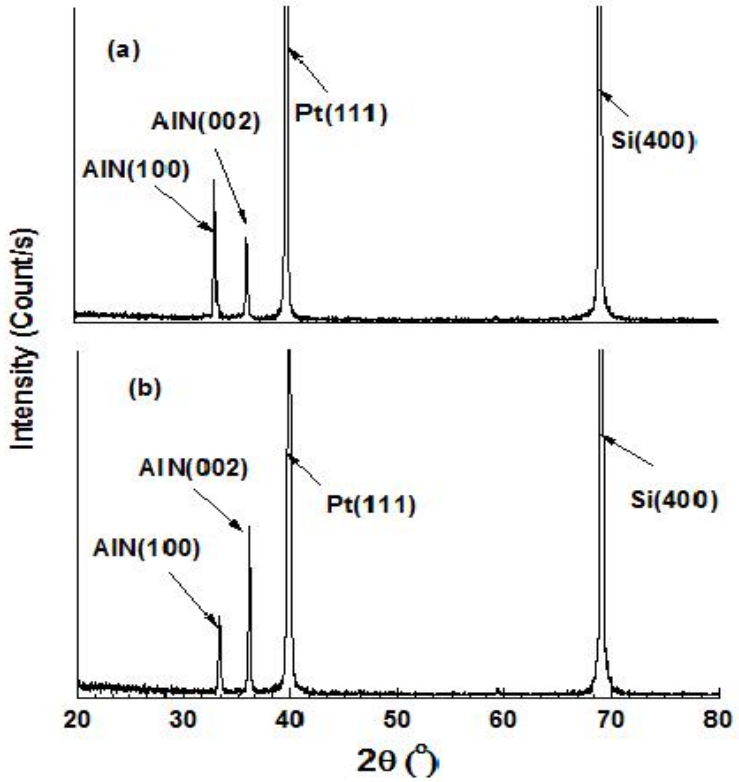

Figure 4.1: XRD results of the AlN thin film deposited with different deposition pressure: a) 4mtorr, (b) 2mtorr.

Fig. 4.1 shows the XRD results of the AlN thin film deposited on the Pt/Ti/ Si substrate with different deposition pressures while the other sputtering parameters kept constant. It shows that low sputtering pressure is of benefit to the formation of c-axis orientation of AlN film.

The sputtering pressure has profound effects on the preferred crystal orientation and microstructure of the sputtered films. Essentially, the sputtering pressure can affect the mean free path of the gas molecule of the plasma, thus it can influence the mechanism of the film deposition. The mean distance traveled by molecules between successive collisions, called the mean free path λ_{mfp}, is an important property of the gas that depends on the pressure. In the sputtering system, the mean free paths of the N_2 and Ar molecules are almost the same which has the following definition

$$\lambda_{mfp} = \frac{k_0 T}{\sqrt{2}\pi P d^2} \tag{4.1}$$

where k_0 is the Boltzmann constant, T is the temperature in ^{o}K, P is the pressure, and d is the elastic atom diameter. It can be seen that the mean free path of a gas molecular will increase with the decrease of the deposition pressure at constant temperature.

For air, at room temperature the mean free path is

$$\lambda_{mfp} = 5 \times 10^{-3} / P \tag{4.2}$$

with P in Torr and λ in cm. Therefore, when the pressure is 10^{-6} torr (or P=10^{-3}mtorr), λ_{mfp}=50m, which is much larger than the dimension of the deposition chamber of the sputtering machine. In this case, the molecules collide only with the walls of the deposition chamber.

For the film deposition by using the sputtering method, the deposition principle is the momentum transfer. While the sputtering pressure decreased, the kinetic energy of the plasma atom transferred to the target increases in direct proportion to the increase of the mean free path, which will improve the c-axis orientation of the AlN thin film.

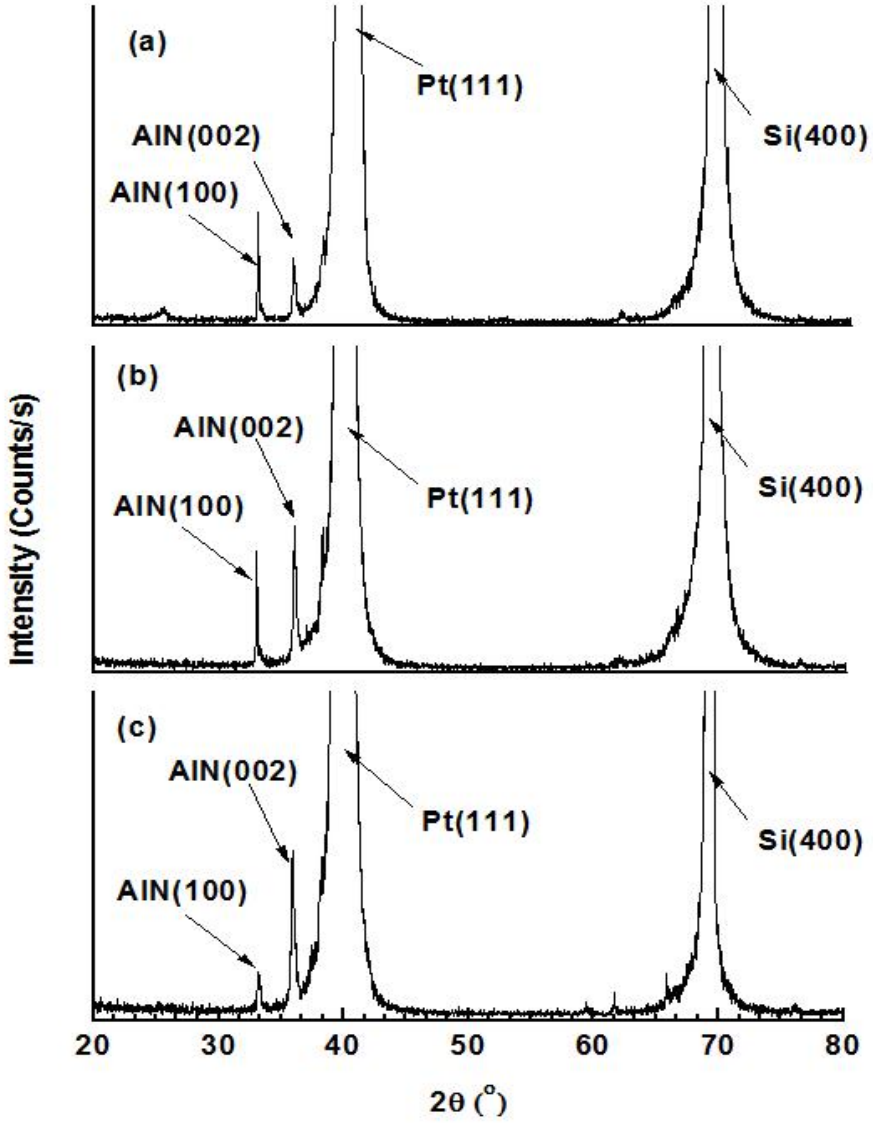

Figure 4.2: XRD results of the AlN thin film deposited with different distance between the substrate and target: (a) 90mm (b) 60mm (c) 40mm.

Fig. 4.2 shows the crystal structures of the AlN thin films deposited with different distances between the substrate and target while the other sputtering parameters kept constant. It can be seen that the reduction of distance can be helpful for the deposition of c-axis orientation AlN film. From the mean free path point of view, the distance between the target and substrate will affect the orientation of the film a lot. When the mean free path is larger than the distance, more

particles will reach the substrate without any collision. Thus, more particles with high energy will form the bond B2 which is beneficial to the deposition of c-axis orientation film. When the λ_{mfp} is smaller than the distance, most of the sputtering particles will reach the substrate after at least one time collision with other gas molecules which will decrease the energy of the sputtering particles. The AlN film grown under this condition will have (100) preferred orientation.

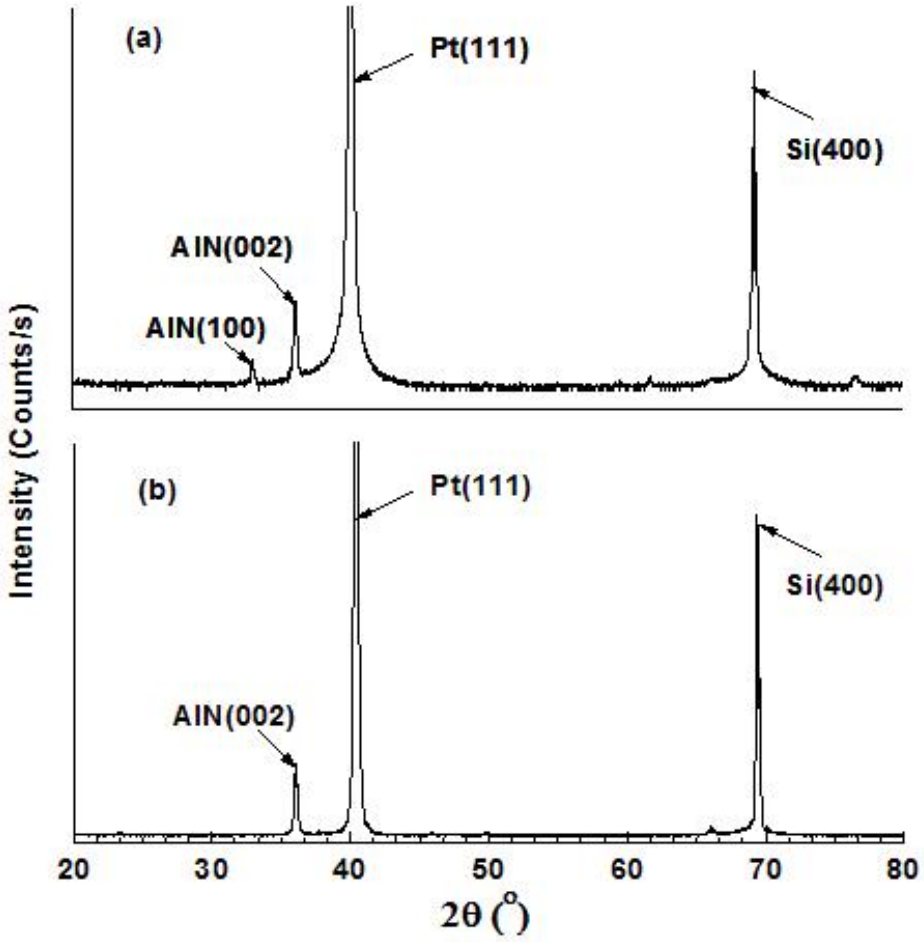

Figure 4.3: XRD results of the AlN thin film deposited at different substrate temperatures: (a) 450°C, (b) 550°C

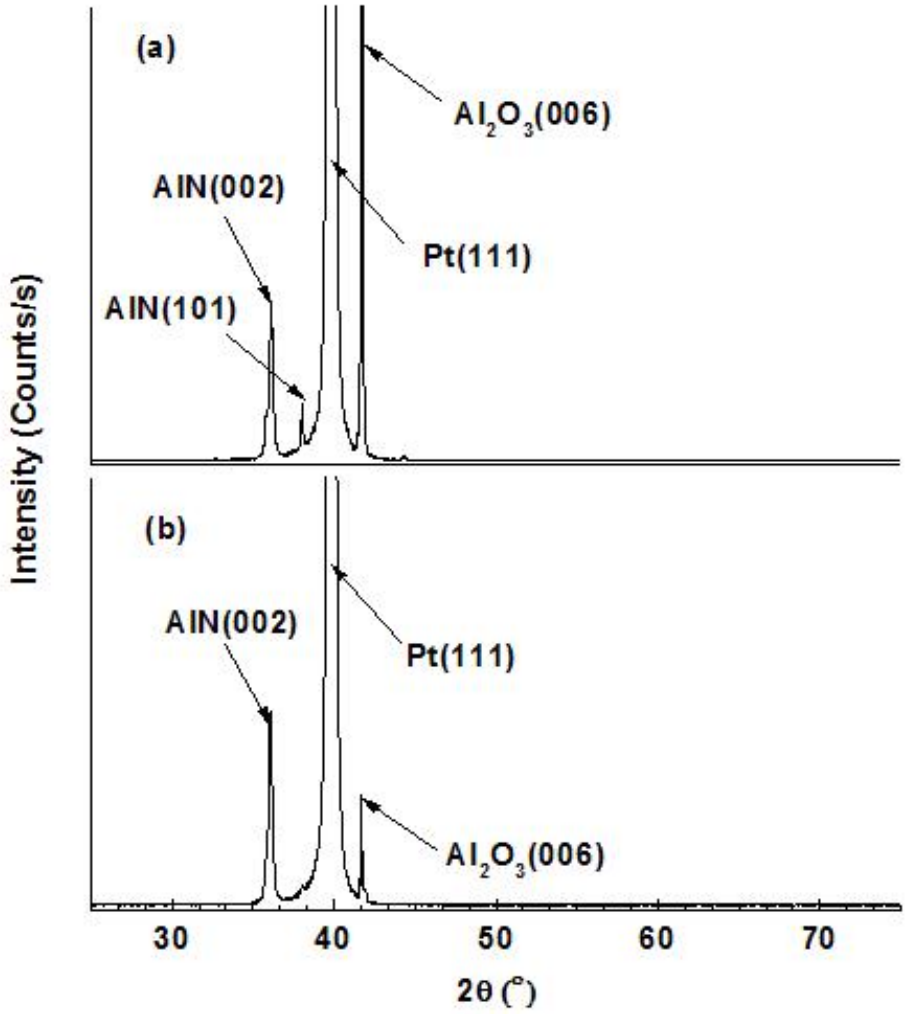

Figure 4.4: XRD results of the AlN thin film deposited with different discharge powers: (a) 200W, (b) 250W

Fig. 4.3 and Fig. 4.4 show the XRD results of the AlN thin films deposited with different temperatures and powers respectively, while the other sputtering parameters kept constant. The results show that the increase of the substrate temperature and the discharge power can dramatically improve the (002) orientation of the AlN thin film. This can be understood from the energy point of view. It is known that the basal plane in the crystal structure is the plane with lowest surface energy. Thus, the enhancement of the kinetic energy of the film atoms can change the microstructure and preferred orientation of the deposition film since the mobility of the atoms

is changed. While the kinetic energy is high enough, we can get the film with the specific preferred orientation. For the AlN thin film, the energy needed for the formation of (001) plane is larger than that for the (100) plane. Therefore, it can be seen that the fabrication of highly c-axis oriented AlN films at low high deposition temperature and discharge power owes to the energy enhancement of the atoms or ions.

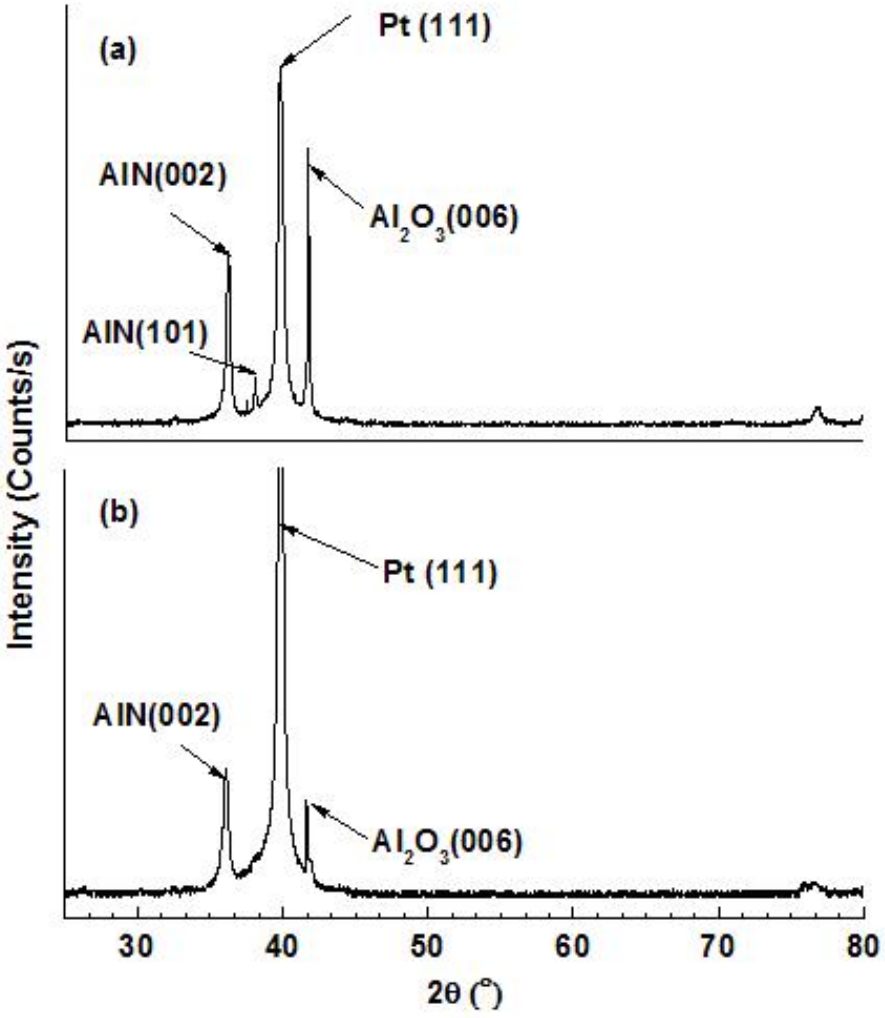

Figure 4.5: XRD results of the AlN thin film deposited with different gas flow ratios: (a) 80% N_2, (b) 60% N_2

Fig. 4.5 shows the crystal structure of the AlN thin film deposited at different gas flow ratios while other process parameters kept constant. For every particular sputtering system and deposition condition, the optimal N_2/Ar gas flow ratio for the c-axis orientation AlN film deposition is different. While in this case, 80% N_2 makes the N_2 in the mixed atmosphere over saturated, thus the AlN(101) peak appears in the XRD analysis results. Since N_2 and Ar molecules have approximately the same mean free path in the mixed gas, the effect of the variation of the flow ratio on the crystal orientation is largely depend on the chemical natures of these two gases.

The Scan Electron Microscopy (SEM) can be used to identify the thickness of the electrode and the AlN thin film. It also can be used to observe the crystal orientations of the films. Figs. 4.6-4.8 show the SEM images of the cross section of the AlN thin films deposited on the sapphire (001) and silicon (100) substrate. For the AlN films deposited at 550^{o}C, The SEM images reveal that the AlN films crystallized and the oriented grains are perpendicular to the surface of the substrates. However, for the AlN film deposited at 450^{o}C, the column crystal grains have a little angle with the normal direction of the silicon substrate. That means the film is not perfectly c-axis orientation deposited under this process condition. XRD result shows that AlN (100) orientation also exists. The SEM results demonstrate that the substrate temperature has a profound effect on the orientation of the deposited thin film.

All the XRD and SEM analysis results demonstrate that we have deposited the highly c-axis oriented piezoelectric AlN thin films on the sapphire (001) and silicon (100) substrate successfully. The deposition parameters have efficient effects on the crystal structures of the films.

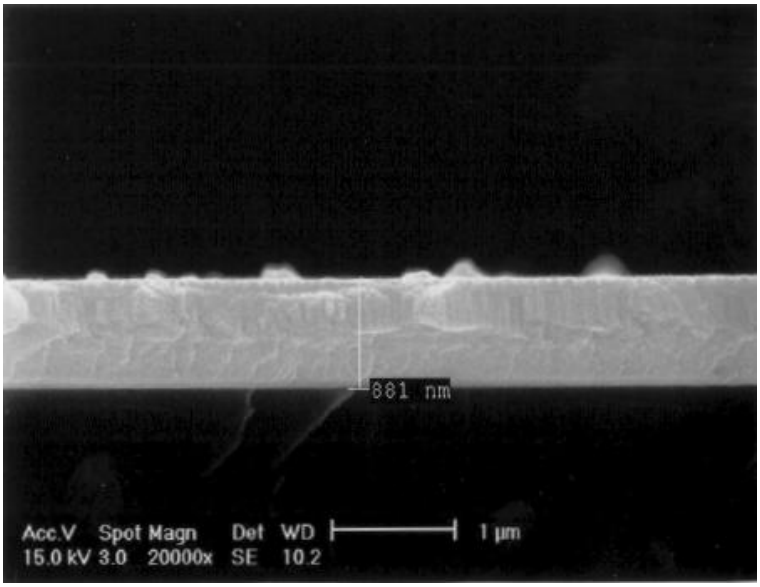

Figure 4.6: SEM image of AlN film deposited at 550^{o}C on sapphire (001) substrate.

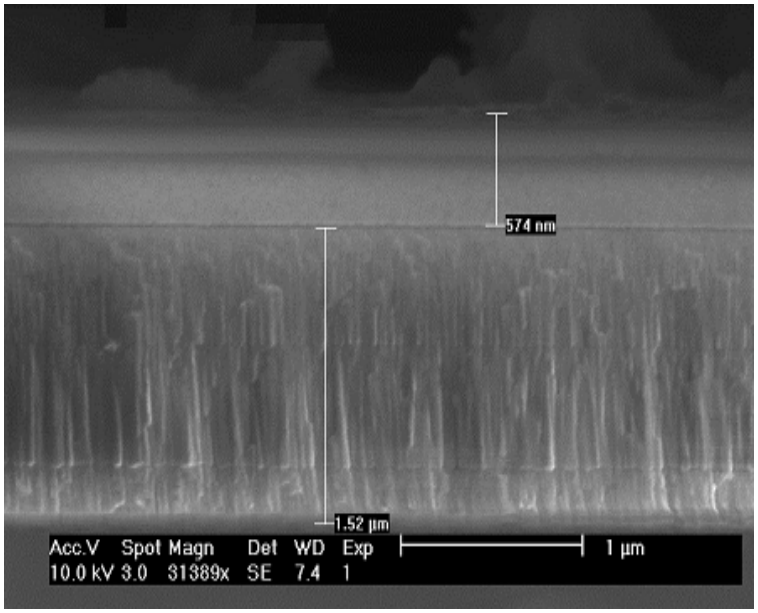

Figure 4.7: SEM image of AlN film deposited at 550^{o}C on silicon (100) substrate.

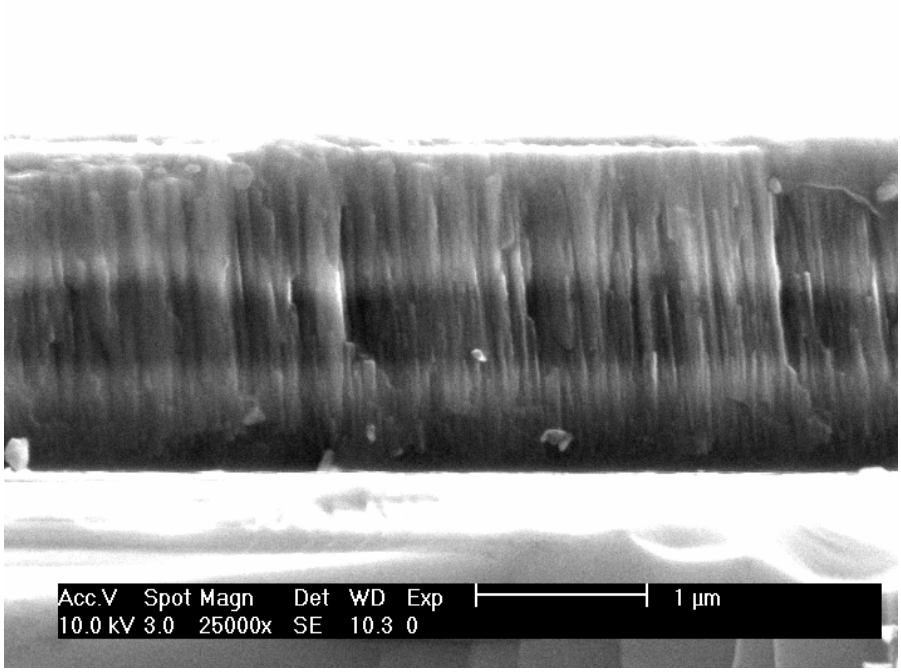

Figure 4.8: SEM image of AlN film deposited at 450^{o}C on silicon (100) substrate.

4.2 SURFACE MORPHOLOGY OF ALN THIN FILM

The thin film surface morphology is critical for the fabrication and design of the acoustic devices. We used SEM and Atomic force microscopy (AFM) to observe the surface morphology of the AlN thin films.

Fig. 4.9 is the SEM images which present the morphology of the AlN thin films prepared at 550^{o}C. The sputtering pressure and discharge power are 2mtorr and 250W respectively. It, clearly, demonstrates that the film is smooth, uncracked, dense, low contaminated and with a good uniformity.

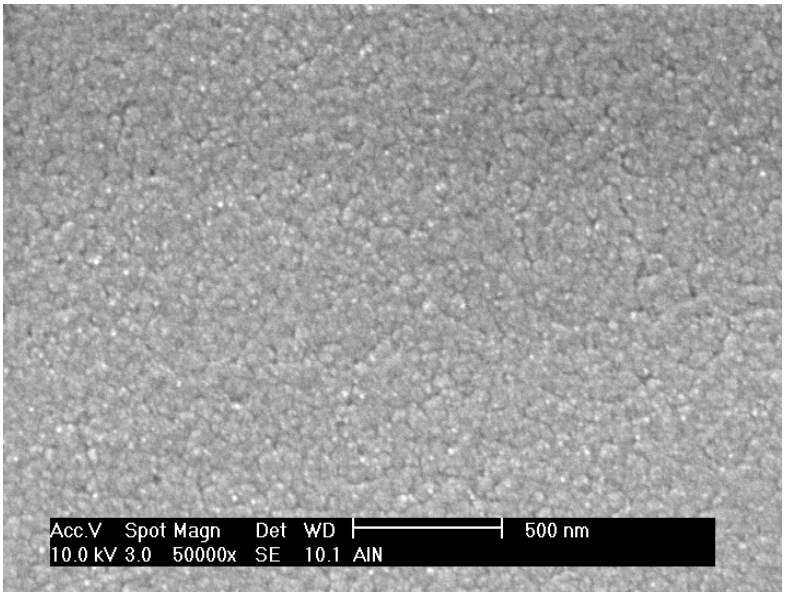

Figure 4.9: Surface morphology of the AlN thin film.

Surface roughness is an important parameter which can affect efficiently some of the performance properties of the resonators. For the piezoelectric thin film applied to the surface acoustic wave device, the roughness becomes a critical factor for the quality of the device. As for the SAW device, the acoustic waves travel along the surface of the piezoelectric layer in lateral direction and the acoustic energy is restricted in the film surface within a wavelength distance from the surface to the inside. When the surface roughness is more than a wavelength, the surface acoustic wave will not pass through. It has been reported that the surface roughness of the film is required to be less than 30 nm for the SAW device [35].

AFM was utilized to characterize the surface roughness of the AlN thin film. The AFM probe scans the surface of the film with a sharp tip, a couple of microns long and often less than 10nm in diameter. The tip is mounted on a flexible cantilever with 100 to 200μm length. Forces between the tip and the sample surface cause the cantilever to bend or deform and the laser beam coupled with the cantilever is reflected and detected by photodetector. Finally the laser beam

signal change can be converted into height variation of the sample surface and thus the morphology of the film can be obtained.

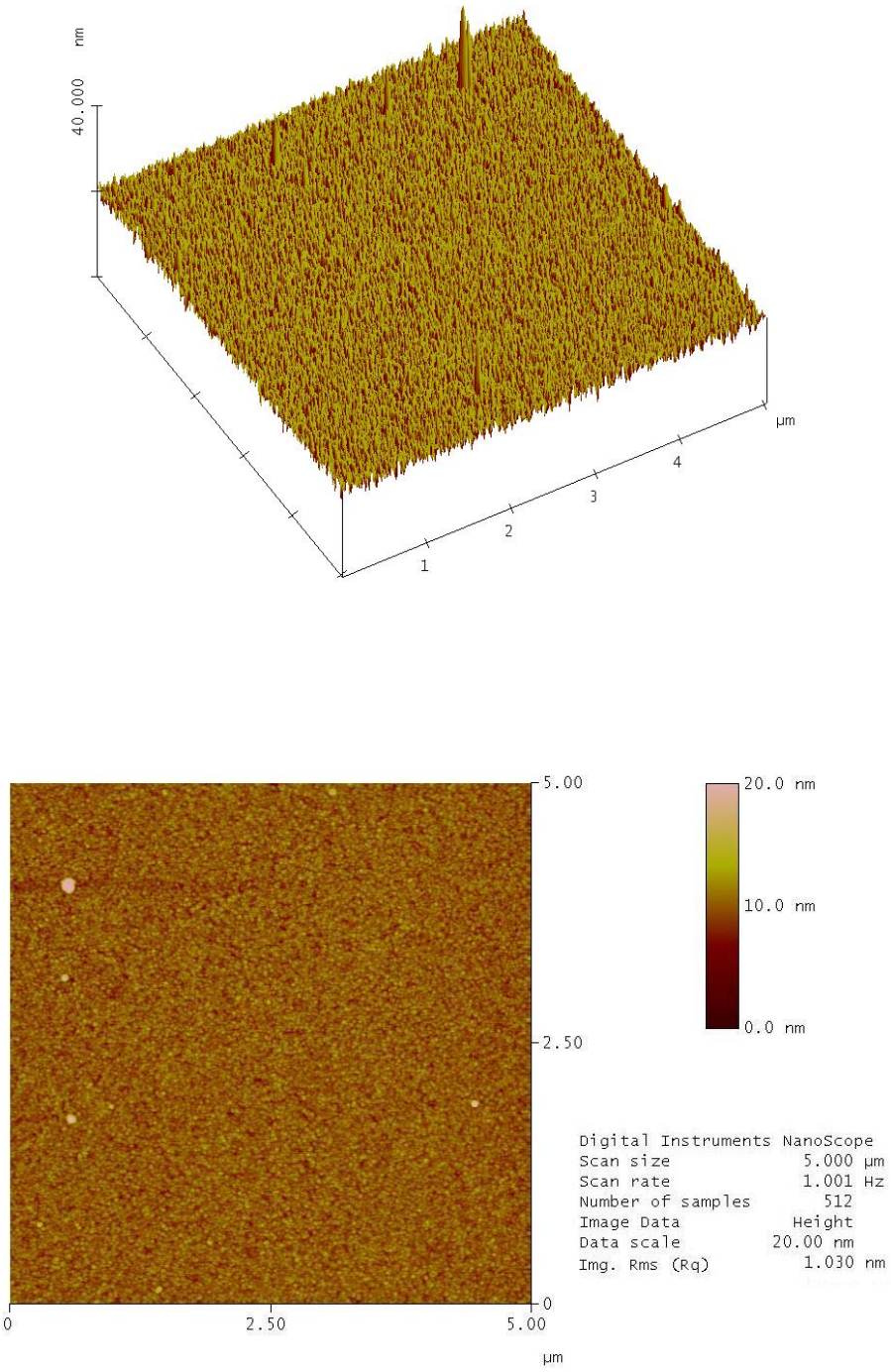

Figure 4.10: The AFM images of the AlN thin film deposited on Pt/Ti/sapphire at 2mtorr.

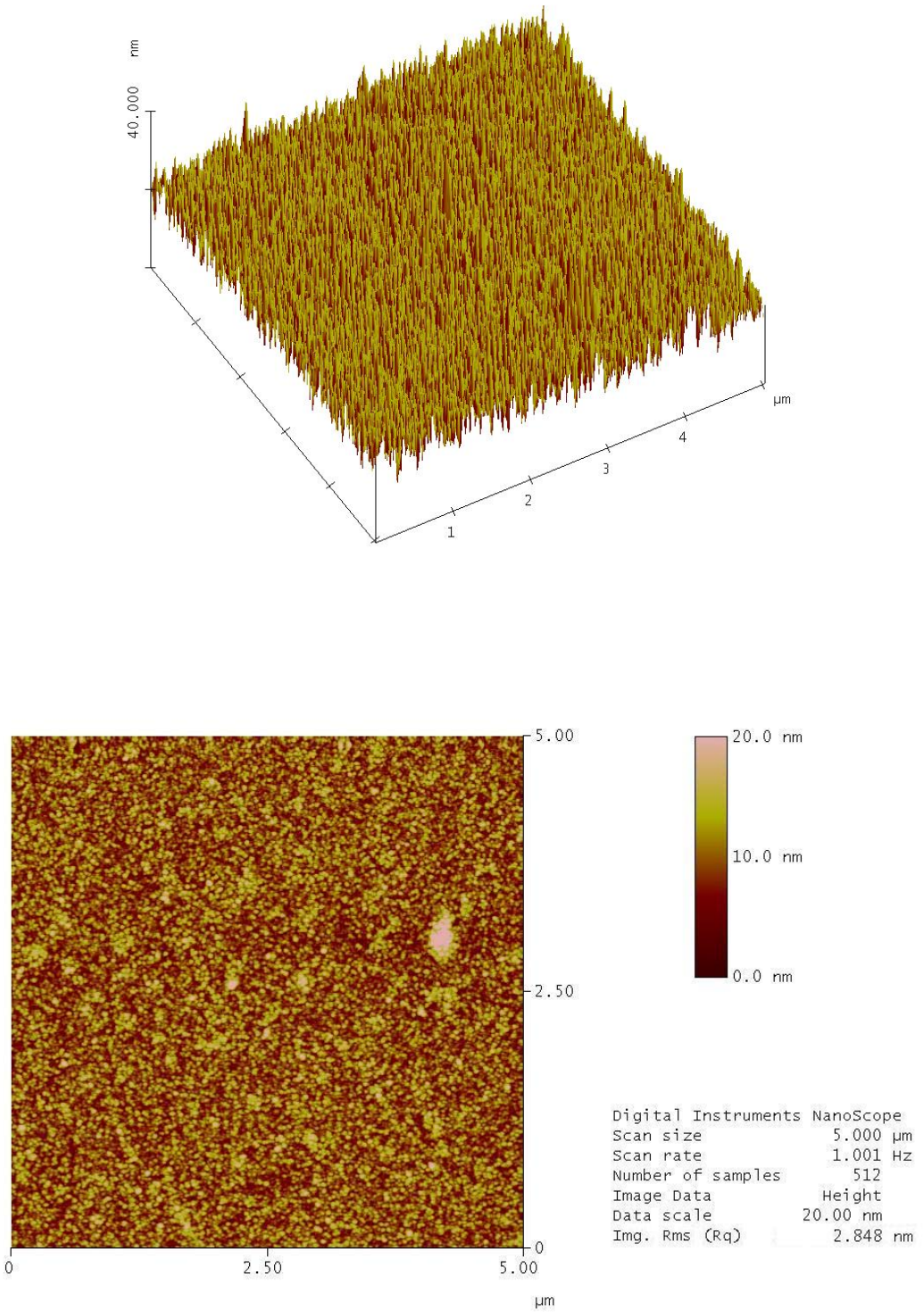

Figure 4.11: The AFM images of the AlN thin film deposited on Pt/Ti/sapphire at 4mtorr.

Fig. 4.10 and Fig. 4.11 show the statistical analysis of the surface roughness of AlN films deposited on Pt/Ti/sapphire substrate. For comparison purpose, only the sputtering pressures were changed for the deposition conditions. Both samples were deposited at 550^{o}C with 275W DC power and the N_2 concentration is 60%. The roughness was measured at a root-mean square (RMS) value. For the film deposited at 2mtorr, the roughness is 1.030nm which is much less than 2.848 nm which is the roughness of the AlN film deposited at 4mtorr. The results show that the reduction of sputtering pressure not only is in favor of the growth of c-axis orientation but also can improve the surface roughness of the AlN thin film. The results also indicate that the AlN films are uniform with smooth morphologies that will improve the coupling factor when these films are utilized in FBAR devises.

4.3 MECHANICAL PROPERTIES OF THE ALN THIN FILM

In past a few decades, with the advance of the nano- and micro-scaled science, engineering and technology, the micro- and nano-indentation methods were emerged as strong techniques to measure the mechanical properties of the thin films. The principle of these methods is to get the penetration depth (h) of the diamond tip which contacts with the specimens under the controlled load (P). The recorded results will be simulated by corresponding mechanical model to obtain the material properties.

It is well known that the elastic and plastic deformations are both in existence during the tip penetration process. The unloading portion is usually considered pure elastic rebound of the material. Therefore, the unloading process results only depend on the material elastic properties of the thin films.

In order to characterize the mechanical properties of the thin film, fixed probe nanoindentation method was employed. Comparing with other indentation methods, fixed probe nanoindentation has a few advantages. First, since there is a tilting angle for cantilever indenter, the indentation made by this indenter is not totally perpendicular to the sample surface. However, the probe for the fixed probe nanoindenter is normal to the sample surface. Second, the maximum load for a fixed nanoindentor can be up to 10mN that is much larger than the AFM cantilever indenter's maximum load which is normally below 100μN.

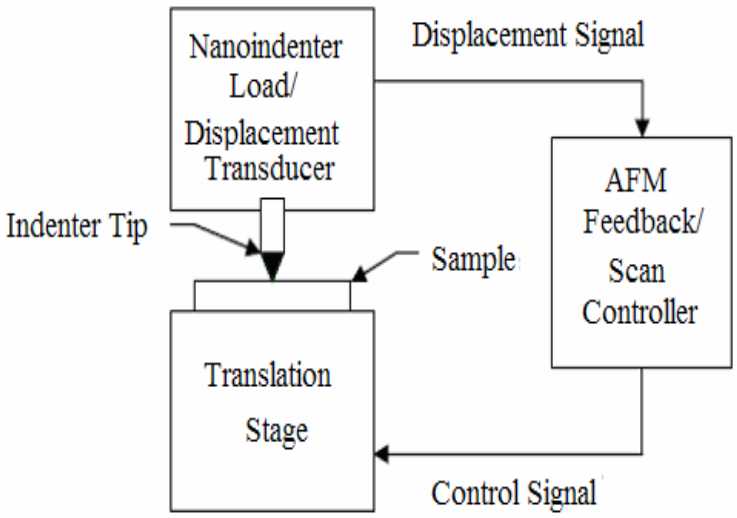

Figure 4.12: Schematic of a fixed probe nanoindenter with in-situ imaging capability.

The nanoidentation tests were performed in a Hysitron TriboScope (Minneapolis, MN, USA) attached to a Quesant (Agoura Hills, CA, USA) atomic force microscope (AFM). Fig. 4.12 is schematic drawing of the working principle for hysitron nanoindenter. The hyriton transducer can serve the function of sensing the sample surface and providing the topographic feedback for imaging. The in-situ imaging capability allows the indenter probe to be positioned to any desired

material feature within ten-nanometers. In the tests, A Berkovich diamond indentor with a nominal tip radius of 40 nm iss used.

In the nanoindentation test, an indentor tip with a known geometry is driven into a specific surface site of the thin film by applying an increased normal load. When reaching a preset maximum value, the normal load is reduced until partial or complete relaxation. This procedure can be performed repetitively. At each stage of the experiment the position of the indenter relative to the sample surface is precisely monitored by the transducer and feedback to the controller.

For each loading/unloading cycle, the applied load value is plotted with respect to the corresponding position of the indenter. Then the resulting load-displacement curves can be obtained which provide data specific to the mechanical nature of the material under examination. Established models are used to calculate quantitative hardness and modulus values from the data.

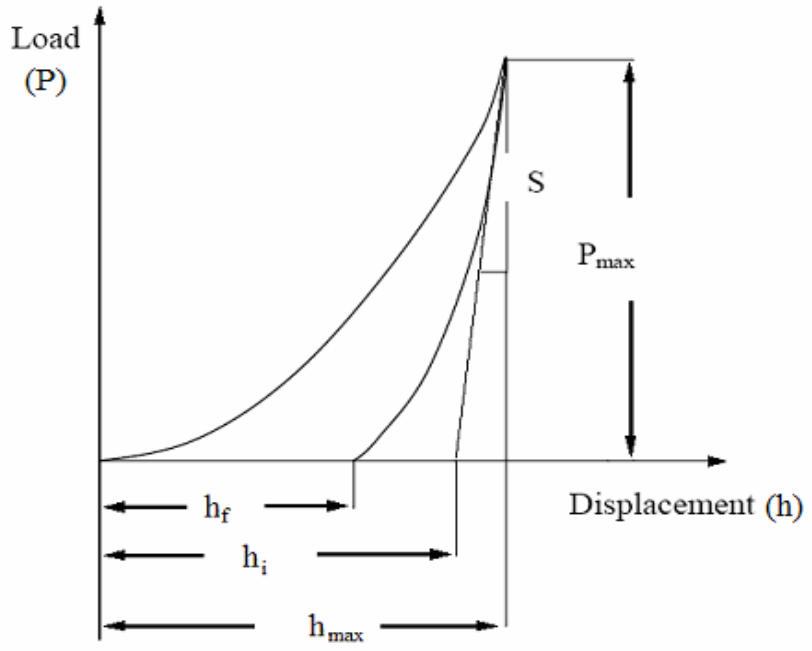

Figure 4.13: Indentation load-displacement curve.

Fig. 4.13 is the schematic drawing of the load-displacement curve which can be experimentally obtained by the indentation test. Where h_{max} is the maximum displacement which corresponding to the maximum applied loading $P_{max,}$ h_f is the final penetration depth after the unload process. The experimental stiffness S is the slope of the tangent line to the unloading curve at the maximum loading point (h_{max}, P_{max}).

The tested samples were the three-layer composite resonators with different thin piezoelectric film thickness, which were 0.6μm, 1.2μm and 1.5μm respectively. The discharge power and substrate temperature were 250W and 550^{o}C respectively and the substrate was sapphire. In the tests, the maximum loads were varied from 1000μN to 4000μN. The results of the loads and displacements during the test offer us a lot of information including the reduced elastic modulus and hardness.

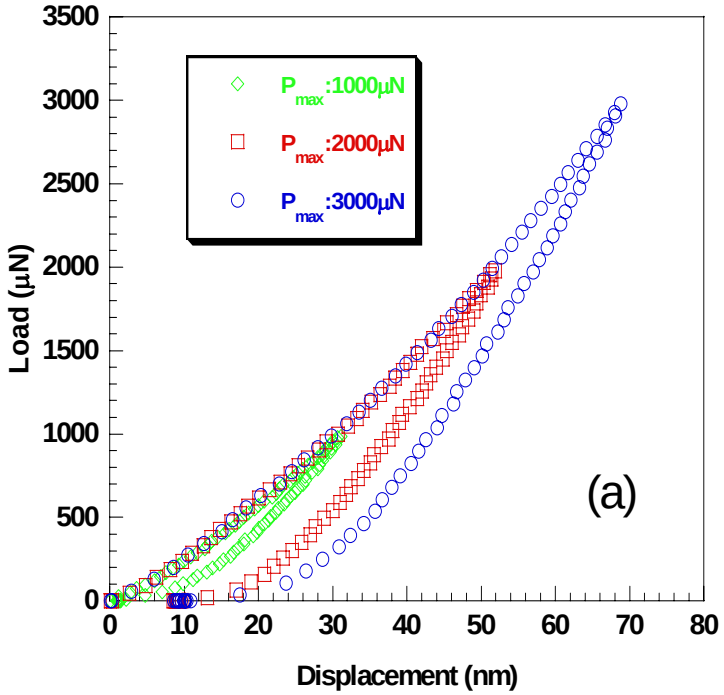

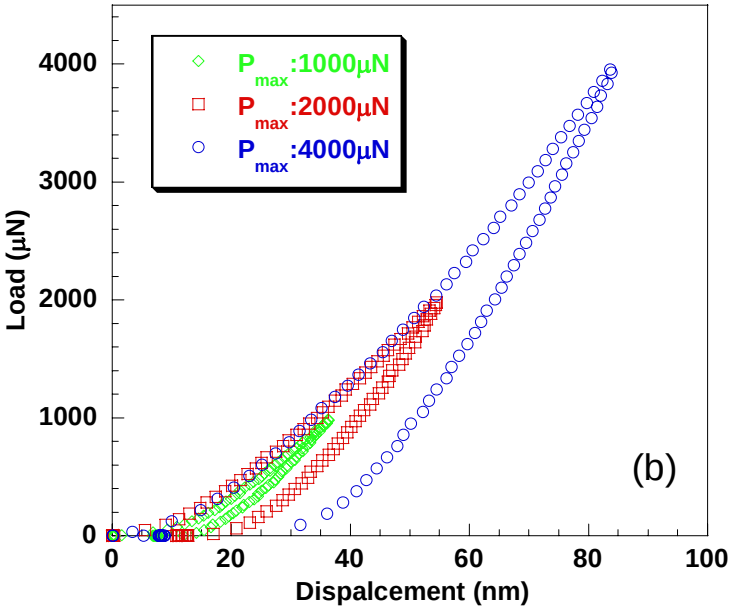

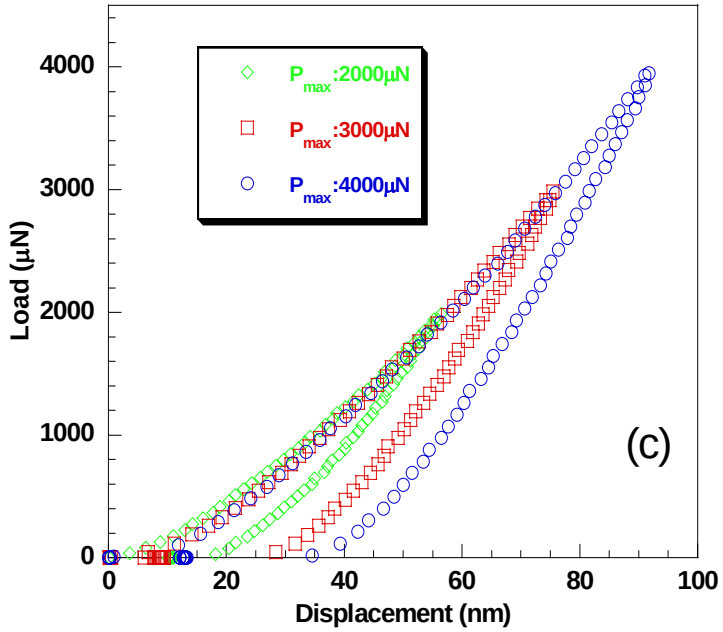

Figure 4.14: Load-displacement curves of the nanoindentation on the AlN thin film with different maximum loads at room temperature: (a) 0.6 μm, (b) 1.2 μm, (c) 1.5 μm.

After the nanoindentation tests, the load displacement curves were obtained for these three different samples. Fig. 4.14 (a), (b) and (c) show the nanoindentation load-displacement curves

of the AlN thin film with thickness 0.6μm, 1.2μm and 1.5μm respectively. It can be seen that with the increase of the maximum load P_{max}, the h_{max} and h_f increase too. All the load-displacement curves are smooth and regular without discontinuities, which indicates there are no cracking occurred in the penetration process.

From the load-displacement curves for various applied maximum loads, the reduced elastic modulus Er and hardness H can be obtained. Hardness is a material property indicates the material resistance to the elastic and plastic deformation. A lot of methods have been used to characterize the hardness of the material over a wide range of size scales. For nanoindentation, while the indentation depth is not deep enough, the effect of the substrate can be ignored. The hardness is normally defined as the maximum load divided by the projected area of the indenter which is in contact with the sample at maximum load. That is

$$H = \frac{P_{\max}}{A_C} \tag{4.3}$$

where H, P_{max} and A_C are the hardness, maximum applied load and the projected contact area of the indenter at the maximum load condition, respectively.

The reduced elastic modulus can also be determined from the unloading portion of the load-displacement curve by the following equation [48, 49]:

$$E_r = \frac{\sqrt{\pi}}{2}\frac{dP}{dh}\frac{1}{\sqrt{A_C}} \tag{4.4}$$

where E_r and dP/dh are reduced elastic modulus and experimentally measured stiffness S which was illustrated in Fig. 4.13, respectively.

Fig. 4.15 shows the reduced modulus E_r and hardness of the thin AlN films. It can be seen that the average reduced moduli of the thin films with different thickness do not change too

much with the values of about 250 GPa. The average hardness of the AlN thin films is about 18 GPa.

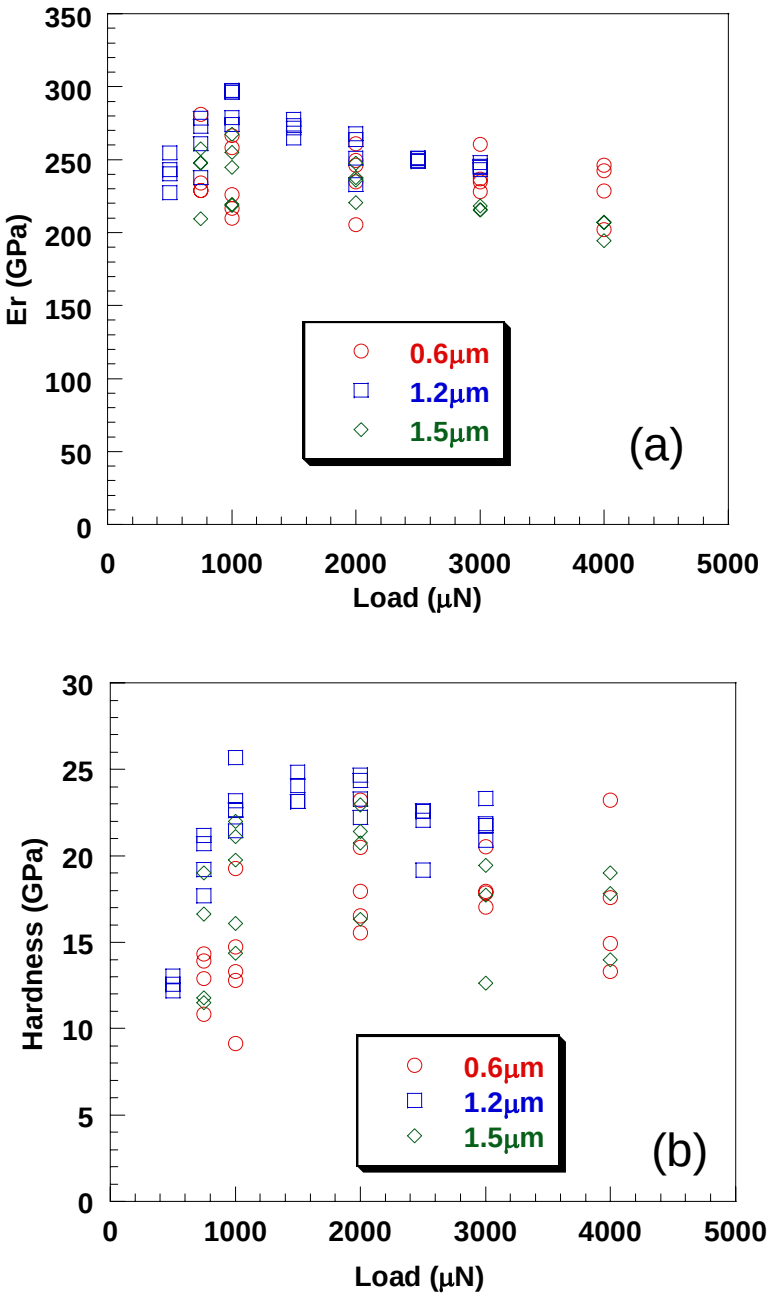

Figure 4.15: (a) Reduced elastic modulus and (b) hardness of the AlN thin films with different maximum loads at room temperature.

The reduced elastic modulus reflects the material properties of the AlN thin film under the effect of the diamond tip. Furthermore, we can also calculate the truly elastic modulus of the AlN thin film by the following equation [50]

$$\frac{1}{E_r} = \frac{1-v_s^2}{E_s} + \frac{1-v_i^2}{E_i} \tag{4.5}$$

where E_s and E_i are the elastic modulus of the thin film and the indenter respectively, and v_s and v_i are the Poisson ratios of the film and the indenter respectively. For the diamond tip, E_i is 1141Gpa and v_i is 0.07. Substituting the Poisson ratio 0.2 of AlN film [51, 52] and the average reduced elastic modulus into the equation (4.5), we get the average elastic modulus of the AlN thin film is about 307Gpa which is in good agreement with the bulk material value 308GPa and the longitudinal elastic modulus value 340GPa.

4.4 PIEZOELECTRIC COEFFICIENT OF ALN THIN FILM

In order to measure the piezoelectric coefficient of the material, both the direct and converse piezoelectric effects can be employed. Here, we used the principle of the converse piezoelectric effect to measure the piezoelectric coefficient of the AlN thin film which is clamped to substrate. That is, by measuring the displacement of the surface of the AlN thin film which subjected to the external AC electric signal, we can calculate the piezoelectric coefficient d_{33}. Since the piezoelectric coefficient of AlN is relatively small, the resulting deformation excited by the electric field is correspondingly small. Thus how to measure the small deformation signal of the AlN accurately is important for the measurement of the d_{33}. This sensitive single beam laser interferometer system which is capable of resolving the displacement down to 10^{-3} Å in low frequency range was employed to measure the piezoelectric coefficient.

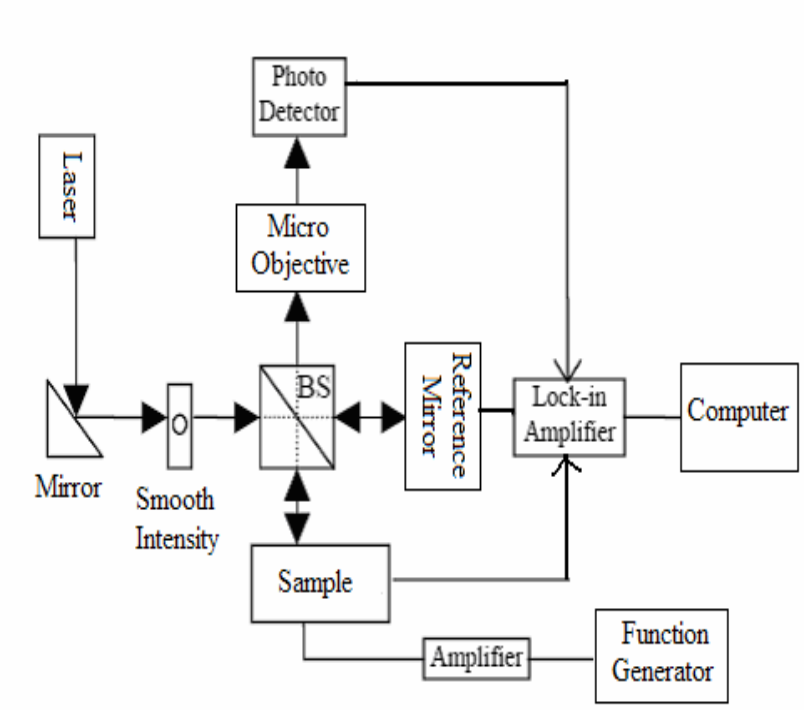

Figure 4.16: Experimental setup of laser interferometer for the measurement of piezoelectric coefficient.

The setup for the single beam laser interferometer is shown in figure 4.16. The beam from the He-Ne laser-light source is splitted into two equal parts by the beam splitter. One of the beams is incident on the reference mirror and the other on the sample to be tested where both lasers travel paths of equal length. There is a reflected beam from each surface and the beams are then combined in the beam splitter and the intensity is gathered at the photo detector. The absolute phase of each beam in turn depends on the distance between the beam splitter and the respective reflecting surface. If the surface of the test sample moves due to the external voltage applied, the absolute phase of the combined probe beam will change [53].

The phase shift is given by:

$$\varphi = 2(2\pi / \lambda)\Delta d = 2k\Delta d \tag{4.6}$$

where λ is the laser light's wavelength and Δd is the optical path-length difference of the two beams. The interference light intensity is

$$I = I_p + I_r + 2\sqrt{I_p I_r}\cos(2k\Delta d) \tag{4.7}$$

where I_p and I_r are the light intensities for the probing beam, where the sample is placed and the reference beam respectively. A relative change Δd between the two beams results in the change in the interference light intensity that can be detected by photo detector here. For convenience, equation (4.7) can be rewritten as:

$$I = 1/2(I_{\max} + I_{\min}) + 1/2(I_{\max} - I_{\min})\cos(2k\Delta d) \tag{4.8}$$

where $I_{\max}$ and $I_{\min}$ are the maximum and minimum interference light intensities which can be measured from the interference light intensity versus time curve.

Differentiating equation (4.8), we have:

$$dI / d(\Delta d) = -k(I_{\max} - I_{\min})\sin(2k\Delta d) \tag{4.9}$$

It can be seen that as the path-length difference is (2n+1)λ/8, the light change is maximized. In order to get the largest signal sensitivity, that is the largest $dI/d(\Delta d)$, we set the initial phase at $2k\Delta d=\pi/2$. Then the displacement becomes

$$\Delta d = d_{ac} + \pi/2 \tag{4.10}$$

Considering the ac intensity, equation (4.8) becomes to

$$I_{ac} = 1/2(I_{\max} - I_{\min})\sin(2kd_{ac}) = (I_{\max} - I_{\min})kd_{ac} \tag{4.11}$$

Since the sample vibration displacement is much less than the wavelength of the laser light, we have the approximation $\sin(2kd_{ac}) \approx 2kd_{ac}$ in equation (4.11).

If the light intensities are transformed in to the voltages by photo detectors, then we have:

$$V_{ac} = (V_{\max} - V_{\min})kd_{ac} \tag{4.12}$$

If a lock-in amplifier can measure V_{ac}, we have:

$$(V_{\max} - V_{\min})kd_0 = \sqrt{2}V_{lock-in} \tag{4.13}$$

where $d_{ac}=d_0cos(\omega t)$ is the sinusoidal displacement. Therefore

$$d_0 = \frac{\sqrt{2}V_{lock-in}}{(V_{\max} - V_{\min})k} \tag{4.14}$$

For piezoelectric coefficient d_{33}, we have

$$d_{33} = \frac{d_0}{d \cdot E} \tag{4.15}$$

where d is the thickness of the sample. Substituting $E = \frac{\sqrt{2}V_{in}}{d}$ into equation, we have

$$d_{33} = \frac{V_{lock-in}}{k(V_{\max} - V_{\min})V_{in}} \tag{4.16}$$

where V_{in} is the voltage of function generator.

By using the single beam laser interferometer method, we measured the effective piezoelectric coefficient of the AlN thin film in the four-layer composite resonator. The AlN thin film was deposited in 500^{o}C with 250W discharge power, and the substrate is sapphire.

The measured effective piezoelectric coefficient of thin AlN film in the composite resonator structure d_{33eff} is 2.9pm/V. Since the piezoelectric coefficient is measured under the fact that the AlN film is always clamped to the sapphire substrate, the stain and electric field ratio S_3/E_3 does not represent the real piezoelectric coefficient d_{33} of the free sample but an effective coefficient. While in the converse piezoelectric effect, the effective piezoelectric coefficient d_{33eff} and the real piezoelectric coefficient has the following relationship

$$d_{33eff} = d_{33} - 2d_{31}s_{13}^{E}/(s_{11}^{E} + s_{12}^{E}) \tag{4.17}$$

where s_{13}, s_{12},and s_{13} are the mechanical compliances of the piezoelectric film and d_{31} is the transverse piezoelectric coefficient. Since $d_{33} \approx -2d_{31}$, we have

$$d_{33} = d_{33eff}(s_{11}^E + s_{12}^E)/(s_{11}^E + s_{12}^E + s_{13}^E) \tag{4.18}$$

Substitute the values of s_{13}, s_{12},and s_{13} from literature [54] into equation (4.18), we get the real piezoelectric coefficient d_{33} is 4.17pm/V.

5.0 MODELING OF ALN THIN FILM BULK ACOUSTIC WAVE RESONATOR

5.1 INTRODUCTION

In recent years, with the strong progress in thin film technologies for complex materials systems such as PZT, ZnO and AlN, thin film bulk acoustic wave resonator (FBAR) and filter concepts are gaining more and more importance for RF and microwave frequency control applications. In bulk acoustic wave (BAW) resonator, an acoustic wave is excited electrically in a thin piezoelectric film; here the fundamental thickness vibration mode is employed. For resonators operating in the GHz range, thin film piezoelectric layer in the order of a few microns with desirable electromechanical properties (high Q and wide bandwidth) is required. Thus, the characterizations of thin film bulk acoustic wave resonators are important in determining the required design parameters for device and the developing suitable applications in the radio frequency range.

As one of the most important parameters, the electromechanical coupling coefficient k_t^2 of a resonator can determine the bandwidth of a filter. For lossless resonator with a single piezoelectric layer and ignored electrodes, the electromechanical coupling coefficient for thickness extensional mode is given by,

$$k_t^2 = \left(\frac{\pi}{2}\right) \cdot \frac{f_s}{f_p} \cdot \tan\frac{\pi}{2}\left(\frac{f_p - f_s}{f_p}\right) \tag{5.1}$$

In the resonance impedance spectra of the resonators, IEEE Std 176-1987 [55] defined the series resonant frequency f_s as the frequency corresponding to the minimum impedance and the parallel resonant frequency f_p as the frequency corresponding to the maximum impedance.

When k_t^2 is small, equation (5.1) is approximates to

$$k_t^2 = \frac{\pi^2}{4} \cdot \frac{f_s}{f_p} \cdot \frac{f_p - f_s}{f_p} \tag{5.2}$$

In order to determine the values of f_s and f_p, the impedance spectra of the thin film resonators around the resonance frequencies need to be obtained first. For multiplayer resonator or composite resonator, many approaches have been used to derive the input impedance. These include the equivalent circuit method [19, 56] and transfer matrix approach [57-60].

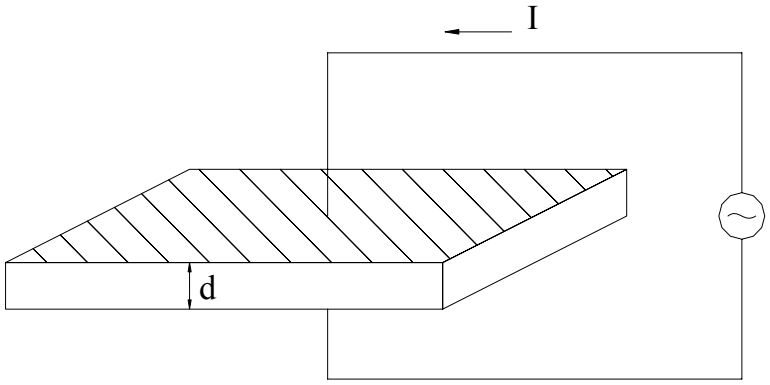

Figure 5.1: Thickness excitation of piezoelectric resonator.

For the bulk acoustic wave resonator, we can use Mason model [19] to investigate the impedance feature. First, consider the structure shown in Fig 5.1. The electrodes are ignored and the acoustic wave propagates in the single piezoelectric thin film layer. The equations derived by Mason model for the resonator are [19]:

$$F_1 = \frac{Z_0}{j\sin(kd)} \cdot (v_1 - v_2) + jZ\tan(\frac{kd}{2})v_1 + \frac{h}{j\omega} I \tag{5.3}$$

$$F_2 = \frac{Z_0}{j\sin(kd)} \cdot (v_1 - v_2) - jZ\tan(\frac{kd}{2})v_2 + \frac{h}{j\omega} I \tag{5.4}$$

$$V = \frac{h}{j\omega}(v_1 - v_2) + \frac{I}{j\omega C_0} \tag{5.5}$$

where d is the thickness of the piezoelectric layer, F_1 and F_2 are the forces on the top and bottom surface of the resonator respectively, v_1 and v_2 are the "acoustic" currents or acoustic velocities of the top and bottom surface plane of the resonator respectively, V is the external electric voltage, I is the electric current, C_0 is the static or "clamped" capacitance, $\omega = 2\pi f$ is the angular frequency, $k = \omega / v$, v is the longitudinal acoustic wave velocity in piezoelectric layer along the direction normal to the resonator surface, $h = e / \varepsilon^S$, where e is piezoelectric coefficient and the ε^S is the permittivity of piezoelectric materials under constant strain condition. $C_0 = \varepsilon^S S / d$ is the clamped capacitor of the resonator with area S, and $Z_0 = S\rho v$ is the acoustic impedance of the piezoelectric layer with density ρ.

The equivalent circuit of the single layer resonator is shown in Fig. 5.2. The piezoelectric layer can be seen as a three-port component. One is the electric port with the voltage V and current I. The other two ports are the mechanical ports presented by the forces F and the displacement velocity v. In equations (5.3) to (5.5), the current I is an independent variable, reflecting the fact that the electric field is composed of external and acoustically generated components. The form of equation (5.5) results in the appearance of a negative capacitance in the equivalent circuit in Fig. 5.2.

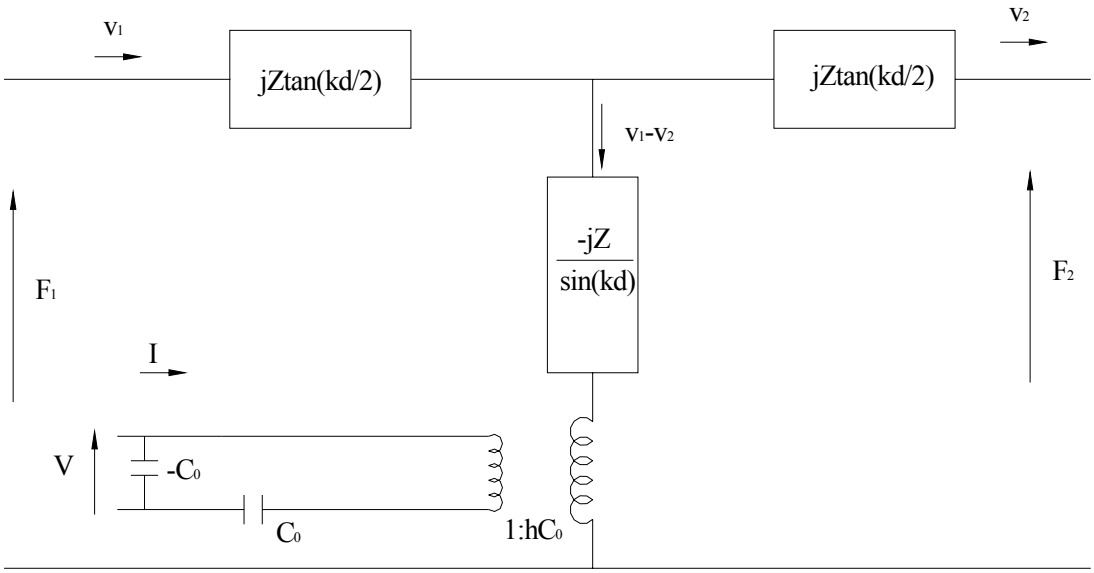

Figure 5.2: Mason model equivalent circuit of a thickness piezoelectric layer.

In the resonator shown in Fig. 5.1, the piezoelectric layer has mechanical free boundary condition that can be considered to be an acoustic short circuit (vacuum or air) on both sides. Thus F_1 and F_2 can be considered to be zero. After some mathematical conversion, equations (5.3) and (5.4) becomes

$$0 = Z_p\left(\frac{v_1}{j\tan(kd)} - \frac{v_2}{j\sin(kd)}\right) + \frac{h}{j\omega} I \tag{5.6}$$

$$0 = Z_p\left(\frac{v_1}{j\sin(kd)} - \frac{v_2}{j\tan(kd)}\right) + \frac{h}{j\omega} I \tag{5.7}$$

From the equations (5.6), and (5.7), we can get

$$\frac{v_1}{I} = \frac{v_2}{I} = \frac{-h}{jw} \cdot \frac{1}{Z_p/(j\tan(kd)) + Z_p/(j\sin(kd))} \tag{5.8}$$

Solving equations (5.5), (5.6) and (5.8) for the ratio $V / I = Z_{in}$, the input impedance of the single piezoelectric layer resonator shown in Fig. 5.1 is

$$Z_{in} = V / I = \frac{1}{j\omega C_0}(1 - k_t^2 \frac{\tan(kd/2)}{kd/2}) \tag{5.9}$$

where $k_t^2 = \frac{e^2}{c^D \varepsilon^S}$ is the electromechanical coupling coefficient of the piezoelectric film which can be calculate by equation (5.2). In this configuration, the larger k_t^2 is, the wider is the frequency band for which Z_{in} is inductive.

However, for the thin film resonator, there is more than one layer in the structure. Thus, we use the transfer matrix method to obtain the impedance spectrum of the multiple-layer resonator, and furthermore discuss the electromechanical coupling coefficient at various conditions.

5.2 TWO-LAYER COMPOSITE RESONATOR

When the thickness and the losses of the electrode layers and substrate materials cannot be ignored, the values and relative difference of the critical frequencies f_s and f_p depend on the material properties of piezoelectric, substrate and electrode materials, the resonator structure and geometry, and usually differ from those defined in lossless single layer resonator by a small amount. For this reason, the fundamental resonance of thin film resonators is usually quantified by the two figures of merit k_{eff}^2 and Q, where k_{eff}^2 is the effective coupling coefficient, and Q is quality factor. k_{eff}^2 is particularly used in filter design literature as a convenient measure of the bandwidth for bandpass filters. k_{eff}^2 is given by [55, Eq.(133)]

$$k_{eff}^2 = \frac{\left(f_p^2 - f_s^2\right)}{f_p^2} \tag{5.10}$$

Using the matrix approach, we can easily get the input impedance of the composite resonator with arbitrary layers. The matrix model of the two-layer composite resonator is shown in Fig. 5.3. The electrodes of the resonator are ignored in this model.

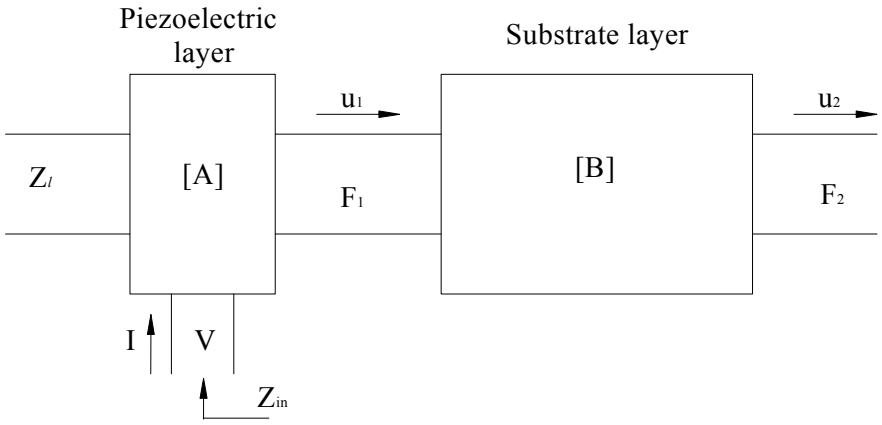

Figure 5.3: Matrix model for two-layer composite resonator.

Z_l represents the impedance of the left mechanical port in Fig. 5.3. In this model, Z_l is zero since the left surface of the piezoelectric layer is free. The electric port and the mechanical ports of the piezoelectric layer has the following relationship

$$\begin{bmatrix} V \\ I \end{bmatrix} = [A] \cdot \begin{bmatrix} F_1 \\ u_1 \end{bmatrix} \tag{5.11}$$

where the transfer matrix of the piezoelectric film [A] can be get from the Mason model,

$$[A] = \frac{1}{\phi H} \begin{bmatrix} 1 & j\phi^2 / \omega C_0 \\ j\omega C_0 & 0 \end{bmatrix} \cdot [A'] \tag{5.12}$$

with

$$H = \cos\gamma - 1 + jz_l \sin\gamma \tag{5.13}$$

and

$$\left[A^{'}\right] = \begin{bmatrix} \cos\gamma + jz_l \sin\gamma & Z_0(z_l \cos\gamma + j\sin\gamma) \\ j\sin\gamma / Z_0 & 2(\cos\gamma - 1) + jz_l \sin\gamma \end{bmatrix} \tag{5.14}$$

where $\phi = \left(k_t^2 C_o Z_o d/v\right)$ is the transformer ratio in the Mason's equivalent circuit, $\gamma = \omega d / v$ is the phase delay of the acoustic wave in the piezoelectric film.

The substrate layer has two acoustic ports with the following relationship

$$\begin{bmatrix} F_1 \\ u_1 \end{bmatrix} = \begin{bmatrix} \cos\gamma_{sb} & jZ_{sb}\sin\gamma_{sb} \\ j\sin\gamma_{sb}/Z_{sb} & \cos\gamma_{sb} \end{bmatrix} \cdot \begin{bmatrix} F_2 \\ u_2 \end{bmatrix} \tag{5.15}$$

where the subscript *sb* represents the substrate layer. $\gamma_{sb} = \omega d_{sb} / v_{sb}$ is the phase delay of the acoustic wave in the substrate film with thickness d_{sb} and acoustic wave velocity v_{sb}, and $Z_{sb} = S\rho_{sb} v_{sb}$ is the acoustic impedance of the substrate with density ρ_{sb}.

Since the right side of the substrate layer is mechanical free, F_2 is zero. Solve equations (5.11)-(5.15), we can get the electric impedance of the two-layer composite resonator

$$Z_{in} = \frac{V}{I} = \frac{1}{j\omega C_0}\left[1 - \frac{k_t^2}{\gamma}\frac{2\tan(\gamma/2) + z_{sb}\tan\gamma_{sb}}{1 + z_{sb}\tan\gamma_{sb}/\tan\gamma}\right] \tag{5.16}$$

where $z_{sb} = Z_{sb} / Z_0$ is the normalized acoustic impedance of the substrate layer.

Using equation (5.16), we can calculate the electric impedance of the two-layer composite resonator. In the calculation, a small imaginary part of the acoustic wave velocity is needed. Fig. 5.4 shows the impedance of a two-layer composite resonator consisting of a piezoelectric AlN film layer and a substrate Si layer. For comparison, the impedance of a single AlN film with the same thickness is shown in Fig. 5.5.

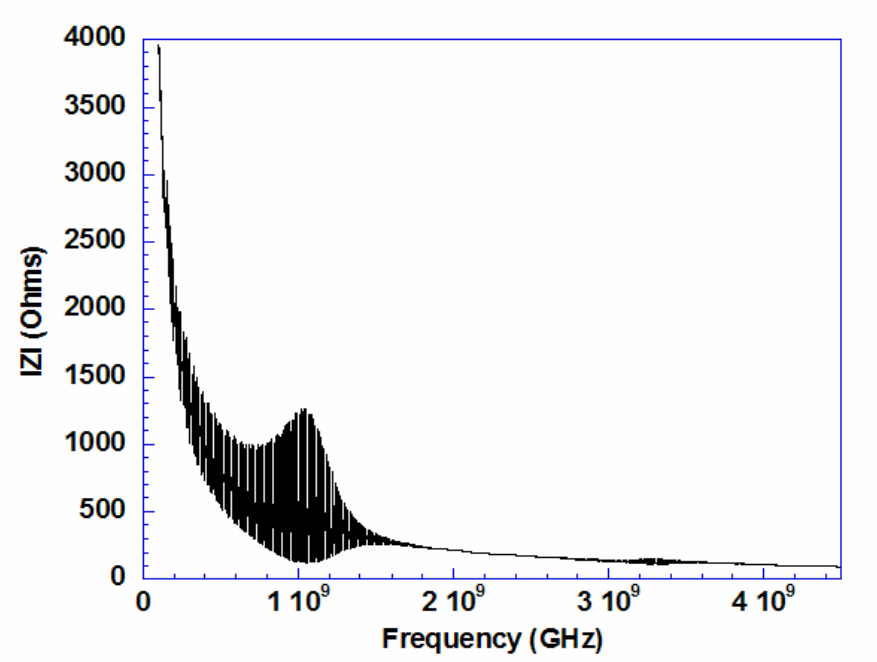

Figure 5.4: The impedance spectrum of an AlN/Si composite resonator.

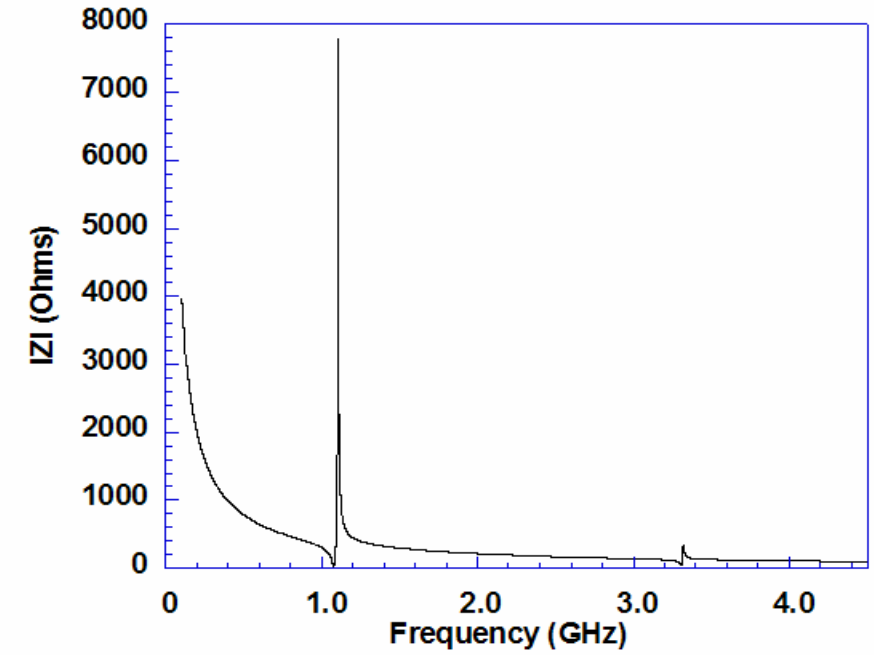

Figure 5.5: The impedance spectrum of the single layer AlN film resonator.

The impedance of the two-layer resonator follows a hyperbolic decrease that is the presentation of the static capacitance C_0 of the piezoelectric. For the two-layer resonator, there are multiple sharp peaks which are the resonator "modes". At a resonant mode, a standing wave is established in the thickness direction of the composite resonator. Since the substrate is much thicker than the piezoelectric layer, the mode's frequency is mainly determined by the acoustic properties and geometric parameters of the substrate. The multiple resonance modes have their maximum magnitude at a certain frequency that is near the resonance frequency for the single piezoelectric layer resonator.

Table 5.1 lists the material properties of the piezoelectric AlN film and silicon substrate used in the simulations within this chapter. It should be mentioned that a small imaginary part of the acoustic velocity has been introduced in the calculation which can stands for the mechanical quality factor of the material.

The mechanical quality factor of material is defined as $Q = c_{33}{}' / c_{33}{}''$, where $c_{33}{}'$ and $c_{33}{}''$ are the real part and imaginary part of the elastic stiffness of piezoelectric film at constant electric displacement $c_{33}^{D} = c_{33}{}' + jc_{33}{}''$. The acoustic wave velocity, $v = v' + jv'' = \sqrt{c_{33}^{D}/\rho}$, thus the mechanical Q factor can be approximately given by,

$$Q \approx \frac{1}{2} \cdot \frac{v'}{v''} \tag{5.17}$$

where the v' and v'' are the real and imaginary part of the velocity of the piezoelectric film respectively. By changing the ratio of the real part to the imaginary part of the acoustic velocity, and using equation (5.17) we can introduce different mechanical Q factors for the piezoelectric films in the simulation.

Table 5.1: Material properties of the AlN film and Si substrate

Material	Density (kg/m^3)	Acoustic Velocity (m/s)	k_t^2 (%)	Thickness (μm)	Area (m^2)	ε_r
AlN	3300	11050	6.25	5	2.5×10^{-8}	8.5
silicon	2320	8265	N/A	350	2.5×10^{-8}	N/A

5.3 THREE-LAYER COMPOSITE RESONATOR

In this section, we will use the transfer matrix approach to derive the electric input impedance of a three-layer composite resonator. Fig. 5.6(a) shows the schematic drawing of the three-layer thin film bulk acoustic wave resonator where the piezoelectric layer is sandwiched by top and bottom electrodes. In the simulation, we consider the electrodes have the same thickness. Fig. 5.6(b) shows the matrix model for a three-layer thin film resonator. E_1 and E_2 represent the electrodes and A represents the piezoelectric layer. Similarly, A can be treated as a three-port component with one electric terminal port and two acoustic terminal ports. The left electrode is a two port acoustic device with the following transfer matrix relationship

$$\begin{bmatrix} F_1 \\ u_1 \end{bmatrix} = \begin{bmatrix} \cos\gamma_{e1} & jZ_{e1}\sin\gamma_{e1} \\ j\sin\gamma_{e1}/Z_{e1} & \cos\gamma_{e1} \end{bmatrix} \cdot \begin{bmatrix} F_1' \\ u_1' \end{bmatrix} \tag{5.18}$$

where the subscript $e1$ represents the left electrode shown in figure 6(b). Because the left side of the electrode exposes to air and can be treated as mechanically free boundary condition, the force F_1 should be zero.

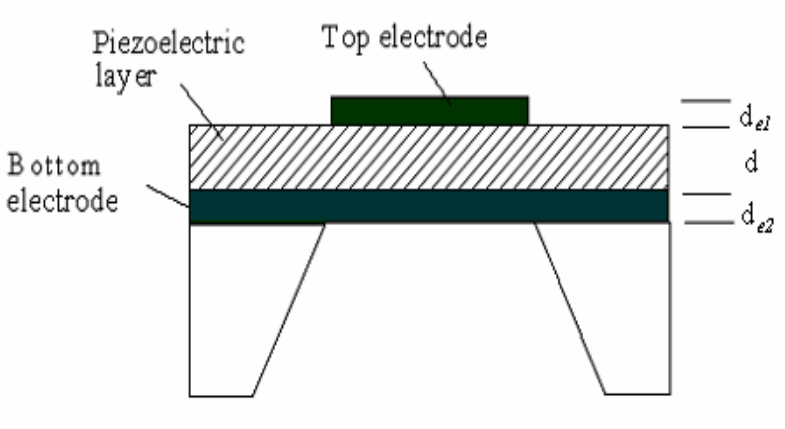

(a)

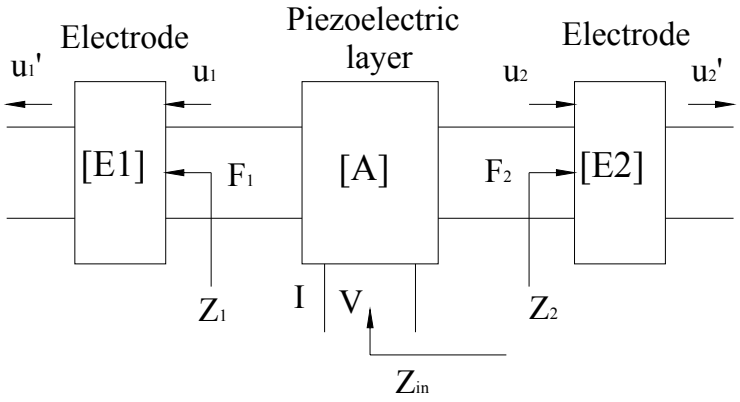

(b)

Figure 5.6: (a) Schematic view and (b) transfer matrix model of three-layer thin film bulk acoustic wave resonator.

From equation (5.18), the acoustic impedance of the left electrode can be obtained as

$$Z_1 = \frac{F_1}{u_1} = jZ_{e1} \tan \gamma_{e1} \tag{5.19}$$

Similarly, the transfer matrix of the right electrode port is

$$\begin{bmatrix} F_2 \\ u_2 \end{bmatrix} = \begin{bmatrix} \cos \gamma_{e2} & jZ_{e2} \sin \gamma_{e2} \\ j \sin \gamma_{e2} / Z_{e2} & \cos \gamma_{e2} \end{bmatrix} . \begin{bmatrix} F_2' \\ u_2' \end{bmatrix} \tag{5.20}$$

where the subscript *e*2 represents the left electrode shown in figure 6(b). With $F_2^{'} = 0$, then the acoustic impedance of the right electrode is

$$Z_2 = \frac{F_2}{u_2} = jZ_{e2}\tan\gamma_{e2} \tag{5.21}$$

If the left electrode port is considered as the acoustic backing port terminated with acoustic impedance Z_1, then the electric pair V and I can be calculated as

$$\begin{bmatrix} V \\ I \end{bmatrix} = [A]\cdot\begin{bmatrix} F_2 \\ u_2 \end{bmatrix} \tag{5.22}$$

where $[A]$ is the same as defined in equations (5.12)-(5.14).

Substitution of equations (5.12)-(5.14), (5.19) and (5.21) into (5.22), we can obtain the electric input impedance of such a three-layer thin film resonator as following

$$Z_{in} = \frac{V}{I} = \frac{1}{j\omega C_0}\left[1 - \frac{k_t^2}{\gamma}\frac{(z_1+z_2)sin\gamma + j2(1-cos\gamma)}{(z_1+z_2)cos\gamma + j(1+z_1z_2)sin\gamma}\right] \tag{5.23}$$

where $z_1 = Z_1/Z_0$ and $z_2 = Z_2/Z_0$ are the normalized acoustic impedance of the left electrode layer and the right electrode. It should be pointed out that equation (5.23) is in the same form as that derived for a four-layer composite resonator in the literature [61]. However in the four-layer composite resonator model, z_1 and z_2 are the acoustic loading impedances on both sides of the piezoelectric layer including the substrate.

Equation (5.23) can then be used to simulate the impedance spectrum of a three-layer thin film resonator. The input impedance response of resonators consisting of AlN film sandwiched by two Al electrodes is shown in Fig. 5.7. It can be seen that the resonance frequency will decrease with the increase of the thickness of the AlN film. Table 5.1 and 5.2 list the parameters used in the simulation. Quality factors for both the piezoelectric thin film layer and the electrode layer have been considered in the simulation by introducing an imaginary part to the acoustic

velocity (a complex number) for each of the layers. From the impedance characteristics, the effective electromechanical coupling coefficient can be calculated by using equation (5.10).

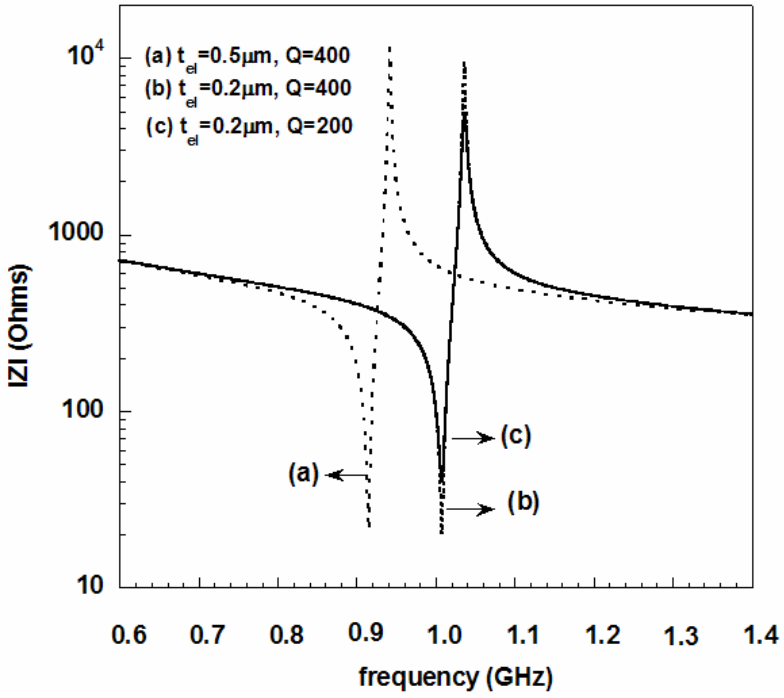

Figure 5.7: The impedance of an Al/AlN/Al three-layer composite resonator as a function of frequency.

Table 5.2: Material properties of the electrodes

Electrode	Density (kg/m^3)	Acoustic Velocity (m/s)	Mechanical Q at about 1 GHz
Al	2700	6418	480
Au	19320	1963	2000

As discussed before, k_{eff}^2 is a parameter representing the relative frequency spacing between the series resonance frequency and the parallel resonance frequency and ultimately determines the bandwidth of a filter that is connected electrically or mechanically by thin film resonators. In

order to understand the resonator performance with respect to the thin film materials properties and geometries, we simulated the effective electromechanical coupling coefficient by varying some different factors including the thickness of the electrodes, electrode materials and the Q factors of the piezoelectric thin film layers.

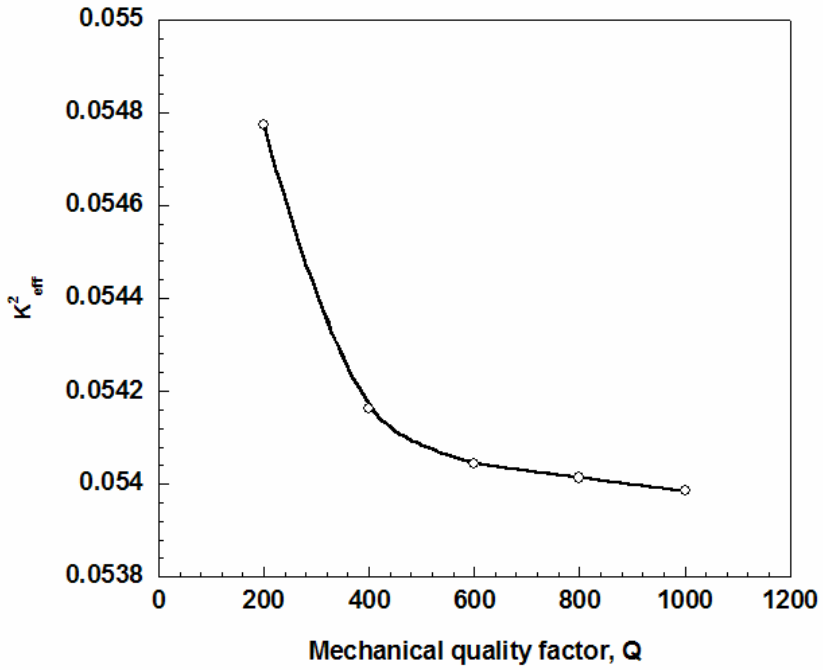

Figure 5.8: Effective coupling coefficient as a function mechanical Q for three-layer AlN thin film resonators.

Fig. 5.8 shows the effect of mechanical Q of the piezoelectric AlN film on the effective coupling constant k_{eff}^2 of the thin film resonator. In the simulation, the thickness of the Al electrodes is 0.2μm. The simulation results show that k_{eff}^2 decreases with the increase of the mechanical Q. When the Q is large enough, k_{eff}^2 approaches a stable value, which is about $\frac{8}{\pi^2}k_t^2$ [62]. It should be pointed out that the mechanical Q factor for a piezoelectric thin film largely

depends on the thin film quality and orientation, which therefore depends on the deposition methods and processing conditions.

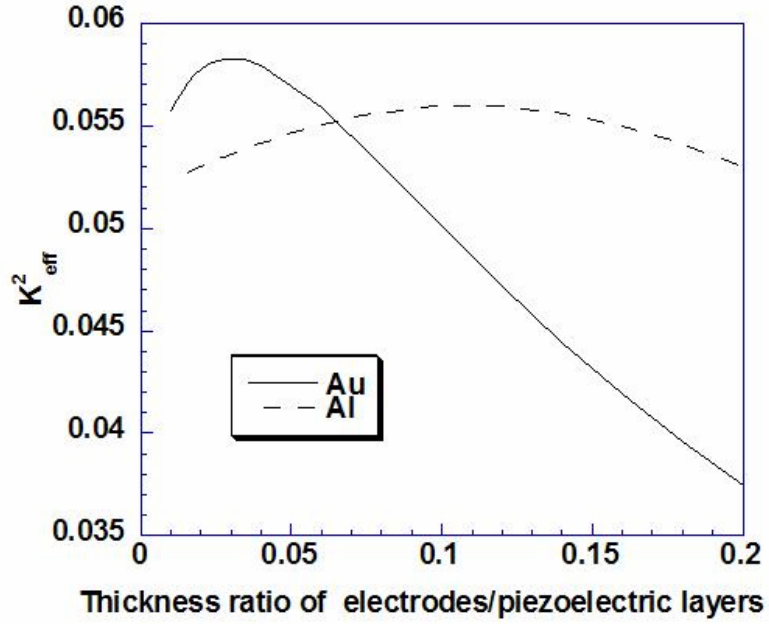

Figure 5.9: Effective coupling coefficient as a function of electrode-to-AlN thickness ratio for the three-layer composite resonator.

Fig. 5.9 shows the effective coupling coefficient versus thickness ratio of electrode layer to piezoelectric AlN layer for three-layer thin film resonators. In this simulation, the mechanical Q of the AlN film is 400. The results indicate that with the increase of the electrode layer thickness k_{eff}^2 initially increases and reaches a maximum value near thickness ratios of 0.03 and 0.12 for gold and aluminum electrodes, respectively. The increase in effective coupling coefficient can be attributed to the improved match in the distribution of acoustic standing wave to the linear distribution of applied electric potential [63]. With further increased electrode thickness, k_{eff}^2 begins to drop since more of the resonator volume becomes occupied by non-piezoelectric

electrode material. The use of a thin layer of the gold electrode, which has higher acoustic impedance than Al, has more significant effect on k_{eff}^2 .

5.4 FOUR-LAYER THIN FILM RESONATOR

In this section, the modeling of four-layer BAW resonator with a thin film support layer or substrate layer is discussed. The characteristics of the four-layer BAW resonator with thick substrate will be studied in chapter 7. In the fabrication process, usually, a support layer or substrate layer such as SiO_2, AlN or Si_3N_4 thin film to the membrane type FBAR is incorporated to increase the mechanical property of the resonator structure; in addition, it can introduce more special properties such as the temperature compensation in the resonator.

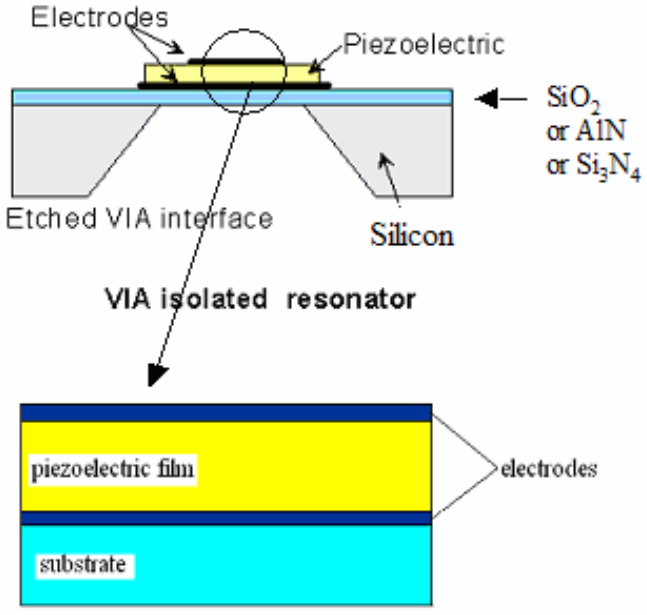

Figure 5.10: The schematic four-layer structure of thin film bulk acoustic wave resonator.

Fig. 5.10 shows the schematic drawing of the four-layer thin film bulk acoustic wave resonator with top and bottom electrodes. In the simulation, we consider the electrodes have the same thickness. Fig. 5.11 shows the matrix model for a four-layer thin film resonator. E_1 and E_2 represent the electrodes, A represents the piezoelectric layer and B represents the support layer or substrate layer. Piezoelectric layer A is a three-port component with one electric terminal port and two acoustic terminal ports.

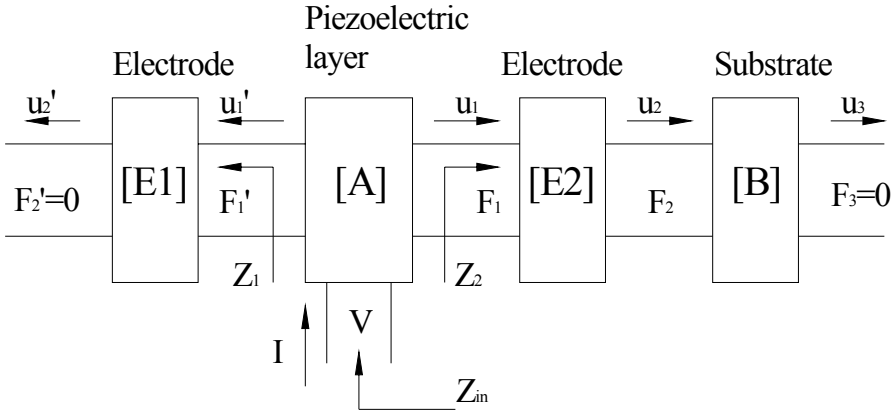

Figure 5.11: Matrix model for four-layer composite resonator.

It can be seen that, the left side of the piezoelectric layer in four-layer composite resonator model is the same with that in the three-layer model. Thus, in the four-layer resonator model:

$$Z_1 = \frac{F_1^{'}}{u_1^{'}} = jZ_{e1}\tan\gamma_{e1} \tag{5.24}$$

On the other hand, the transfer matrix of the right electrode port is

$$\begin{bmatrix} F_1 \\ u_1 \end{bmatrix} = \begin{bmatrix} \cos\gamma_{e2} & jZ_{e2}\sin\gamma_{e2} \\ j\sin\gamma_{e2}/Z_{e2} & \cos\gamma_{e2} \end{bmatrix} \cdot \begin{bmatrix} F_2 \\ u_2 \end{bmatrix} \tag{5.25}$$

$$\begin{bmatrix} F_2 \\ u_2 \end{bmatrix} = \begin{bmatrix} \cos\gamma_{e2} & jZ_{e2}\sin\gamma_{e2} \\ j\sin\gamma_{e2}/Z_{e2} & \cos\gamma_{e2} \end{bmatrix} \cdot \begin{bmatrix} F_3 \\ u_3 \end{bmatrix} \tag{5.26}$$

$$F_3 = 0 \tag{5.27}$$

From equations (5.25), (5.26) and (5.27), the acoustic impedance of the right electrode and substrate layer can be derived as

$$Z_2 = \frac{F_1}{u_1} = j\frac{Z_{sb}\tan(\gamma_{sb}) + Z_{e2}\tan(\gamma_{e2})}{1-(Z_{sb}/Z_{e2})\tan(\gamma_{sb})\tan(\gamma_{e2})} \tag{5.28}$$

Following the same way used in the three-layer resonator modeling, we can get the input electric impedance of the four-layer composite resonator:

$$Z_{in} = \frac{V}{I} = \frac{1}{j\omega C_0}\left[1 - \frac{k_t^2}{\gamma}\frac{(z_1+z_2)sin\gamma + j2(1-cos\gamma)}{(z_1+z_2)cos\gamma + j(1+z_1z_2)sin\gamma}\right] \tag{5.29}$$

where z_1 and z_2 are the normalized acoustic impedances on both sides of the piezoelectric layer.

Using equation (5.29), we can get the impedance spectrum of the four-layer thin film BAW resonator. Table 5.3 lists some material properties of substrate layers used in the calculation.

Table 5.3: Material properties of substrate layers

	Density ρ (kg/m^3)	Acoustic Velocity (m/s)	Mechanical Q
SiO_2	2200	5760	2700
Si_3N_4	3100	8032	1000

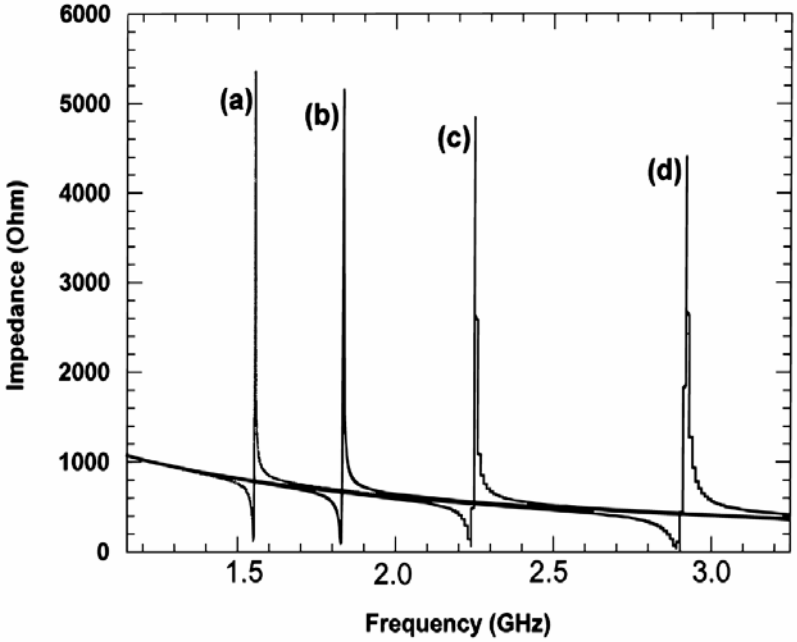

Figure 5.12: The impedance spectra of Al/AlN/Al/SiO_2 four-layer composite resonators, a) t_{sb}=1.0μm, b) t_{sb}=0.8μm, c) t_{sb}=0.6μm, and d) t_{sb}=0.4μm.

Fig. 5.12 shows the simulated input electric impedance spectra of four-layer thin film BAW resonators with different thickness of the SiO_2 substrate layer. The thickness of the AlN thin film is 1.0 μm in the calculation. SiO_2 thin membrane is often used as etch stop in the MEMS device fabrication. It is convenient to use SiO_2 as the support membrane in thin film resonator fabrication. In addition, positive temperature coefficient (TC) of elastic constant can be obtained from SiO_2 material. From the impedance spectrum, the fundamental series resonant frequency f_s and the parallel resonant frequency f_p can be determined. Thus the effective coupling coefficient k_{eff}^2 can be calculated by equation (5.10). Fig. 5.12 also shows that the resonant frequencies of the thin film resonators decrease with the increase of the substrate thickness.

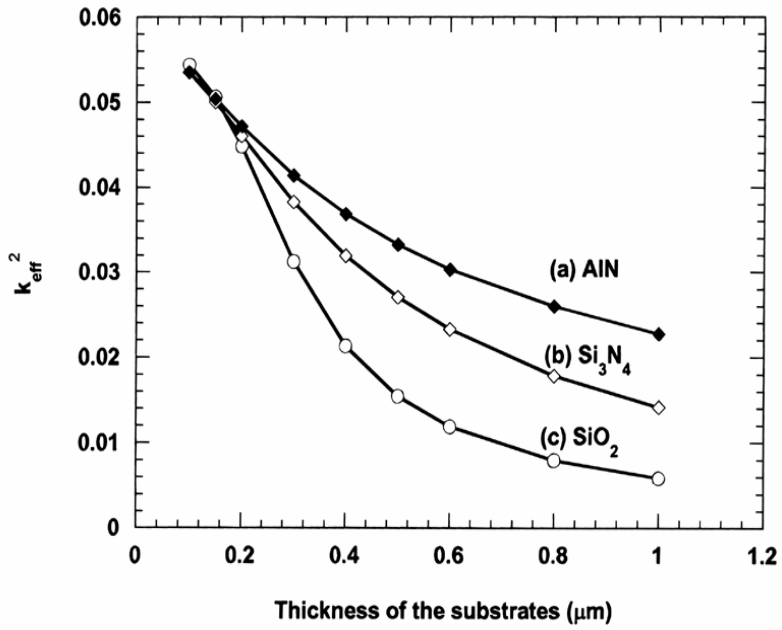

Figure 5.13: Effective coupling coefficient as a function of substrate thickness for the four-layer AlN thin film resonators with different substrate materials.

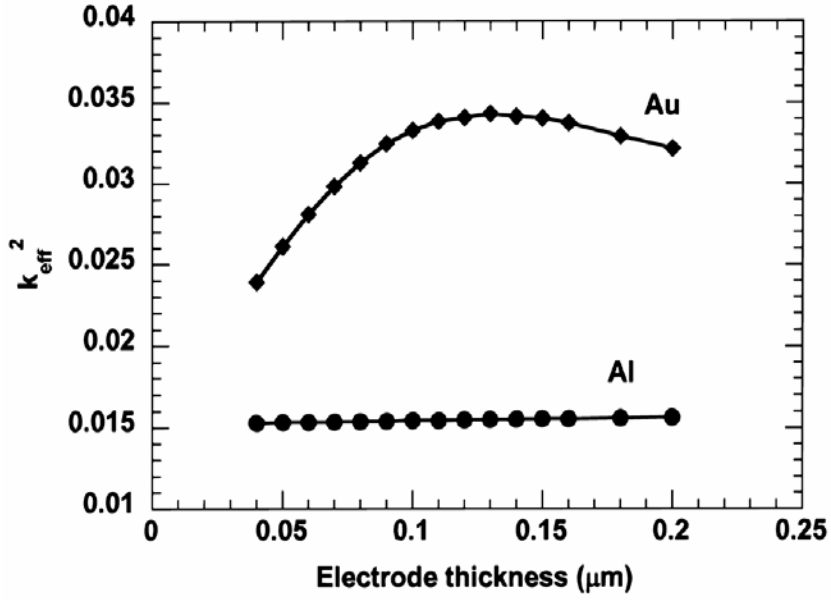

Figure 5.14: Effective coupling coefficient as a function of the electrode thickness for the four-layer AlN thin film resonators with Al and Au as electrodes.

Fig. 5.13 shows effective coupling coefficient k_{eff}^2 as a function of substrate thickness for the four-layer AlN thin film resonators. Al electrodes with 0.1μm thickness are used in the simulation. Different substrates including SiO_2, Si_3N_4 and AlN thin film are used in the simulation. It can be seen that k_{eff}^2 decreases with the increase of the substrates thickness since more resonator volume is occupied by non-piezoelectric substrate material. The use of AlN as substrate leads to higher effective coupling coefficient than SiO_2 and Si_3N_4 for AlN thin film resonators. This can be attributed to a better match in acoustic impedance.

Fig. 5.14 shows the effective coupling coefficient k_{eff}^2 as a function of the electrode thickness for the AlN four-layer thin fim resonators. Both Al and Au electrodes with 0.5μm thickness SiO_2 substrate are used in thin film resonator structure for the simulation. It can be seen the AlN resonators with Au electrodes have higher k_{eff}^2 than those resonators with Al electrodes. Thus, the use of a thin layer of the gold electrode, which has higher acoustic impedance than Al, has a more enhancement effect on k_{eff}^2. Furthermore, due to the match in the distribution of acoustic standing wave to the linear distribution of applied electric potential, a peak k_{eff}^2 occurs at a certain electrode thickness.

6.0 FREQUENCY CONTROL AND TUNING OF THIN FILM BULK ACOUSTIC WAVE RESONATORS

The need for better filters and signal conditioning is continuously changing to address a wide range of applications including frequency controls, signal processing, RF and microwave communications, navigation and many others. Specifically, for mobile communication applications in the GHz range, small sized bandpass filters with low insertion loss and good out of band rejection are required. Since the bulk acoustic wave (BAW) resonators and filters are at least an order of magnitude smaller than dielectric resonators or lumped elements, and have much lower insertion loss than surface acoustic wave (SAW) devices, these devices have gained increasing interests in the RF communication and high frequency control applications [11,64-66]. However, for on-chip FBAR and filter fabrication, variation of thickness of the resonator layers caused in thin film deposition process will lead to resonance frequency shift. Moreover, some environmental change such as the ambient temperature variation will also induce the resonance frequency shift during the applications of the filter. Thus, the frequency control and tuning techniques become important for the design, fabrication, and application of the BAW resonators and filters. In this chapter, the introduction of the passive layer and external impedance and the incorporation of the SiO_2 support layer with positive temperature coefficient of elastic constant to the FBAR resonator structure to control and tune the resonance frequency are studied.

6.1 FREQUENCY CONTROL AND TUNING BY PASSIVE LAYER AND EXTERNAL IMPEDANCE

6.1.1 Electric input impedance modeling

In order to control and tune the resonance frequency of the FBARs, the resonator structure consisting of an active piezoelectric AlN thin film layer, a passive piezoelectric layer, electrode layers is investigated. Moreover, the effect of the external electric impedance that is connected to the passive layer is also been studied. It will be shown that the introduction of passive AlN layer and external impedance in the thin film resonator structure can tune the resonance frequency and effective electromechanical coupling coefficient of the resonator.

It has been mentioned that, when the effect of electrode and substrate layers and the losses of materials cannot be ignored, the values and relative difference of the critical frequencies f_s and f_p usually differ from those defined in lossless single layer resonator by a small amount. For this reason, the resonance characteristics of a thin film resonator are usually quantified by the two figures-of-merit k_{eff}^2 and Q, where k_{eff}^2 is the effective coupling coefficient, and Q is the quality factor. k_{eff}^2 is a convenient measure of the bandwidth for bandpass filters which has been defined in equation (5.10).

It can be seen that k_{eff}^2 is determined by the series resonance frequency f_s and parallel resonance frequency f_p. In order to determine the values of f_s and f_p, we need to get the impedance spectrum of a thin film resonator at the resonance frequency first. Here, we will derive the input electric impedance of the AlN thin film composite resonator by using the transfer matrix approach and then to evaluate the frequency characteristics, especially the effects

of passive layer and external impedance on the effective coupling coefficient k_{eff}^2 of the resonator.

We consider AlN membrane-type thin film resonator with two piezoelectric layers and three electrodes layers. Fig. 6.1 shows the schematic structure of thin film resonator. The resonator structure can be fabricated by sputtering deposition of AlN thin film and metal electrode films followed by thin film patterning and silicon micromachining. The critical issue in the thin film bulk acoustic resonator fabrication is the deposition of c-axis oriented AlN film and its patterning.

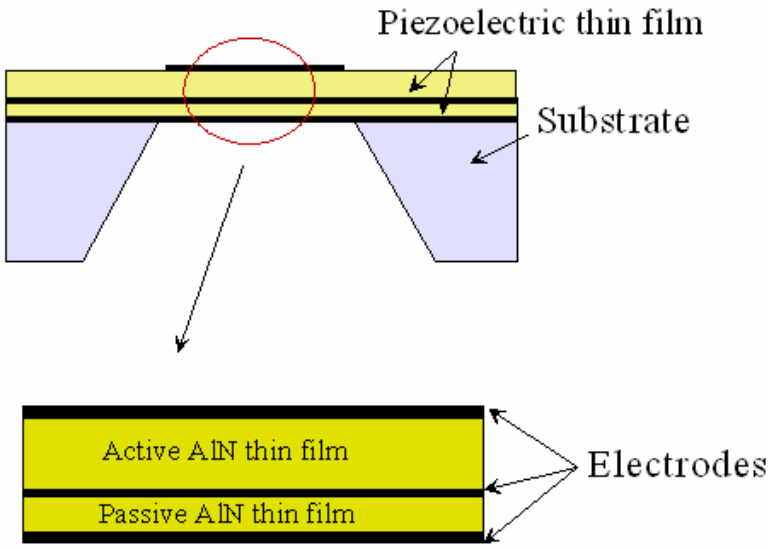

Figure 6.1: The schematic structure of the AlN thin film bulk acoustic wave resonator with a passive piezoelectric layer.

The matrix model for the five-layer thin film resonator is shown in Fig. 6.2, in which A represents the active piezoelectric layer, B_1, B_2 and B_3 represent the electrodes and C represents the passive piezoelectric layer. A and C can be considered as a three-port component with one electric terminal port and two acoustic terminal ports.

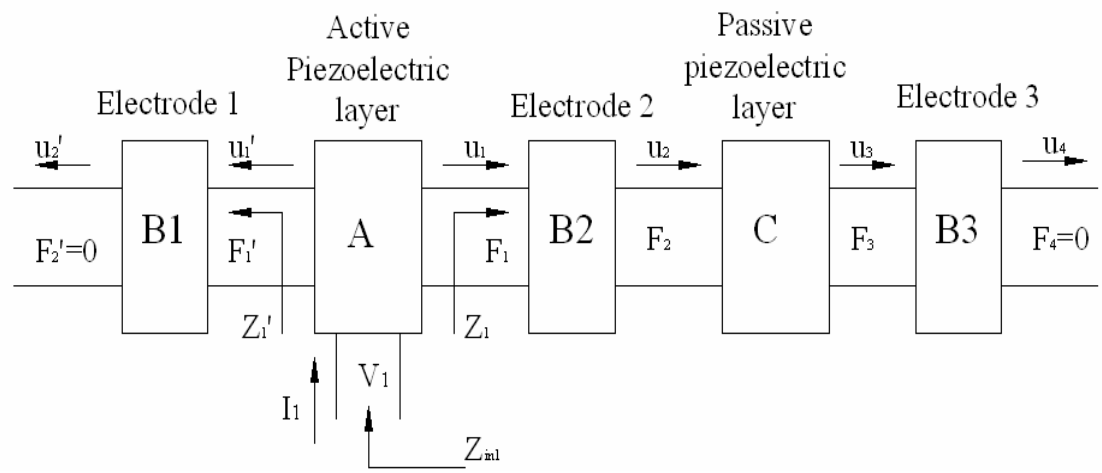

Figure 6.2: Matrix model for thin film bulk acoustic wave resonator.

Fig. 6.3 shows the Mason equivalent circuit of the passive piezoelectric layer. In the equivalent circuit, C_{02} represents the clamped capacitance of the passive piezoelectric layer, and $Z_l = R_l + jX_l$ is the external electric impedance that can be electric resistance, inductance and capacitance [19, 56].

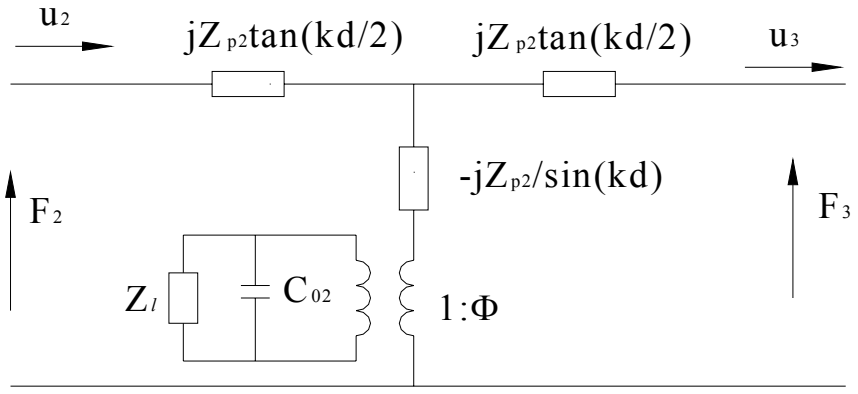

Figure 6.3: Equivalent circuit mode of the passive piezoelectric layer.

The total electric impedance of the clamped capacitance C_{02} and the electric load impedance Z_l is calculated as:

$$Z_E = Z_l // Z_{C_{02}} = \frac{R_l + j[X_l - \omega C_{02}(R_l^2 + X_l^2)]}{(1-\omega C_{02} X_l)^2 + (\omega C_{02} R_l)^2} \tag{6.1}$$

The reflected mechanical impedance through the electromechanical transformer is:

$$Z_M = \phi_{p2}^2 Z_E \tag{6.2}$$

where $C_{02} = \varepsilon_{33}^S S / d_{p2}$ is the clamped capacitor of the passive piezoelectric layer with area *S*, d_{p2} is the thickness of the passive piezoelectric layer, ε_{33}^S is the dielectric permittivity, $\phi_{p2} = \sqrt{k_t^2 C_{02} Z_{p2} v_{p2} / d_{p2}}$ is the transformer ratio in the Mason's equivalent circuit, $Z_{p2} = S\rho_{p2} v_{p2}$ is the acoustic impedance of the passive piezoelectric layer with density ρ_{p2}, v_{p2} is the longitudinal acoustic wave velocity in the passive piezoelectric layer along the direction normal to the resonator surface, $\omega = 2\pi f$ is the angular frequency, and k_t^2 is the electromechanical coupling coefficient of the thin film piezoelectric material. Here, we assume the two AlN piezoelectric layers have the same k_t^2. The subscript *p*2 represents the passive piezoelectric layer.

The transfer matrix relationship of the left electrode in Fig. 6.2 is

$$\begin{bmatrix} F_1' \\ u_1' \end{bmatrix} = \begin{bmatrix} \cos\gamma_{e1} & jZ_{e1}\sin\gamma_{e1} \\ j\sin\gamma_{e1}/Z_{e1} & \cos\gamma_{e1} \end{bmatrix} \cdot \begin{bmatrix} F_2' \\ u_2' \end{bmatrix} \tag{6.3}$$

where *F* and *u* represent force and displacement velocity, respectively. Z and γ are the acoustic impedance and the phase delay, $Z_{e1} = S\rho_{e1} v_{e1}$ is the acoustic impedance of the electrode 1, $\gamma_{e1} = \omega d_{e1} / v_{e1}$ is the phase delay of the electrode 1, where l_{e1} and v_{e1} are the thickness and

acoustic wave velocity of electrode 1. The subscript $e1$ represents the electrode 1. Since the left surface of electrode 1 is free, we can get $F_2^{'} = 0$. Thus, the acoustic impedance of the electrode 1 can be obtained by solving the equation (6.3),

$$Z_1^{'} = \frac{F_1^{'}}{u_1^{'}} = jZ_{e1} \tan \gamma_{e1} \tag{6.4}$$

Similarly, on the right side of the resonator, the matrix relationship of the electrode 3 is

$$\begin{bmatrix} F_3 \\ u_3 \end{bmatrix} = \begin{bmatrix} \cos \gamma_{e3} & jZ_{e3} \sin \gamma_{e3} \\ j \sin \gamma_{e3} / Z_{e3} & \cos \gamma_{e3} \end{bmatrix} \cdot \begin{bmatrix} F_4 \\ u_4 \end{bmatrix} \tag{6.5}$$

where $Z_{e3} = S\rho_{e3}v_{e3}$, $\gamma_{e3} = \omega d_{e3}/v_{e3}$ are the acoustic impedance and phase delay of the electrode 3 respectively, and the subscript $e3$ represents the electrode 3.

If the left electrode port of the active piezoelectric layer is considered as the acoustic backing port terminated with acoustic impedance $Z_1^{'}$, then the electric pair V_1 and I_1 can be calculated as

$$\begin{bmatrix} V_1 \\ I_1 \end{bmatrix} = [A] \cdot \begin{bmatrix} F_1 \\ u_1 \end{bmatrix} \tag{6.6}$$

where

$$[A] = \frac{1}{\phi H_A} \begin{bmatrix} 1 & j\phi^2 / \omega C_{01} \\ j\omega C_{01} & 0 \end{bmatrix} \cdot [A^{'}] \tag{6.7}$$

with

$$H_A = \cos \gamma - 1 + jz_1^{'} \sin \gamma \tag{6.8}$$

and

$$[A^{'}] = \begin{bmatrix} \cos \gamma + jz_1^{'} \sin \gamma & Z_0 (z_1^{'} \cos \gamma + j \sin \gamma) \\ j \sin \gamma / Z_0 & 2(\cos \gamma - 1) + jz_1^{'} \sin \gamma \end{bmatrix} \tag{6.9}$$

where $z_1^{'} = Z_1^{'} / Z_0$ is the normalized $Z_1^{'}$ with respect to the impedance of active piezoelectric layer, $\gamma = \omega d / v$ is the phase delay in layer A, C_{01} is the clamped capacitance of the layer A, $\phi = \sqrt{k_t^2 C_{01} Z v / d}$ is the transformer ratio in the Mason's equivalent circuit for layer A.

For the electrode 2, the transfer matrix relations is

$$\begin{bmatrix} F_1 \\ u_1 \end{bmatrix} = \begin{bmatrix} \cos\gamma_{e2} & jZ_{e2}\sin\gamma_{e2} \\ j\sin\gamma_{e2}/Z_{e2} & \cos\gamma_{e2} \end{bmatrix} \cdot \begin{bmatrix} F_2 \\ u_2 \end{bmatrix} \tag{6.10}$$

where the subscript $e2$ represents the electrode 2, $Z_{e2} = S\rho_{e2}v_{e2}$ is the acoustic impedance of electrode 2 and $\gamma_{e2} = \omega d_{e2} / v_{e2}$ is the phase delay in electrode 2.

By analyzing the equivalent circuit shown in Fig. 6.3, we can get the equations in which F_2 and u_2 are the functions of the variant F_3 and u_3. Then we can obtain the transfer matrix relation of the passive piezoelectric layer

$$\begin{bmatrix} F_2 \\ u_2 \end{bmatrix} = [C] \cdot \begin{bmatrix} F_3 \\ u_3 \end{bmatrix} = \begin{bmatrix} C_{11} & C_{12} \\ C_{21} & C_{22} \end{bmatrix} \cdot \begin{bmatrix} F_3 \\ u_3 \end{bmatrix} \tag{6.11}$$

where

$$\begin{cases} C_{11} = \dfrac{Z_{p2}\cos\gamma_{p2} + jZ_M\sin\gamma_{p2}}{Z_{p2} + jZ_M\sin\gamma_{p2}} \\ C_{12} = \dfrac{jZ_{p2}^2\sin(\gamma_{p2}) - 4Z_{p2}Z_M\sin^2(\gamma_{p2}/2)}{Z_{p2} + jZ_M\sin(\gamma_{p2})} \\ C_{21} = \dfrac{j\sin\gamma_{p2}}{Z_{p2} + jZ_M\sin\gamma_{p2}} \\ C_{22} = \dfrac{Z_{p2}\cos\gamma_{p2} + jZ_M\sin\gamma_{p2}}{Z_{p2} + jZ_M\sin\gamma_{p2}} \end{cases} \tag{6.12}$$

where the subscript $p2$ represents the passive piezoelectric layer , $Z_{p2} = S\rho_{p2}v_{p2}$ is the acoustic impedance of the passive piezoelectric layer and $\gamma_{p2} = \omega d_{p2} / v_{p2}$ is the phase delay in this layer.

Combining Eqs. (6.5), (6.10) and (6.11), we have:

$$\begin{bmatrix} F_1 \\ u_1 \end{bmatrix} = \begin{bmatrix} \cos\gamma_{e2} & jZ_{e2}\sin\gamma_{e2} \\ j\sin\gamma_{e2}/Z_{e2} & \cos\gamma_{e2} \end{bmatrix} \cdot \begin{bmatrix} C_{11} & C_{12} \\ C_{21} & C_{22} \end{bmatrix} \cdot \begin{bmatrix} \cos\gamma_{e3} & jZ_{e3}\sin\gamma_{e3} \\ j\sin\gamma_{e3}/Z_{e3} & \cos\gamma_{e3} \end{bmatrix} \cdot \begin{bmatrix} F_4 \\ u_4 \end{bmatrix} \tag{6.13}$$

Since the right side of the electrode 3 is force free, $F_4 = 0$. From equation (6.13), we can get:

$$Z_1 = \frac{F_1}{u_1} = \frac{jC_{11}Z_{e3}\tan\gamma_{e3} - C_{21}Z_{e2}Z_{e3}\tan\gamma_{e2}\tan\gamma_{e3} + C_{12} + jC_{22}Z_{e2}\tan\gamma_{e2}}{-C_{11}Z_{e3}\tan\gamma_{e2}\tan\gamma_{e3}/Z_{e2} + jC_{21}Z_{e3}\tan\gamma_{e3} + jC_{12}\tan\gamma_{e2}/Z_{e2} + C_{22}} \tag{6.14}$$

By solving equations (6.6)-(6.9), we can obtain input the electric impedance of the resonator:

$$Z_{in} = \frac{V}{I} = \frac{1}{j\omega C_{01}}\left[1 - \frac{k_t^2}{\gamma}\frac{(z_1 + z_1')\sin\gamma + j2(1-\cos\gamma)}{(z_1 + z_1')\cos\gamma + j(1 + z_1 z_1')\sin\gamma}\right] \tag{6.15}$$

where $z_1 = Z_1 / Z_0$ is the normalized acoustic impedance. Equation (6.15) is consistent with thin film resonators with simple structure such as electrode-AlN thin film-electrode triple layer resonator.

6.1.2 Resonance frequency tuning of the FBAR resonator

Equation (6.15) can then be used to simulate the impedance spectrum of the composite resonator. Tables 5.1 and 5.3 list the parameters used in the simulation within this chapter. It should be pointed out that the elastic constant temperature dependence dlnE/dT is -25×10^{-6} and 85×10^{-6} [67] for AlN and SiO_2 respectively. The mechanical quality factor for the piezoelectric thin film layer has been considered in the simulation by introducing an imaginary part to the acoustic velocity (a complex number). With the simulation of the impedance spectrum, f_s and f_p can be calculated. Thus the effective electromechanical coupling coefficient can be obtained by using equation (5.10).

In the simulation, the thickness of the active piezoelectric and passive piezoelectric layers is assumed to be 2μm and 1μm, respectively. Fig. 6.4 shows the input electric impedance spectra of

composite thin film resonators with and without external impedance load. The external electric load is introduced by connected to the passive piezoelectric layer, as shown in Fig. 6.3. Since the external electric load can affect the input electric impedance of the thin film BAW resonator, the resonant frequency and effective electromechanical coupling coefficient of the resonator will change with the external load. Thus, the external load could be used as a tuning mechanism for frequency characteristics of the resonators. On the other hand, the use of external electric load also affects the quality factor (Q) of the resonator. For example, as shown in Fig.6.4, when an external resistance (e.g., 2000Ω) is connected to the passive piezoelectric film, the Q factor decreases dramatically because of the increase of the dissipation of the resonator. Fig. 6.5 shows the corresponding phase spectra of the thin film composite resonator. Obviously, the phase spectra also change with the external electric load.

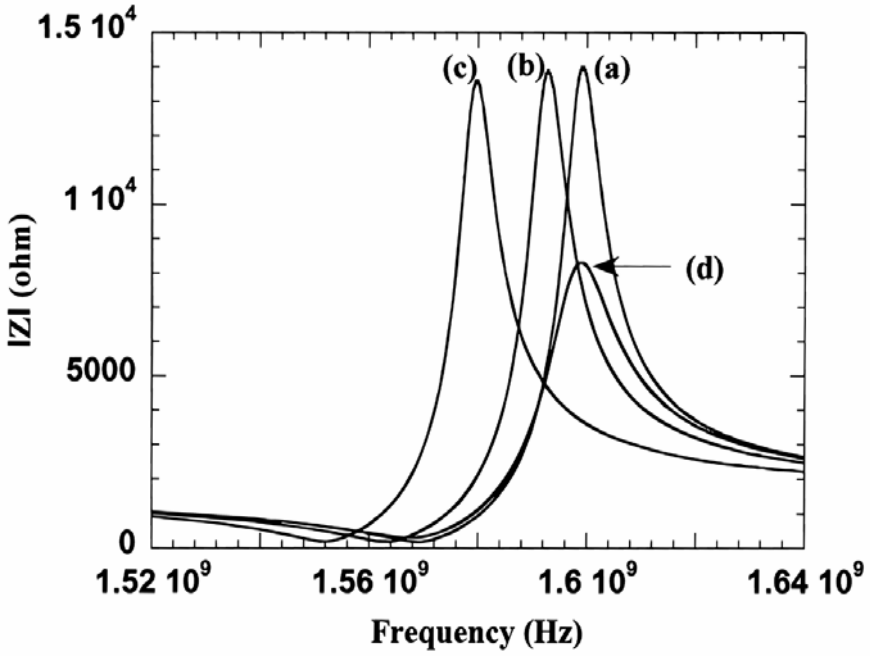

Figure 6.4: The impedance spectra of thin film bulk acoustic wave resonators: (a) no external electric load, (b) external electric capacitance $C=1\times10^{-12}$F, (c) external electric inductance $H=5\times10^{-8}$H, (d) external electric resistance R=2000Ω.

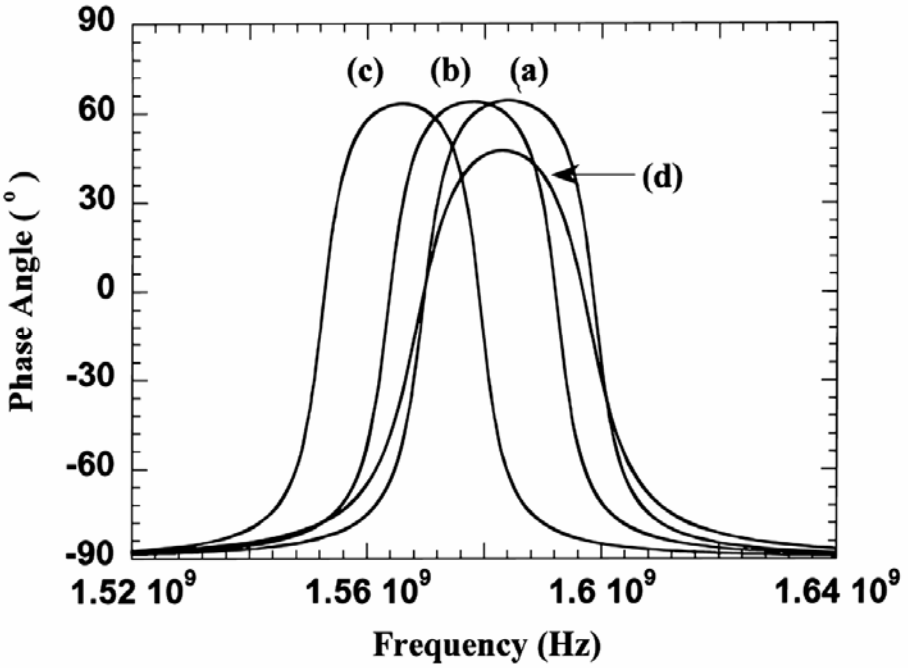

Figure 6.5: The phase angle of AlN thin film bulk acoustic wave resonators (a) no external electric load, (b) external electric capacitance $C=1\times10^{-12}$F, (c) external electric inductance $H=5\times10^{-8}$H, (d) external electric resistance R=2000Ω.

Dielectric materials such as SiO_2 or Si_3N_4 thin films have been used as supporting membrane and barrier layer in the fabrication of thin film acoustic resonators [64, 68]. In the thin film resonator shown in Fig. 6.1, similar to dielectric material SiO_2 or Si_3N_4, passive piezoelectric AlN layer will introduce additional acoustic impedance. Moreover, as a piezoelectric layer it will also introduce clamped electrical capacitance C_{02} and electromechanical coupling (transformer) to the thin film resonator. This passive piezoelectric layer will therefore, affect the effective electromechanical coupling coefficient and mechanical quality factor of the resonator. Fig. 6.6 shows the effective electromechanical coupling coefficient k_{eff}^2 of thin film resonator as a function of the thickness ratio of the passive piezoelectric AlN layer to the active piezoelectric AlN layer, The thickness of the active piezoelectric AlN layer remains 2μm in the calculation.

The k_{eff}^2 decreases with the increase of the passive layer thickness. When the electric port or clamped capacitance C_{01} is not considered, such as in the case of a non-piezoelectric layer is used, the Z_M and Z_E [equations (6.1) and (6.2)] are zero. The capacitance C_{02} can be treated as infinite. While the electric port is considered in the calculation for a passive piezoelectric layer, C_{02} has a finite value. Then the power factor $\cos\theta$ (θ is the phase angle between the current and the voltage across the composite resonator) is increased; therefore, the effective electromechanical coupling coefficient of the resonator is higher when the electric port of the passive piezoelectric AlN film is taken into account.

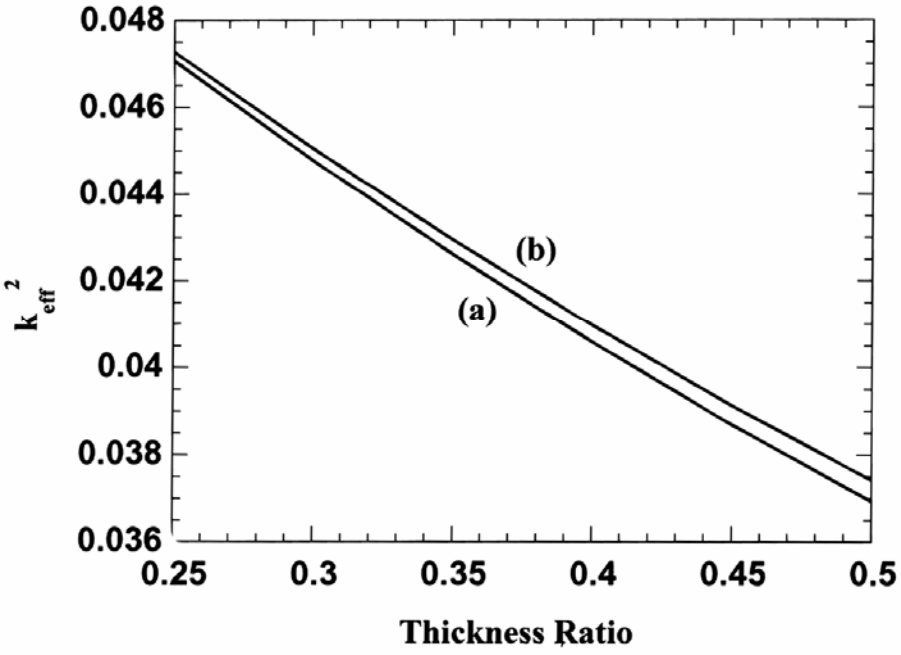

Figure 6.6: The effective electromechanical coupling coefficient k_{eff}^2 changes with the thickness ratio of passive AlN layer to active AlN layer: (a) electric port of the passive layer is not considered; (b) electric port of the passive layer is considered.

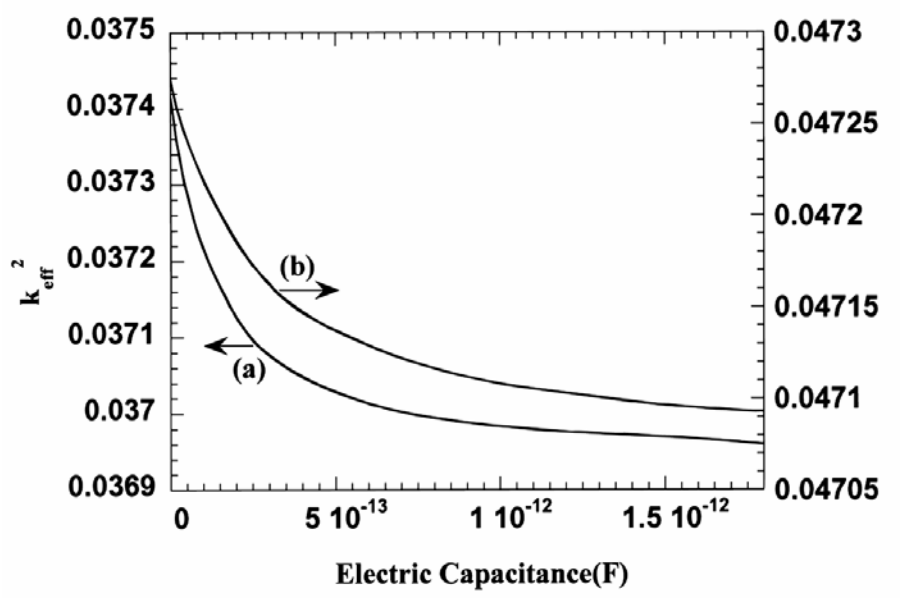

Figure 6.7: The effective electromechanical coupling coefficient k_{eff}^2 changes with the external electric capacitance: (a) thickness of the passive AlN layer is 1μm; (b) thickness of the passive AlN layer is 0.5μm.

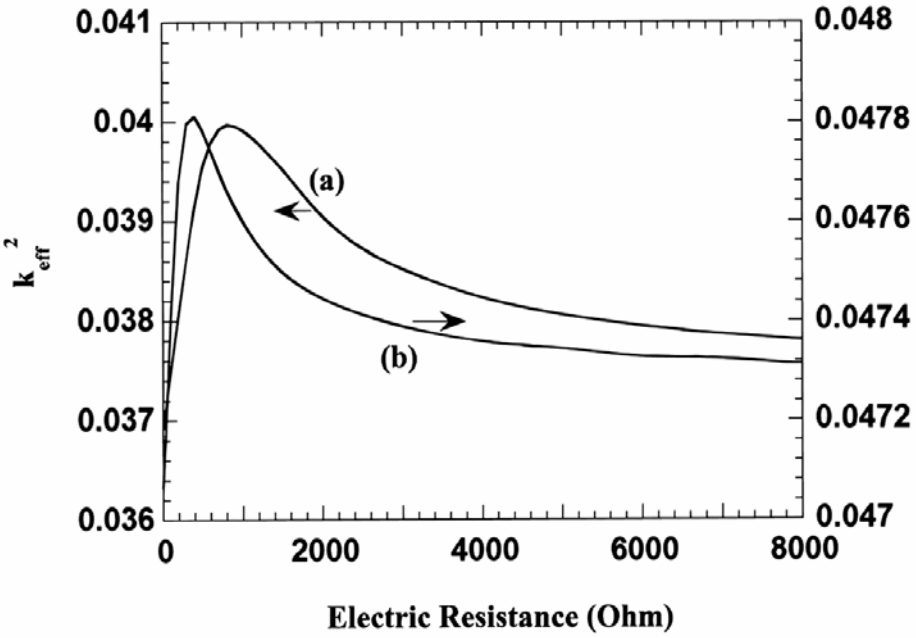

Figure 6.8: The effective electromechanical coupling coefficient k_{eff}^2 changes with the external electric resistance: (a) thickness of the passive AlN layer is 1μm; (b) thickness of the passive AlN layer is 0.5μm.

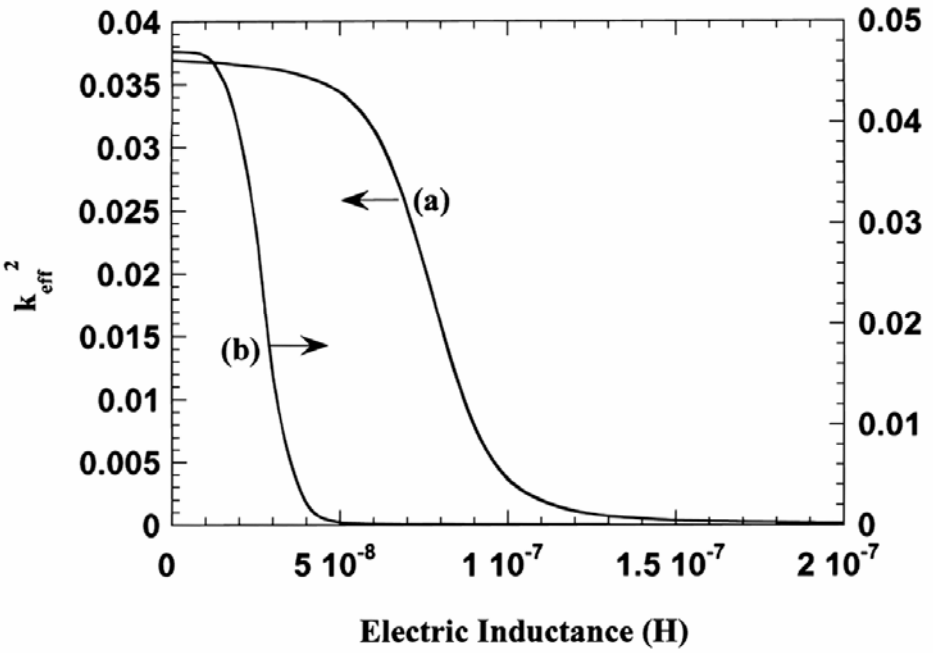

Figure 6.9: The effective electromechanical coupling coefficient k_{eff}^2 changes with the external electric inductance: (a) thickness of the passive AlN layer is 1μm; (b) thickness of the passive AlN layer is 0.5μm.

Figs. 6.7-6.9 show the effective electromechanical coupling coefficient k_{eff}^2 as a function of the external electric impedance including capacitance, resistance and inductance, respectively. Without any external electric load, the thin film piezoelectric resonator is capacitive at low frequency. The impedance changes from capacitive to inductive at the series resonant frequency, and the phase angle changes from -90^o to a positive value (90^o when loss is zero). At the parallel resonant frequency, the phase angle changes from positive to negative, and the device becomes capacitive again. When an external electric capacitance is connected to the passive layer in the resonator structure, the resonator becomes more capacitive. The effective electromechanical coupling coefficient of the resonator will decrease with external capacitance. When the external electric load is electric resistance and inductance, the relationship between the effective

electromechanical coupling coefficient and the external load is quite complicated. For a specific external resistance, the phase angle between the current and the voltage can have a smallest value; therefore the power factor has a highest value. Thus a peak k_{eff}^2 can occur at a certain external electric resistance. When the external load is the electric inductance, the k_{eff}^2 decreases with the increase of the external electric inductance, and the series resonance frequency and parallel resonance frequency decrease dramatically when the inductance reaches a specific range which lead to a dramatically drop of the k_{eff}^2.

The simulation results indicate that, when the passive layer is connected to the external electric resistance, capacitance and inductance, the resonance frequency and the electric factor Q of the resonator will change. Therefore resonance frequency can be tuned using the external impedance to connect to passive piezoelectric layer of the resonator in parallel. In addition, the effective electromechanical coupling coefficient can be changed by using the external electric impedance.

6.2 SIO2 THIN FILM LAYER COMPENSATION ON THE RESONANCE FREQUENCY SHIFT

Frequency shift or phase change is common phenomenon in the applications of the electromechanical resonator. Generally, the resonance frequency shift or phase change in resonators is related to the detecting mass, viscosity, flow rate, force, ambient temperature or other physical parameters. Thus, the study of temperature stability has become an important aspect for the frequency control application of the resonator [69-71].

Usually, two ways can be utilized to compensate the resonance frequency shift induced by the change in ambient temperature. One way is to provide an external field such as the DC bias or the external impedance to compensate the shift. The other way is to fabricate a temperature compensation layer into the composite resonator. The compensation layer should have an opposite temperature coefficient of the material properties corresponding to that of the piezoelectric thin film layer. For the four-layer thin film bulk acoustic wave resonator, the SiO_2 thin film can be deposit and used as the substrate layer. Since the SiO_2 has a positive temperature coefficient of elastic constant, it can compensate the thermal drift induced by the property variation of the AlN layer which has a negative temperature coefficient of elastic constant.

The structure of the resonator and the matrix model are shown in Fig. 5.10 and Fig. 5.11. Using the equation (5.29), the impedance of the four-layer composite FBAR can be calculated. And the effective electromechanical coupling coefficient can be analyzed.

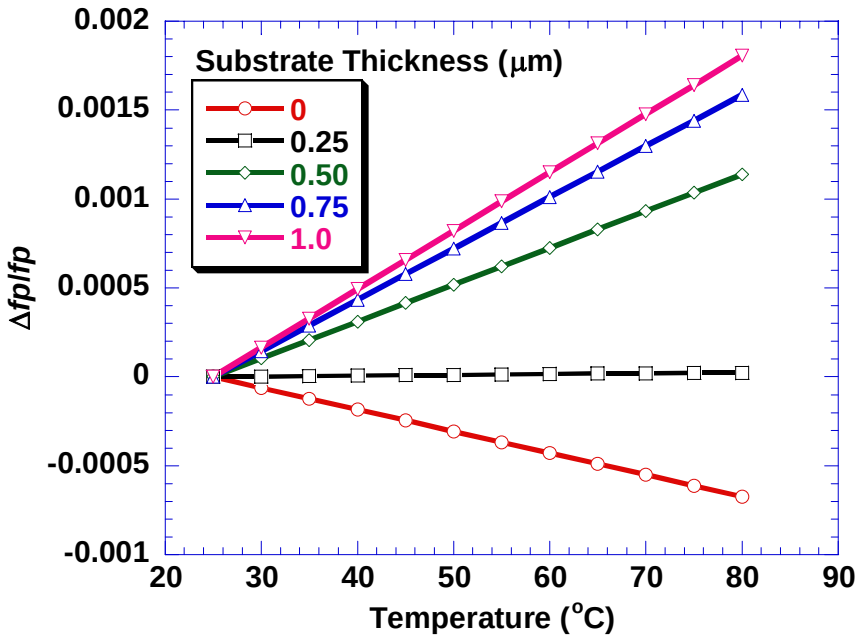

Figure 6.10: The parallel resonance frequency shift of the Al/AlN/Al/SiO_2 resonators induced by the change in ambient temperature for different substrate thickness.

Fig. 6.10 shows the theoretical analyzed results of the parallel resonance frequency shift of the AlN thin film resonators induced by the change in ambient temperature for different substrate thickness. In the calculation, it is assumed that the thickness of AlN layer and Al electrode are 1 μm and 0.1 μm, respectively. It can be seen that by selecting an appropriate thickness of the positive temperature coefficient material for substrate layer, reasonable frequency-temperature stability can be achieved.

The effective coupling coefficient k_{eff}^2 is also temperature dependent for thin film resonators. By simulating the impedance spectra at different temperature, the relationship of k_{eff}^2 verse temperature can be obtained. The results are shown in Fig. 6.11. It can be seen that with the increase of SiO_2 substrate thickness, and ambient temperature, the k_{eff}^2 will increase.

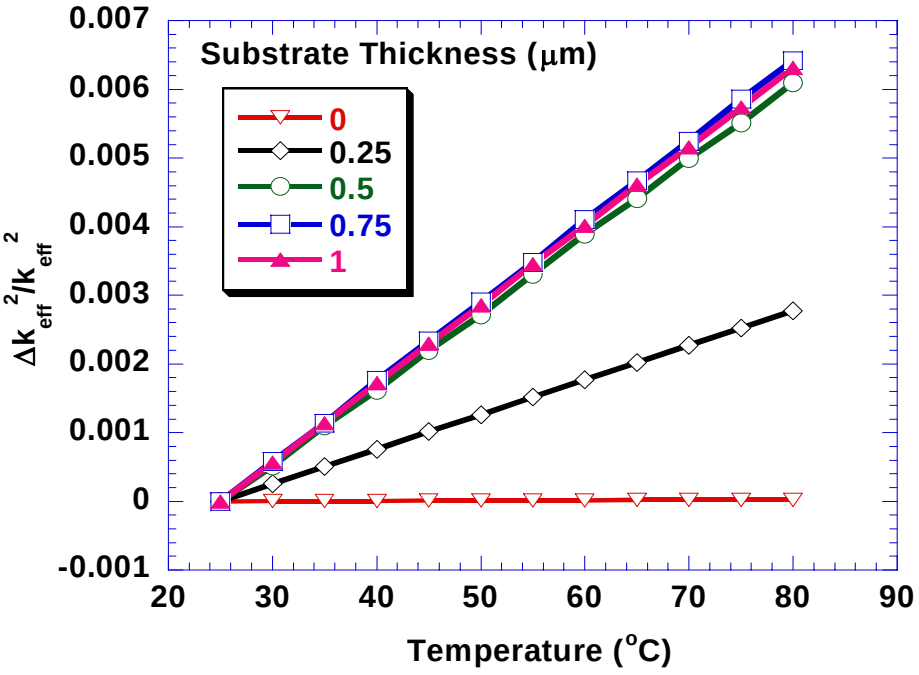

Figure 6.11: The effective coupling coefficient shift of the Al/AlN/Al/SiO_2 four-layer resonators induced by the change in ambient temperature for different substrate thickness.

7.0 CHARACTERIZATION OF THE FOUR-LAYER THIN FILM COMPOSITE BAW RESONATOR

7.1 INTRODUCTION

7.1.1 Scattering parameters

When an electric circuit operates at low frequency range, the dimensions of the elements in the circuit are much smaller than the wavelength and thus the circuit can be treat as the interconnection of lumped elements. The voltage and current are unique at any point in the circuit. Therefore, we can use electric impedance and admittance parameters to describe the circuit network. However, when the operating frequency is up to microwave wave range or higher, the dimensions of the elements are larger than the wavelength. The impedance and admittance are not well defined in such situation. Normalized wave variables (*a* and *b*) are more suitable for the characterization of the circuit at microwave or higher frequencies. The scattering parameters or *S* parameters were used to express the relationship of the normalized wave variables. Unlike other parameters, the *S* parameters relate to the traveling waves that are scattered or reflected when a network is inserted into a transmission line with certain characteristic impedance Z_0.

For a two-port network, there are totally four scattering parameters S_{ij} (i,j=1,2). Each *S* parameter has two subscripts, i and j, where i refers to the port number at which power emerges

and j refers to the port number at which power enters. Thus S_{11} and S_{22} are the reflection coefficients and S_{12} and S_{21} are the transmission coefficients.

For two-port network, the scattering parameters express the relationship of variables a and b through the following matrix equation

$$\begin{bmatrix} b_1 \\ b_2 \end{bmatrix} = \begin{bmatrix} S_{11} & S_{12} \\ S_{21} & S_{22} \end{bmatrix} \begin{bmatrix} a_1 \\ a_2 \end{bmatrix} \tag{7.1}$$

S_{ij} may be obtained by finding the b_i and the incident wave a_j while keeping the other incident wave to be zero. The determination of S_{11} and S_{21} are illustrated in the Fig. 7.1 where DUT means the device under test.

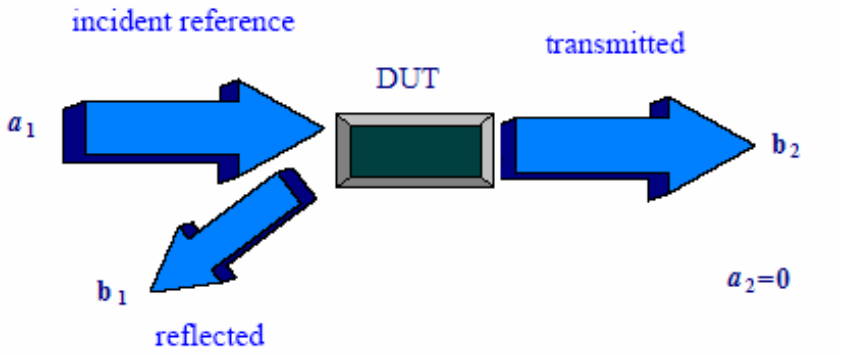

Figure 7.1: Determination of the *S*-parameters for a device under test (DUT).

It can be obtained that

$$S_{11} = \frac{reflected}{incident} = \frac{b_1}{a_1}\bigg|_{a_2 = 0} \tag{7.2}$$

$$S_{21} = \frac{transmitted}{incident} = \frac{b_2}{a_1}\bigg|_{a_2 = 0} \tag{7.3}$$

$$S_{22} = \frac{reflected}{incident} = \frac{b_2}{a_2}\bigg|_{a_1 = 0} \tag{7.4}$$

$$S_{12} = \frac{transmitted}{incident} = \frac{b_1}{a_2}\bigg|_{a_1 = 0} \tag{7.5}$$

In the voltage domain, the *a* and *b* variables have the following definition

$$a_j = \frac{V_{jin}}{\sqrt{Z_0}} = \frac{V_j + Z_0 I_j}{2\sqrt{Z_0}} \tag{7.6}$$

$$b_j = \frac{V_{jout}}{\sqrt{Z_0}} = \frac{V_j - Z_0 I_j}{2\sqrt{Z_0}} \tag{7.7}$$

Where V_j and I_j are the terminal voltage and current at port j, respectively. Z_0 is the system characteristic impedance.

Thus from the equation (7.2), we can get that

$$S_{11} = \frac{V_1 / I_1 - Z_0}{V_1 / I_1 + Z_0} = \frac{Z_1 - Z_0}{Z_1 + Z_0} \tag{7.8}$$

and

$$Z_1 = Z_0 \frac{1 + S_{11}}{1 - S_{11}} \tag{7.9}$$

where Z_1 is the input impedance at port 1. It can be seen that from the S_{11} parameter, we can get the input impedance which can be used to characterize the performance of the BAW resonator and filter.

Scattering parameters are important in microwave design because they are easier to measure and to work with high frequencies than other kinds of two-port parameters. They are analytically convenient and capable of providing detailed insight into a measurement and modeling problem. Moreover, the *S* parameters give a clear and meaningful physical interpretation. This is especially true for power and power gain calculations. The transmission parameters S_{12} and S_{21} are a measure of the complex insertion gain, and the reflection parameters S_{11} and S_{22} are a

measure of the input and output mismatch loss. It should be pointed out that the *S* parameters are linear by default. Thus, they represent the linear behavior of the two-port network.

7.1.2 Vector network analyzer (VNA) and the calibration

Vector network analyzer (VNA) is sophisticated measurement system used for device or network test at RF and microwave frequency range. The key elements of the Vector network analyzer (VNA) are shown in the Fig. 7.2. The RF source at the top provide stimulus to the device under test (DUT). A switch directs the RF energy to either DUT port. The test set uses directional couplers or bridges to pick off the forward and reverse waves traveling to and from each port, and converts these signals to four IF sections. Each IF section filters, amplifies and digitizes the signal for further digital processing and display. A VNA is used to measure the vector ratios of reflected or transmitted energy to incident energy upon the DUT.

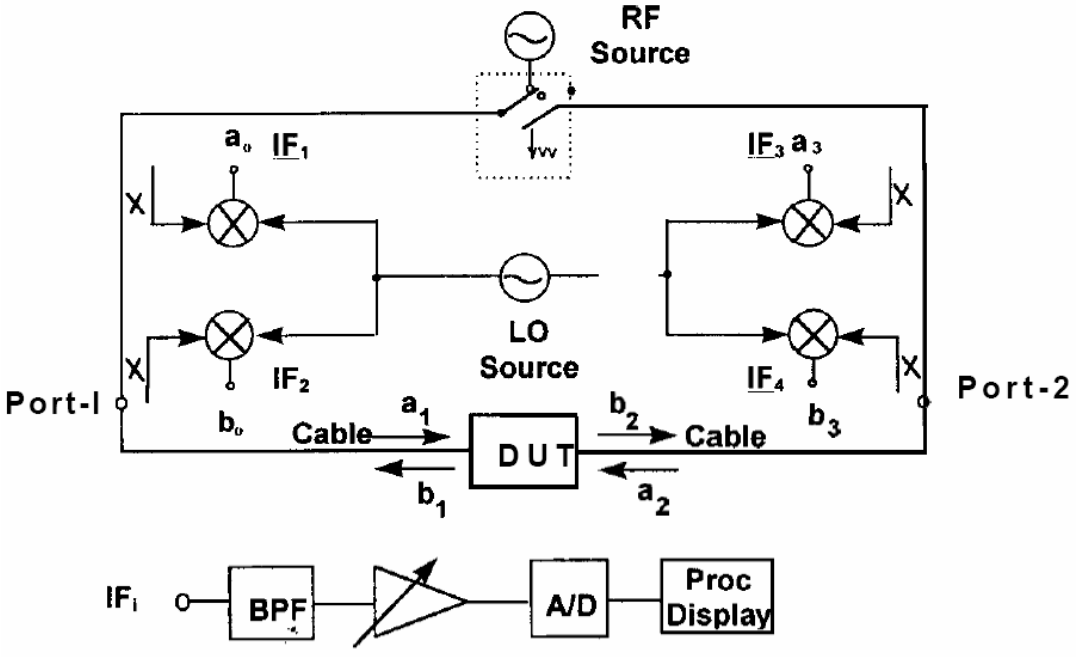

Figure 7.2: Main hardware blocks in a Vector Network Analyzer (VNA). [72]

How to identify exactly where the measurement system ends and the DUT begins is important to the stimulus-response measurement. In VNA measurements this boundary is known as the "reference plane" of the measurement and usually is located at the probe tips. Ideally the system will measure the characteristics of whatever is connected to the measurement reference plane. If we ignore any imperfections of the cables, connectors, mixers, and so forth, then the ratios of wave amplitudes (*a*'s and *b*'s) inside of the machine correspond directly to the DUT's S-parameters.

VNA calibration is the process of measuring devices with known or partly known characteristics and using these measurements to establish the measurement reference planes. Calibration also corrects for the imperfections of the measurement system. These imperfections not only include the non-ideal nature of cables and probes, but also the internal characteristics of the VNA itself. Calibrations account for serious systematic imperfections in the VNA such as impedance mismatch, loss in the cables and connectors, the frequency response of the source and receiver, the transmission between ports, and directivity and cross talk due to signal leakage. However, calibrations do not account for system drift, repeatability in the switches and connectors, instrument noise, or errors in the calibration standards.

There are a wide variety of calibration methods available to VNA users. However, the basic procedure for calibrating a VNA is the same, regardless of what type of calibration is performed. The first step is to measure the known standards. Next, the measured data is processed to determine the error coefficients. And finally, the measured data for a DUT is corrected using the error coefficients. A VNA uses multiple standards, typically open circuit, short circuit, loads, and through connections to perform the calibration.

7.2 RESONANCE SPECTRUM METHOD FOR FOUR-LAYER COMPOSITE RESONATOR

Resonance Spectrum Method is a kind of direct method to characterize the piezoelectric film layer in the composite resonators. With the calculation of the spacing of the parallel resonant frequencies and the effective coupling coefficient k_{eff}^2, the acoustic velocity, the density, and therefore elastic constant of the piezoelectric film can be evaluated directly.

Figure 3.5(a) shows the schematic structure of the composite resonator while taking two electrodes into account.

Using transfer matrix approach, we can get the impedance of the above four layer composite resonator as following

$$Z_{in} = \frac{1}{j\omega C_0}\left[1 - \frac{k_t^2}{\gamma}\frac{(z_1 + z_2)\sin\gamma + j2(1-\cos\gamma)}{(z_1 + z_2)\cos\gamma + j(1+z_1 z_2)\sin\gamma}\right] \tag{7.10}$$

The parameters in the equations in this chapter have been identified in chapter 5.

7.2.1 The first normal region

The parallel resonance frequencies of a composite resonator correspond to the maximum resistance. By setting the denominator of equation (7.10) to zero, we can get the determination equation for the parallel resonance frequencies.

$$(z_1 + z_2)\cos\gamma + j(1 + z_1 z_2)\sin\gamma = 0 \tag{7.11}$$

The normal regions are the areas where γ is close to an integral multiple of π. The first normal region is where $\gamma \approx \pi$. Assuming the electrodes are much thinner than the piezoelectric film, then at the center of the first normal region, we can set

$$\gamma = \pi + \varepsilon \tag{7.12}$$

$$\gamma_{sb} = m_N \cdot \pi + \delta \tag{7.13}$$

where m_N is the mode order of the bare substrate layer resonator at the center of the first normal region. From equations (5.24) and (5.28) and ignoring the second order small quantity, we can get

$$z_1 = \frac{Z_1}{Z_0} \approx j \cdot z_{e1} \cdot \gamma_{e1} \tag{7.14}$$

$$z_2 = \frac{Z_2}{Z_0} \approx j \cdot \left(z_{sb} \cdot \delta + z_{e2} \cdot \gamma_{e2} \right) \tag{7.15}$$

From equations (7.11) to (7.15), we can get the m_N+1 order parallel resonance frequency of the four layer composite resonator as,

$$f_p(m_N + 1) = \frac{1}{2} \frac{(m_N z_{sb} + 1)}{\frac{z_{e1} d_{e1}}{v_{e1}} + \frac{z_{e2} d_{e2}}{v_{e2}} + \frac{z_{sb} d_{sb}}{v_{sb}} + \frac{d}{v}} \tag{7.16}$$

So the spacing of two parallel resonant frequencies (Δf_p) in the first normal region is

$$\Delta f_N = \frac{1}{2} \frac{\rho_{sb} v_{sb}}{\rho_{e1} d_{e1} + \rho_{sb} d_{sb} + \rho_{e2} d_{e2} + \rho d} \tag{7.17}$$

Therefore, the density of the piezoelectric film is

$$\rho = \left(\frac{v_{sb} \rho_{sb}}{2 \Delta f_N} - \rho_{sb} d_{sb} - \rho_{e1} d_{e1} - \rho_{e2} d_{e2} \right) \Big/ d \tag{7.18}$$

7.2.2 The first transition region

The first transition region is the area where $\gamma \approx \pi/2$. We can set

$$\gamma = \pi/2 + \varepsilon' \tag{7.19}$$

$$\gamma_{sb} = (m_T + 1/2) \cdot \pi + \delta' \tag{7.20}$$

where m_T is the mode order of the bare substrate layer resonator near the center of the first transition region.

Then

$$z_2 = \frac{j}{Z_0}\frac{Z_{sb}\tan\gamma_{sb} + Z_{e2}\tan\gamma_{e2}}{1-(Z_{sb}/Z_{e2})\tan\gamma_{sb}\tan\gamma_{e2}} \approx -j\cdot\left(\frac{\delta'}{z_{sb}} + \frac{\gamma_{e2}}{z_{e2}}\right)^{-1} \tag{7.21}$$

Substituting the approximations of equations (7.14), (7.19), (7.20) and (7.21) into equation (7.11). We can get the parallel resonance frequencies in the first transition region.

$$f_p = \frac{1}{2z_{sb}}\frac{m_T + 1/2 + z_{sb}/2}{\frac{z_{e1}d_{e1}}{v_{e1}} + \frac{d_{e2}}{z_{e2}v_{e2}} + \frac{d_{sb}}{z_{sb}v_{sb}} + \frac{d}{v}} \tag{7.22}$$

Δf_p in the first transition region is

$$\Delta f_T = \frac{1}{2z_{sb}}\frac{1}{\frac{z_{e1}d_{e1}}{v_{e1}} + \frac{d_{e2}}{z_{e2}v_{e2}} + \frac{d_{sb}}{z_{sb}v_{sb}} + \frac{d}{v}}$$

$$= \frac{v_{sb}}{2d_{sb}}\left(1 + \frac{\rho_{sb}v_{sb}^2 d}{\rho v^2 d_{sb}} + \frac{\rho_{sb}v_{sb}^2 d_{e2}}{\rho_{e2}v_{e2}^2 d_{sb}} + \frac{\rho_{sb}\rho_{e1}v_{sb}^2 d_{e1}}{\rho^2 v^2 d_{sb}}\right)^{-1} \tag{7.23}$$

Therefore, the acoustic velocity of the piezoelectric layer is

$$v = \sqrt{\left(\frac{\rho_{sb}v_{sb}^2 d}{\rho d_{sb}} + \frac{\rho_{sb}\rho_{e1}v_{sb}^2 d_{e1}}{\rho^2 d_{sb}}\right) \Big/ \left(\frac{v_{sb}}{2d_{sb}\Delta f_T} - 1 - \frac{\rho_{sb}v_{sb}^2 d_{e2}}{\rho_{e2}v_{e2}^2 d_{sb}}\right)}' \tag{7.24}$$

The density and the acoustic velocity of the AlN thin film can be calculated by the equations (7.18) and (7.24), and thus the stiffened elastic constant of the film can be calculated,

$$c^D = v^2\rho \tag{7.25}$$

7.3 FOUR-LAYER COMPOSITE RESONATOR SAMPLE AND EXPERIMENT SETUP

7.3.1 Four-layer composite resonator sample

The four-layer resonator sample is composed of the AlN thin film sandwiched by the Al top electrode and Pt bottom electrode with the double side polished Si substrate. The schematic drawing of the resonator structure is show in Fig 3.5. The thickness of the AlN thin film and the Si substrate is 1.9μm and 100μm, respectively. The square bottom electrode has a thickness and area of around 80 nm and 0.64mm^2 respectively, where the titanium buffer layer is very thin and thus the platinum layer determines the bottom electrode property. The square Al top electrode has a thickness and area of around 1.05μm and 1mm^2 respectively. All the thin film is deposited by the DC reactive magnetron sputtering method.

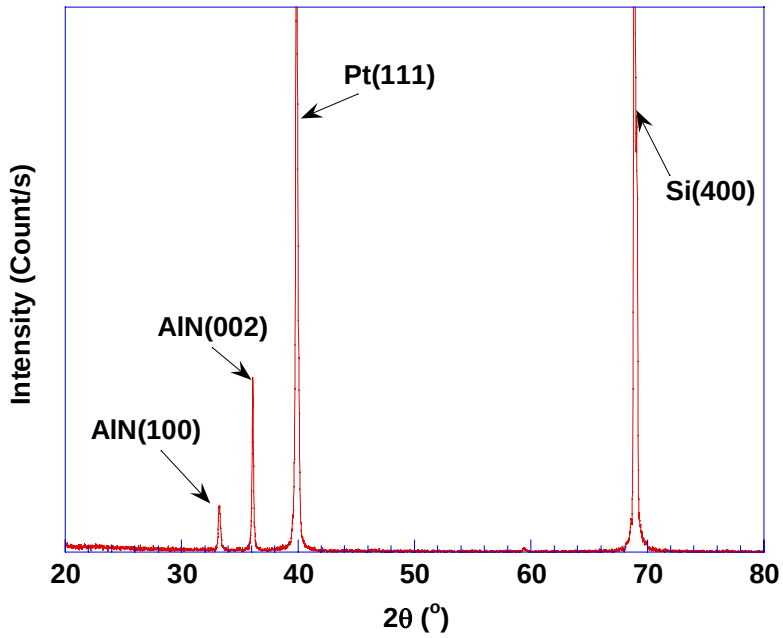

Figure 7.3: XRD of the AlN thin film.

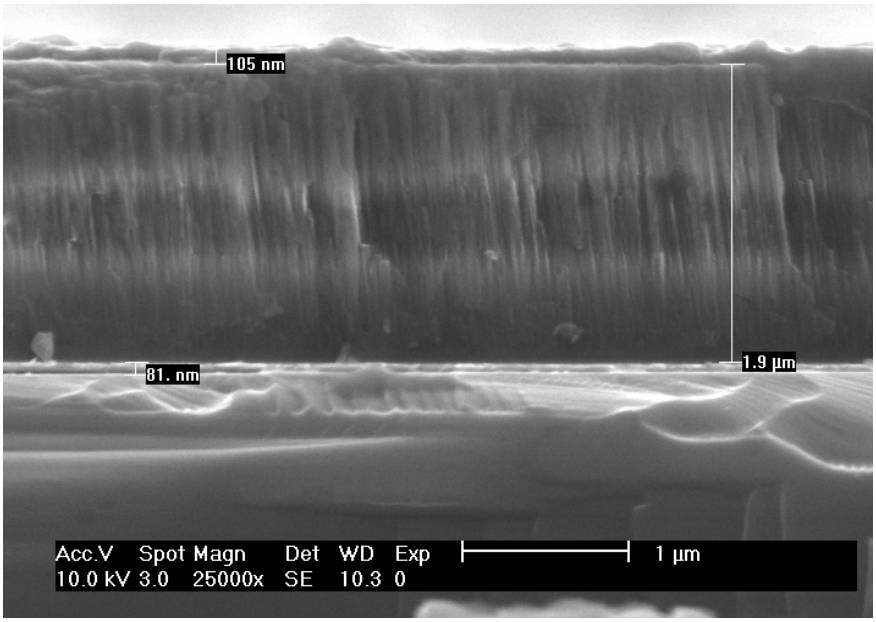

Figure 7.4: SEM image of AlN film deposited at 450^{o}C on silicon (100) substrate.

Fig. 7.3 and Fig.7.4 show the XRD and SEM images of the AlN four-layer composite resonator. Since the AlN film was deposited in 450^{o}C, the AlN (100) peak appears in the XRD analysis result. The column grain of the AlN is also not exactly perpendicular to the surface of the Si substrate.

7.3.2 The measurement setup and calibration

The composite resonator was measured on the Cascade probe station (Cascade Summit 9000, Cascade Micro Tech, Oregon, USA). The microscope of the probe station is used to assist the alignment of the SG probe to the impedance standard substrate (ISS) and the device under test (e.g., FBAR). The sample was placed on the moveable probe station substrate which contacted the edges of the bottom surface of the sample so that the resonator could vibrate with free boundary condition in the thickness direction. A proper SG probe shown in Fig. 7.5, which has two pins on the tip, was used to contact the electrodes of the composite resonator electrically.

The other end of the probe was connected to the network analyzer through a RF cable. The schematic measurement setup is shown in Fig. 7.6.

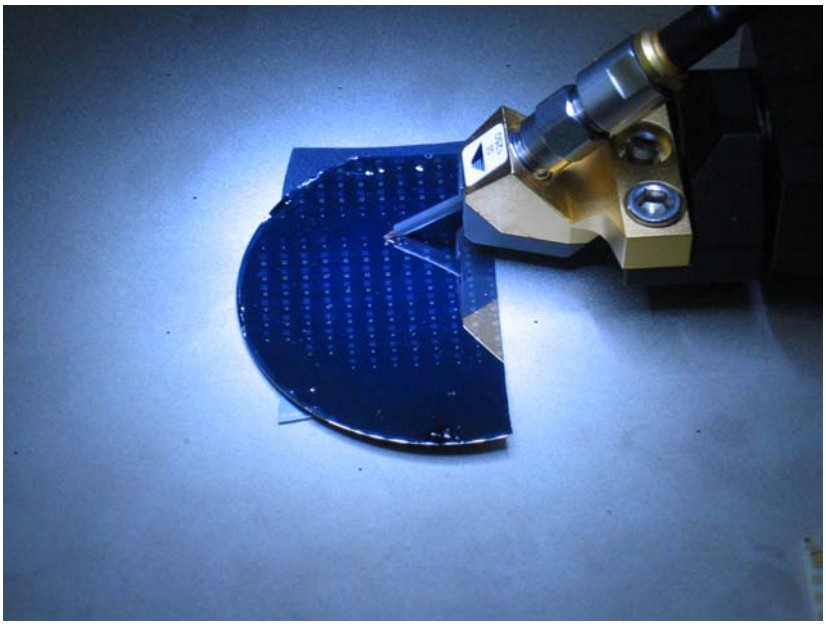

Figure 7.5: The SG probe on the samples.

Before the measurement, the calibration was implemented by applying standard impedance at the tip of the SG probe. Therefore, some imperfection of the VNA system will be calibrated out. In order to measure the S_{11} parameters of the sample, the open-short-load VNA calibrations steps were performed. Fig. 7.7 shows the impedance standard substrate for the calibration where (a), (b), and (c) represents the open, short and 50Ω standard impedance.

The reflection scattering parameter S_{11} was measured from 400MHz to 2500MHz. The entire frequency span of 2100MHz was divided to tens of narrow sub-spans to achieve higher resolution in the measurement of the resonance spectrum.

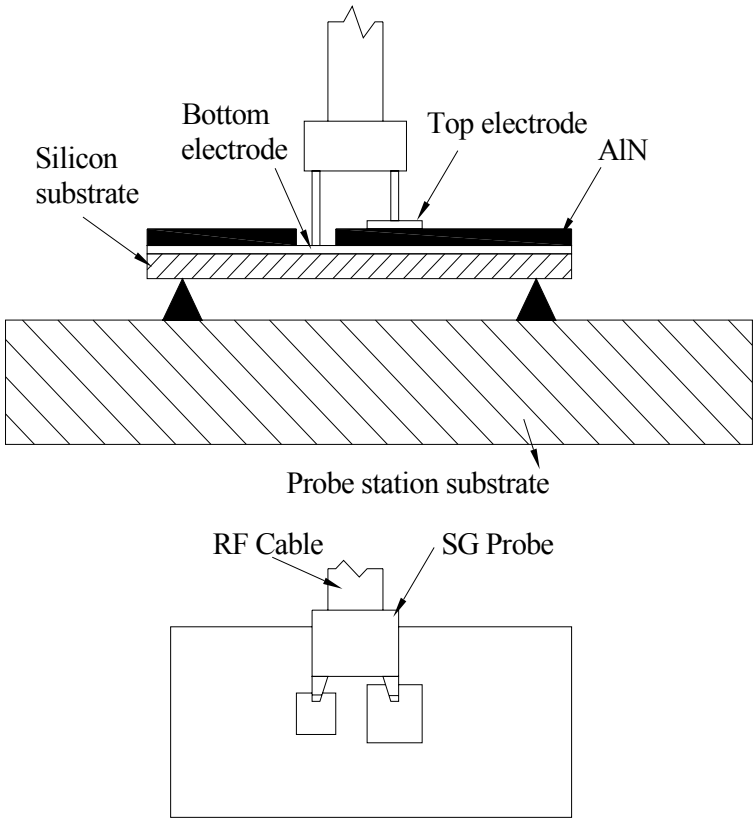

Figure 7.6: The measurement setup.

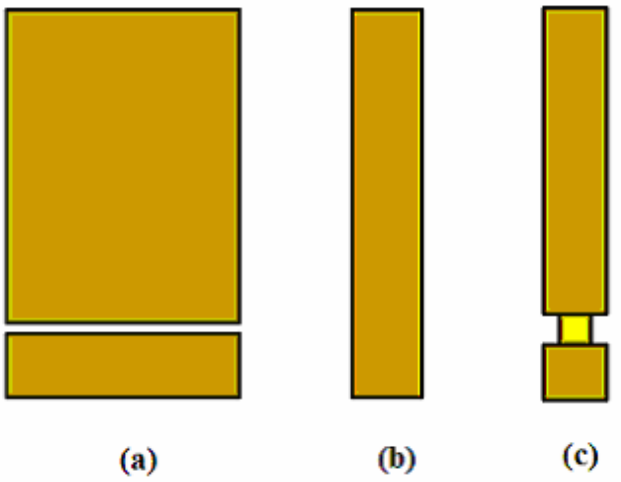

Figure 7.7: Impedance Standard Substrate map for SG probe.

7.4 EXPERIMENT RESULTS AND DISCUSSION

First, we use the equation (7.1) to get the simulated impedance spectrum of the four-layer AlN composite resonator. Fig. 7.8 shows the simulation result. It can be seen that the multiple sharp peaks or the resonance modes appear in the spectrum of the composite resonator due the thick substrate existence. Table 7.1 lists the material properties used in the simulation. It should be mentioned that small imaginary parts of the acoustic velocities of the materials, which stand for the mechanical loss, have been introduced in the calculation. The mechanical Q in the table represents half of the real part to imaginary part ratio of the acoustic velocity. Fig. 7.9 and Fig. 7.10 show the S_{11} and converted impedance spectrum with three consecutive peaks. By detecting the parallel resonance frequency of these modes, we can obtain the space of two adjacent parallel resonance frequencies Δf_P over the detecting frequency range.

Table 7.1: Material properties of the four-layer composite resonators

	Density (kg/m^3)	Acoustic Velocity(m/s)	k_t^2 (%)	Thickness (μm)	Area (m^2)	Q	ε_r
AlN	3300	11000	6.25	1.9	2.5×10^{-9}	500	8.5
Al	2700	6418	N/A	1.05	2.5×10^{-9}	2000	N/A
Pt	21450	2823	N/A	0.8	2.5×10^{-9}	500	N/A
Si	2320	8265	N/A	100	2.5×10^{-9}	3000	N/A

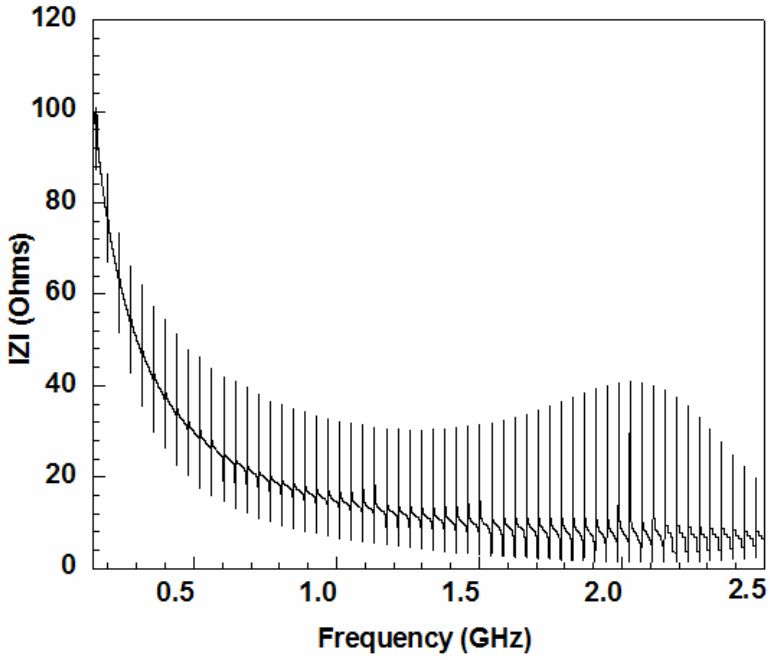

Figure 7.8: Simulated impedance spectrum of the four-layer AlN thin film composite resonator.

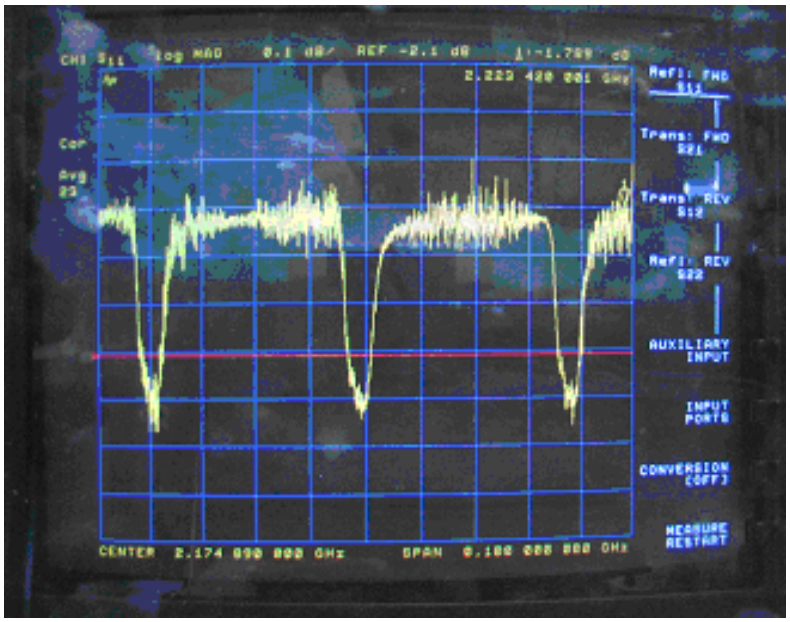

Figure 7.9: Measured S_{11} parameter of the four-layer composite resonator.

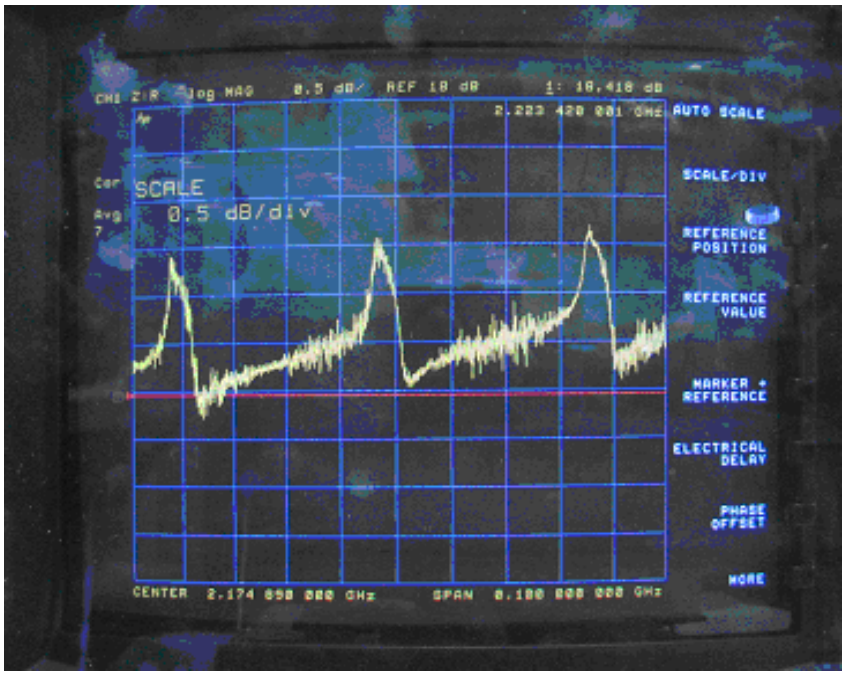

Figure 7.10: Measured impedance of the four-layer composite resonator.

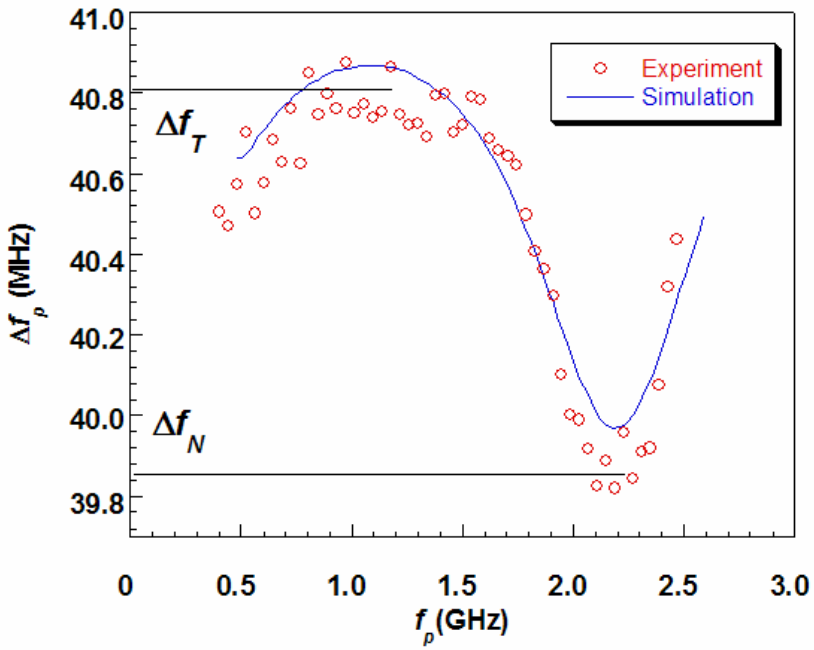

Figure 7.11: Space of the parallel resonance frequency as the function of parallel resonance frequency.

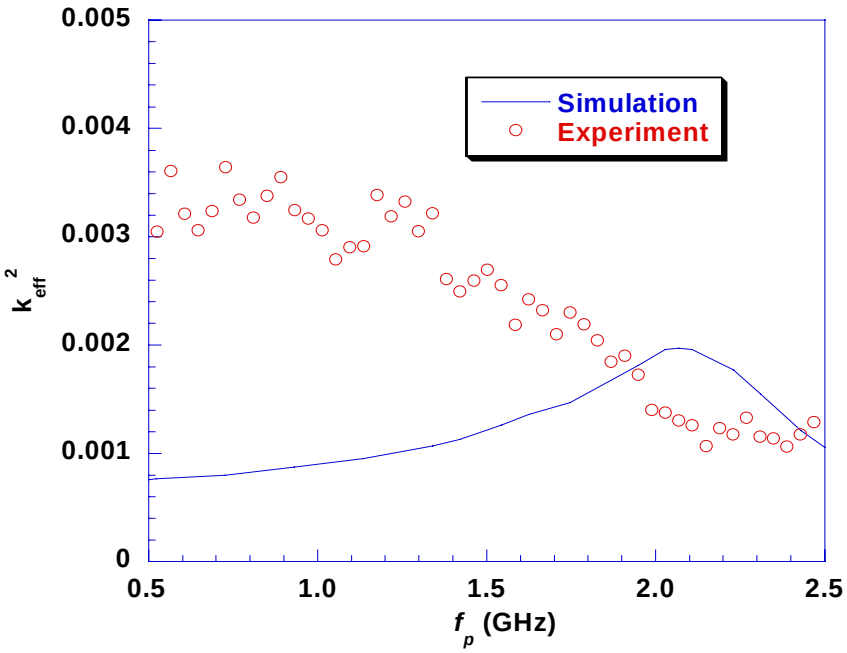

Figure 7.12: Effective electromechanical coupling coefficient as the function of parallel resonance frequency.

Fig. 7.11 shows the experiment results and the simulation results of space of the parallel resonance frequency Δf_P as the function of parallel resonance frequency. Although the experimental data is a little dispersive, the periodic shape of the curve is in good agreement with the simulation results. By averaging the measurement data around the center of the first normal and transition region, respectively, we can obtain the values of the Δf_T and Δf_N are 40.81MHz and 39.86MHz, respectively.

Using the equations (7.18) and (7.24), the density and acoustic velocity of the AlN thin film can be calculated with values of 3187.3kg/m^3 and 10631m/s, respectively. Comparing the experiment value with the value list in the Table 7.1, the difference is less than 5%.

From equation (7.25), the elastic constant of the AlN thin film is obtained with value of 341.2GPa which is in good agreement with the value reported. [73, 74]

From the equation (5.10), effective electromechanical coupling coefficient k_{eff}^2 can be calculated. Fig 7.12 shows the experiment results and the simulation results of k_{eff}^2 as the function of the parallel resonance frequency. It can be seen that the experimental data is dispersive. However, the experiment data and the simulation values are at the same order of magnitude. The experiment results show that the four-layer composite resonator with resonance frequency up to 2.5 GHz has been fabricated and the effective electromechanical coupling coefficient k_{eff}^2 is 0.001-0.004.

8.0 CONCLUSIONS AND FUTURE WORK

In this dissertation, we have made several contributions to the fabrication and characterization of the on-chip thin film bulk acoustic wave resonator. Experimental study has been conducted to fabricate and characterize the AlN thin films and the FBARs. Theoretical study also has been conducted to design, optimize and characterize these acoustic devices.

8.1 MAJOR ACCOMPLISHMENTS

The major accomplishments of this research are list below:

- The highly c-axis orientation piezoelectric AlN thin films are deposited on the silicon (100) and sapphire (002) substrate by using the DC reactive magnetron sputtering method. The crystal structures of the AlN thin films are characterized by using the XRD and SEM method.
- The effects of the deposition parameters including the discharge power, substrate temperature, deposition pressure, gas flow ratio, and the distance between target and substrate on the orientation of the thin film are investigated.
- The surface roughness and morphology of the AlN thin films are characterized by using the AFM and SEM method.
- The membrane type FBAR and four-layer thin film composite resonator with different substrate are fabricated. AlN and Al thin films and the silicon substrate are etched by using the

appropriate wet etchant or dry etching method. The MEMS techniques including the photolithography are utilized to fabricate the micro acoustic devices.

- The hardness and reduced elastic constant of the AlN thin film in the AlN/Pt/Ti/sapphire four-layer composite structure are measured by nano-indentation method. The experiments show that the average hardness is 18GPa. By considering the effect the diamond tip, the average elastic constant is 307GPa.

- The effective piezoelectric coefficient d_{33eff} of the AlN thin film in the AlN/Pt/Ti/sapphire four-layer composite structure is measured by the single beam laser interferometer. By considering the clamping effect of the substrate on the thin film, the truly piezoelectric coefficient d_{33} is 4.17pm/V.

- The theoretical method based on the mason model is developed to characterize the input impedance of the multiplayer FBAR. Based on the impedance spectrum, the effective electromechanical coupling coefficient k_{eff}^2 of the device can be studied.

- For three-layer resonator structure, effective coupling coefficients as the function of mechanical Q and electrode thickness for different electrodes Au and Al are simulated respectively.

- For four-layer resonator structure, effective coupling coefficients as the function of thickness of different support layers and different electrodes Au and Al are simulated respectively.

- The introduction of the passive layer and external impedance and the incorporation of the SiO_2 support layer with positive temperature coefficient of elastic constant to the FBAR resonator structure to control and tune the resonance frequency are studied by using the theoretical model.

- The scattering parameters S_{11} of the four-layer thin film composite BAW resonator are measured by the vector network analyzer. The converted impedance spectrum of the resonator is obtained. The resonance frequencies from 500 MHz to 2500 MHz have been detected.
- Using the resonance spectrum method, the density and the elastic constant of the AlN thin film are calculated which are 3187.3kg/m^3 and 10631m/s, respectively. Comparing the experiment values with the values list in the simulation, the difference is less than 5%. The effective electromechanical coupling coefficient k_{eff}^2 is 0.001-0.004 for the four-layer thin film composite resonator.

In this study, the impedance modeling for the multi-layer thin film resonator can be used to direct the design of the FBAR to get the optimal operation quality. And the composite resonator experimental method also provides a technique to precisely obtain some important material properties of the piezoelectric thin film.

8.2 FUTURE WORK

The membrane type FBARs have been fabricated and modeled by the theoretical model. More experiment should be conducted to measure the scattering parameters S_{11} and S_{12}. Then we can get some important performance parameters such as the effective electromechanical coupling coefficient and quality factor Q of the devices. These values are very useful for the design of the RF filters.

As discussed before, the AlN thin film resonator is temperature dependence of the resonance frequency. Therefore, resonators for use in oscillator and filters need a degree of temperature compensation. Since the temperature coefficients of AlN used in the thin film resonator is about –25ppm/^{o}C, one temperature compensation approach is to use a composite structure with

positive TC materials such as SiO_2 (+85ppm/^oC) to obtain satisfactory degree of temperature compensation. The SiO_2 with a few different thicknesses can be incorporated in the FBAR structure and the resonance frequency dependence can be measured experimentally.

In addition, an alternative approach can be studied for the on-chip resonator fabrication, in which the epitaxial films or heterostructure are first grown on a suitable single crystal substrate (such as sapphire) followed by laser lift-off and transfer of the epitaxial films to the receptor substrate (such as silicon). Then a wafer bonding processing is applied to realize the on-chip integration. The processing steps for the on-chip resonator fabrication are shown in Fig. 8.1. In the processing, excimer laser radiation of 3.49eV (355nm) used for the lift-off of GaN films is just above the absorption edge of GaN, and absorption yields metallic Ga and N_2 gas as decomposition products. It should be noted that the transfer of the thin film elements to silicon substrate by the laser lift-off process can be accomplished with the aid of Pd-In transient –liquid-phase bonding process.

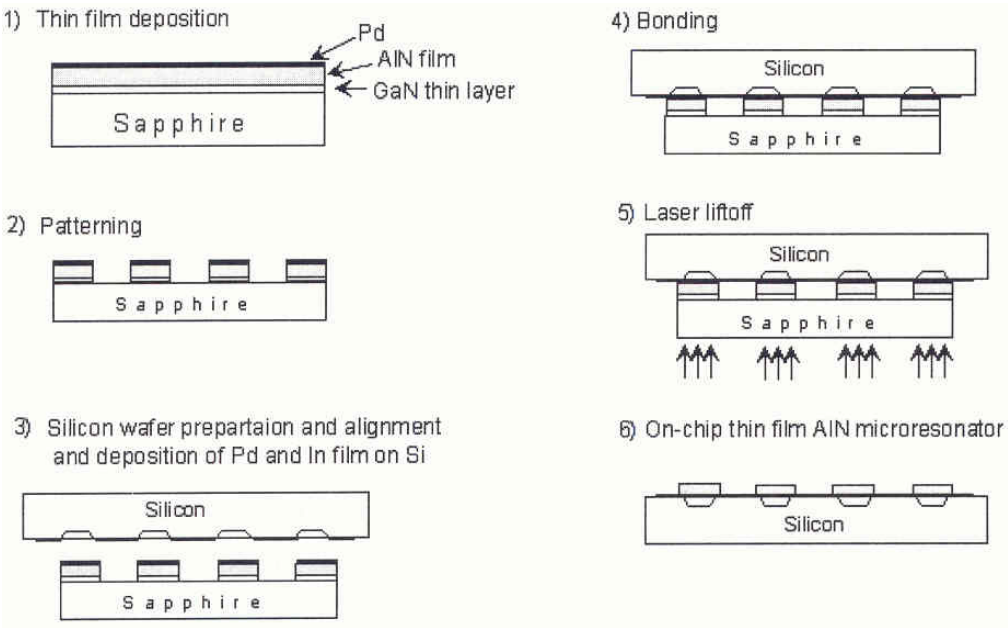

Figure 8.1: Processing steps for on-chip AlN FBAR fabrication and integration.

Using the laser lift-off and transfer method, the single crystal piezoelectric materials such as AlN thin film can be grown on any substrate including metals, semiconductors and polymers. Since the single crystal materials have better electromechanical properties than the ceramic materials or multi-crystal materials, the devices made by these materials should have better performance capability.

BIBLIOGRAPHY

1. M. Elwenspoek, R. Wiegerink, Mechanical Microsensors, Springer-Verlag, (2001).

2. Tai-Ran Hsu, MEMS & Microsystems: Design and Manufacture, McGraw-Hill, (2002).

3. Shigeo M. Tanaka, A new mechanical stimulator for cultured bone cells using piezoelectric actuator, Journal of Biomechanics, Vol.32, pp. 427-430, 1999.

4. C. Zhang, J. F. Vetelino, Chemical sensors based on electrically sensitive quartz resonators, Sensors and Actuators B, Vol. 91, pp. 320-325, 2003.

5. Wan Y. Shih, Simultaneous liquid viscosity and density determination with piezoelectric unimorph cantilevers, Journal of Applied Physics, Vol. 89, pp. 1497-1505, 2001.

6. Erik Stemme, Göran Stemme, A balanced resonant pressure sensor, Sensors and Actuators A, Vol. 21, pp. 336-341, 1990.

7. E. Benes, M. Gröschl, Sensors based on piezoelectric resonators, Sensors and Actuators A, Vol. 48, pp. 1-21, 1995.

8. K. M. Lakin, Thin film resonators and filters. IEEE Ultrasonic Symposium, pp. 895–906, 2001.

9. Bolaji Omolaja Olutade, Thin Film ZnO-based Resonators for Integrated Wireless Applications, PhD thesis, Department of Electrical Engineering, Georgia Institute of Technology, USA. 1998.

10. Campbell, C., Surface Acoustic Wave Devices for Mobile and Wireless Communications, San Diego: Academic Press, 1998.

11. B. Drafts, Acoustic wave technology sensors, IEEE Transactions on Microwave Theory and Techniques, Vol. 49, pp. 795-802, 2001.

12. R. Ruby and P. Merchant, Micromachined thin film bulk acoustic resonators, 1994 IEEE International Frequency Control Symposium, pp. 135-138, 1994.

13. Lakin, K.M., A review of thin-film resonator technology, Microwave Magazine, *IEEE*, Vol.4, pp. 61-67, 2003.

14. K.M. Lakin, G.R. Kline, and K.T. McCarron, Development of miniature filters for wireless applications, IEEE MTT-S Digest, pp. 95-101, 2001.

15. K.M. Lakin, G.R. Kline, and K.T. McCarron, High Q microwave acoustic resonators and filters", IEEE MTT-S Digest, pp. 1517-1520, 1993.

16. C. W. Seabury, J. T. Cheung, P.H. Kobrin, R. Addison, and D. P. Havens, High performance microwave air-bridge resonators, Proc. IEEE Ultrasonics Symposium, pp. 909-911, 1995

17. Kun-Wook Kim, Gwang-Yong Kim, Jong-Gwan Yook, and Han-Kyu Park, Air-gap-type TFBAR-based filter topologies, Microwave and optical technology letters, Vol. 34, pp. 386-387, 2003

18. Feng Zhong, Development of Aluminum Nitride Thin Films For Applications In Acoustic Wave (AW) Sensors, Ph. D. Thesis, Department of Electrical Engineering, Wayne State University, USA, 2001.

19. J. F. Rosenbaum, Bulk Acoustic Waves Theory and Devices, Artech House, 1988.

20. Nadim Maluf, An Introduction to Microelectromechanical Systems Engineering , Artech House, INC. ,2000.

21. Larson Philip H., The Use of Piezoelectric Material in Creating Adaptive Shell Structures, Ph. D. thesis, department of mechanical engineering, University of Delaware, USA, 1994.

22. X. D. Bai et al, Dual-mode mechanical resonance of individual ZnO nanobelts, Applied Physics Letters, Vol. 82, pp. 4806-4808, 2005.

23. William L. Hughes et al. Nanobelts as nanocantilevers, Applied Physics Letters, Vol. 82, pp. 2886-2888, 2003.

24. Q. Wan, et al, Fabrication and ethanol sensing characteristics of ZnO nanowire gas sensors, Applied Physics Letters, Vol. 84, pp. 3654-3656, 2004.

25. Been-Yu Liaw, Diamond and Aluminum Nitride Thin Films: Synthesis, Properties, and Some Device Application, PH. D. thesis, Department of Electrical Engineering, University of Missouri-Columbia, USA, 1995.

26. W. M. Yim and R. J. Paff, Thermal expansion of AlN, sapphire, and silicon, Journal of Applied Physics, Vol. 45, pp. 1456-57, 1974

27. Guanghai Zhang, Nanoscale and Macroscale Aluminum Nitride Deposition Via Reactive Magnetron Sputtering Method, Ph. D. thesis, University of Akron, USA, 2004.

28. G.F. Iriarte, AlN Thin film electroacoustic devices, Comprehensive Summaries of Uppsala Dissertations from the Faculty of Science and Technology. 817

29. P.M Martin, Piezoelectric films for 100-MHz ultrasonic transducers, Thin Solid Films, Vol. 379, pp. 253-258, 2000.

30. Milton Ohring, The Materials Science of Thin Films, Academic Press, Inc. (1992)

31. Nadim Maluf, An Introduction to Microelectromechanical Systems Engineering , Artech House, INC., 2000.

32. H. Itoh, M. Kato, K. Sugiyama, Plasma-enhanced chemical vapour deposition of AlN coatings on graphite substrates, Thin Solid Films, Vol. 146, pp. 255-264, 1987.

33. Matthew T. Johnson, C. Barry Carter, AlN films grown by electric field induced flux of Al cations, Thin Solid Films, Vol. 339, pp. 117-119, 1999.

34. S. Six, J. W. Gerlachi, B. Rauschenbach, Epitaxial aluminum nitride films on sapphire formed by pulsed laser deposition, Thin Solid Films, Vol. 370, pp. 1-4, 2000.

35. Xiao-Hong Xu, Hai-Shun Wu, Cong-Jie Zhang, Zhi-Hao Jin, Morphological properties of AlN piezoelectric thin films deposited by DC reactive magnetron sputtering, Thin Solid Films, Vol.388, pp. 62-67, 2001.

36. M. Ishihara, S. J. Li, H. Yumoto, K. Akashi, Y. IDe, Control of preferential orientation of AlN films prepared by the reactive sputtering method, Thin Solid Films, Vol. 316, pp. 152-157, 1998.

37. H.P.Löbl, M. Klee, R. Milsom, R. Dekker, C. Metzmacher, W. Brand, P. Lok, Materials for bulk acoustic wave (BAW) resonators and filters, Journal of the European Ceramic Society, Vol. 21, pp. 2633-2640, 2001.

38. Marc-Alexandre Dubois, Paul Muralt, Victor Plessky, BAW resonators based on aluminum nitride thin films, IEEE Ultrasonics symposium, pp. 907-910, 1999.

39. Marc-Alexandre Dubois, Paul Muralt, Properties of aluminum nitride thin films for piezoelectric transducers and microwave filter applications, Vol. 74, pp. 3032-3034, 1999.

40. A. Dollet, Y. Casaux, G. Chaix, C. Dupuy, Chemical vapour deposition of polycrystalline AlN films from $AlCl_3$-NH_3 mixtures; Analysis and modeling of transport phenomena, Thin Solid Films, Vol. 406, pp. 1-16, 2002.

41. Ju-Won Soh, Seong-Soo Jang, In-Seop Jeong, Won-Jong Lee, C-axis orientation of AlN films prepared by ECR PECVD, Thin Solid Films, Vol. 279, pp. 17-22, 1996.

42. M. Penza, M. R. De riccardis, L. Mirenghi, M. A. Tagliente, E. Verona, Low temperature growth of r.f. reactively planar magnetron-sputtered AlN films, Thin Solid Films, Vol. 259, pp. 154-162, 1995.

43. Arshad Mahmood, Nikifor Rakov, Mufei Xiao, Influence of deposition conditions on optical properties of aluminum nitride (AlN) thin films prepared by DC-reactive magnetron sputtering, Materials Letters, Vol. 57, pp. 1925-1933, 2003.

44. B. Potì, M.A. Tagliente and A. Passaseo, High quality MOCVD GaN film grown on sapphire substrates using HT-AlN buffer layer, Journal of Non-Crystalline Solid, available online 5 June 2006.

45. Nobuhisa Tanuma, Munecazu Tacano, Jan Pavelka, Sumihisa Hashiguchi, Josef Sikula and Toshiaki Matsui, Hooge noise parameter of epitaxial n-GaN on sapphire, Solid-State Electronics, Vol. 49, pp. 865-870, 2005.

46. L.B. Jonsson, C. Hedlund, I.V. Katardjiev, and S. Berg, Compositional variations of sputter deposited Ti/W barrier layers on substraters with pronounced surface topography, Thin Solid Films, Vol. 348, pp. 227-232, 1999.

47. D. B. Bergstrom, F. Tian, I. Petrov, J. Moser, and J. E. Greene, Origin of compositional variations in sputter-deposited Ti_xW_{1-x} diffusion barrier layers, Applied Physics Letters, Vol. 67, pp. 3102-3104, 1995.

48. M. F. Doerner, and W. D. Nix, A method for interpreting the data from depth-sensing indentation instruments, Journal of Materials Research, Vol. 1 (4), pp 601-609, 1986.

49. W. C. Oliver, and G. M. Pharr, An improved technique for determining hardness and elastic modulus using load and displacement sensing indentation measurements, Journal of Materials Research, Vol. 7 (6), pp 1564-1583, 1992.

50. Kebin Geng, Fuqian Yang, Thad Druffel, Eric A. Grulke, Nanoindentation behavior of ultrathin polymeric films, Polymer, Vol.46, pp. 11768-11772, 2005.

51. Ichiro Yonenaga, Toshiyuki Shima, Marcel H. F. Sluiter, NaNo-indentation hardness and elastic moduli of bulk single crystal AlN, Japanese Journal of Applied Physics, Vol. 41, pp. 4620-4621, 2002.

52. H. Takahashi, J. Ohta, H. Fujioka, M. Oshima, M.Kimura, G-GIXD characterization of GaN grown by laser MBE, Journal of Crystal Growth, Vol. 237-239, pp. 1158-1162, 2002.

53. Q. M. Zhang, W. Y. Pan, and L. E. Cross, Laser interferometer for the study of piezoelectric and electrostrictive strains, Journal of Applied Physics, Vol. 63(8), pp. 2492, 1988.

54. Kazuo Tsubouchi, NoBuo Mikoshiba, Zero-Temperature-Coefficient SAW Devices on AlN Epitaxial Films, IEEE Transactions on Sonics and Ultrasonics, Vol. Su-32, pp. 634-644, 1995.

55. IEEE Standard on Piezoelectricity 176-1987, Available from IEEE Customer Service, Piscataway, NJ.

56. Shuyu Lin, Effect of electric load impedances on the performance of sandwich piezoelectric transducers, IEEE Transactions on Ultrasonics, Ferroelectrics and Frequency Control, Vol. 51, pp. 1280-1286, 2004.

57. A. H. Meitzler and E. K. Sittig, Characterization of piezoelectric transducers used in ultrasonic devices about 0.1GHz, Journal of Applied Physics, Vol. 40(11), pp. 4341-4352, 1969.

58. E. K. Sittig, Effects of bonding and electrode layers on the transmission parameters of piezoelectric transducers used in ultrasonic digital delay lines, IEEE Transactions on Sonics and Ultrasonics, Vol. 16, pp. 2-10, 1969.

59. E. K. Sittig, Transmission parameters of thickness-driven piezoelectric transducers arranged in multiplayer configurations, IEEE Transactions on Sonics and Ultrasonics, Vol. SU-1 (1967)167-174

60. E. K. Sittig, Design and technology of piezoelectric transducers for frequencies above 100MHz, Physical Acoustics, Vol. IX, Edts. W.P. Mason and R.N. Thurston, Academic Press, New York, pp. 221-275, 1972.

61. Y. Zhang, Resonant spectrum method to characterize piezoelectric film in composite resonators, IEEE Transactions on Ultrasonics, Ferroelectrics, and Frequency Control, Vol. 50, pp. 321-333, 2003.

62. M. Ylilammi, J. Ellä, M. Partanen, and J. Kaitila, Thin film bulk acoustic wave filter, IEEE Transactions on Ultrasonics, Ferroelectrics, and Frequency Control, Vol. 49, pp. 535-539, 2003.

63. K.M. Lakin, Improved Bulk Wave Resonator Coupling Coefficient For Wide Bandwidth Filters, IEEE Proceedings on Ultrasonics Symposium, pp. 827-831, 2001.

64. Qing-Xin Su, Paul Kirby, Thin-film bulk acoustic resonators and filters using ZnO and Lead-Zirconium-Titanate thin films, IEEE Transactions on Microwave Theory and Techniques, Vol. 49, pp. 769-778, 2001.

65. M. H. Francombe, S.V. Krishnaswamy, Growth and properties of piezoelectric and ferroelectric films, Journal of Vacuum Science and Technology A, Vol. 8, pp. 1382-1390, 1990.

66. S.V. Krishnaswamy, J. Rosenbaum, S. Horwitz, C. Vale and R. A. Moore, film Bulk Acoustic Wave resonator Technology, IEEE Ultrasonic Symposium, pp. 529-536, 1990.

67. Lakin, K.M.; McCarron, K.T.; McDonald, J.F. Temperature compensated bulk acoustic thin film resonators, Ultrasonics Symposium, 2000 IEEE, Vol. 1, pp. 855-858, 2000.

68. Kun-Wook Kim; Myeong-Gweon Gu; Jong-Gwan Yook; Han-Kyu Park, Resonator size effects on the TFBAR ladder filter performance, Microwave and Wireless Components Letters, IEEE, Vol. 13, pp. 335 – 337, 2003.

69. Weileun Fang, Determining thermal expansion coefficients of thin films using micromachined cantilevers, Sensors and Actuators A, Vol. 77, pp. 21-27, 1999.

70. J. D. Zook, D. W. Burns, Characteristics of polysilicon resonant microbeams, Sensors and Actuators A, Vol. 35, pp. 51-59, 1992.

71. Han Jianqiang, Zhu Changchun, Dependence of the resonance frequency of thermally excited microcantilever resonators on temperature, Sensors and Actuators A, Vol. 101, pp. 37-41, 2002.

72. On-Wafer Vector Network Analyzer Calibration and Measurements, Application note, Cascade Microtech. USA

73. A. F. Wright, Elastic properties of zinc-blende and wurtzite AlN, GaN, and InN, Journal of Applied Physics, Vol. 82, pp. 2833-2839, 1997.

74. A. Kampfe, B. Eigenmann, O. Vohringer, and D. Lohe, X-ray and single crystal values of the elastic constants and determination of machining residual stresses in AlN, High Temperature Material Processes, Vol. 2, pp. 309-326, 1998.